UNIVERSITY OF OKLAHOMA

GRADUATE COLLEGE

IMPORTANCE OF CAPILLARY HETEROGENEITY IN DEVELOPING A REPRESENTATIVE RESERVOIR MODEL FOR SHALES WITH COMPLEX FRACTURES

A THESIS

SUBMITTED TO THE GRADUATE FACULTY

in partial fulfillment of the requirements for the

Degree of

MASTER OF SCIENCE

By

YIWEN GONG
Norman, Oklahoma
2016

IMPORTANCE OF CAPILLARY HETEROGENEITY IN DEVELOPING A REPRESENTATIVE RESERVOIR MODEL FOR SHALES WITH COMPLEX FRACTURES

A THESIS APPROVED FOR THE
MEWBOURNE SCHOOL OF PETROLEUM AND GEOLOGICAL ENGINEERING

BY

_____
Dr. Ahmad Sakhaee-Pour, Chair

_____
Dr. Xingru Wu

_____
Dr. Deepak Devegowda

I dedicate this master thesis work to my parents, Mr. Jiansheng Gong and Ms. Xia Liu, for both financial and spiritual support. I would also to thank my uncle Mr. Jianxin Gong and my cousin Miss. Yixuan Gong for their support on my hardest time spiritually.

Acknowledgements

I would like to thank my advisor, Dr. Ahmad Sakhaee-Pour for his support on weekly meeting to guide my research. I would also like to thank Dr. Xingru Wu and Dr. Deepak Devegowda for the help of thesis revisions.

Table of Contents

List of Tables

List of Figures

Abstract

Our advancement in hydraulic fracturing has enabled us to produce shale formations economically. The formation stimulation is successful when the effective transport properties of the formation is improved significantly, which is achieved usually by creating multiple intersecting curved (complex) fractures in tight formations. The transport mechanisms are fundamentally different from those of high-permeable (conventional) formations since the fracture-matrix contact surface, which is often curved, is much larger. The difference between the transport properties of the matrix and the fractures is also more significant, in shales, which adds another complexity to this problem.

Our main objective in this research is to determine the importance of a formation heterogeneity on the estimated ultimate recovery (EUR) of a shale formation. We determine the accuracy of the reduced model. We also analyze hydrocarbon production from shales with complex fractures based on the fracture cell model (Sakhaee-Pour and Wheeler, 2016). The fracture cell model accounts for the effects of multiple intersecting curved (complex) fractures on the transport properties. It takes different representations for the relative permeability and the capillary pressure of the matrix and the fracture. Further, we use a geostatistically representative model to account for the formation heterogeneity as it relates to the porosity, permeability, and capillary pressure.

Our study shows that the capillarity heterogeneity plays a dominant role in estimated ultimate recovery (EUR) of shales, whereas the effects of permeability and porosity

heterogeneity is less important. The local trapping caused by the capillary heterogeneity in all cases helped the pressure drop of the reservoir in early time and mitigate the cumulative oil production in later time.

Chapter 1: Introduction

1.1 Problem Statement

The heterogeneous character of the shale formation (Barnett Shale) leads to the less promising well performance from the traditional standard completion techniques (Daniels, et al. 2007). The reduction on hydrocarbon phase trapping that is caused by the capillary pressure and the wetting histories in the tight reservoir essentially enhances the relative permeability of hydrocarbons (Penny, Pursley and Clawson 2006). The pore radius becomes significantly important on capillarity-induced phase behavior change when it is on nanometers (Nojabaei, Johns and Chu 2013).

The capillarity effect of multi-component tight oil reservoir currently has not been well understood due to the lack of representative phase behavior models in the ultra-low permeability scenario (Zhang, et al. 2016). The presence of the capillary pressure in some wettability situations could be the driven force. When it comes with the tight reservoir with heterogeneous petrophysical properties, all other issues, such as the pore throat and adsorption/desorption, leads to the extra challenges of estimating the expected ultimate recovery (EUR) of the tight formation.

1.2 Objective

The primary objective of this work is to investigate the effect of formation heterogeneity on the EUR of the shale formation. The heterogeneities considered here are relevant to the permeability, porosity and the capillary pressure. We use geostatistical data for each petrophysical property and conduct two-phase flow for different realizations. Averaging

the results obtained for different realizations allow us to discuss the cumulative production of the formation.

The secondary objective of this research is to determine the predictive capabilities of the reduced model with different formation heterogeneities. We compare the normalized cumulative production results of the reduced model with those of the refined model (reference model). The comparison enables us to further test the accuracy of the fracture cell as it relates to the two-phase flow (Sakhaee-Pour and Wheeler, 2016).

1.3 Research Hypothesis

In order to precisely describe the curved fractures intersecting with each other, local refinement and introducing irregular grid shape is not a computationally economical. Instead, the fracture cell model, developed recently by Sakhaee-Pour and Wheeler 2016) is used.

The hypothesis of this research is that we can capture the formation heterogeneity relevant to permeability, porosity, and capillary pressure if we account for the effective transport properties of fracture using the fracture cell model. We will build a reservoir cell model with an arbitrary fracture whose transport properties are determined from petrophysical measurements of shale. We test the hypothesis by comparing the results based on the fracture cell model with the refined model.

1.4 Thesis Outline

Regular shaped cells are used to capture the effects of fractures with an arbitrary geometry in this research on the transport properties. The effective permeability and porosity are assigned to each cell with a fracture to mimic fracture-fracture, fracture-matrix and matrix-matrix interactions in three principal directions. This approach can be widely applied to a complex fracture pattern, such as those observed in heavily stimulated formations, naturally fractured carbonates, and those stimulated by acidizing.

The present thesis consists of the following chapters:

Chapter 2: literature review as it relates to the petrophysical properties of shale formations such as absolute permeability, relative permeability, and capillary pressure. It also discusses the recent developments on modeling heavily stimulated tight formations.

Chapter 3: the fracture cell model is discussed. We elaborate the implementation of the effective transport properties based on the fracture cell model in commercial software.

Chapter 4: heterogeneity of the shale formation. We develop a geostatistically representative model for shale formations. The representative model embraces realistic models for porosity, permeability, and capillary pressure. The capillary pressure is scaled using *J* function.

Chapter 5: Results of the conducted study. We discuss the importance of capillary pressure heterogeneity.

Chapter 6: Conclusion. We summarize the conclusions relevant to building a representative model for shale formations by accounting for the formation heterogeneity based on the fracture cell model. The addressed conclusions have major implications for developing a realistic model for shales with complex fractures.

Chapter 2: Literature Review

2.1 Complexities of Transport Properties in Tight Formations

The nanoscale or microscale pore network distribution dominant the gas flow in shale play (Javadpour, Fisher and Unsworth 2007). The transfer phenomena between the fracture and matrix during the production from fractured reservoir are effect by the combined processes of fluid expansion, capillary imbibition, gravity drainage and diffusion (Lu, Donato and Blunt 2008). The porosity and cross-sectional area for gas transporting mitigate due to the pore pressure, indicating the difficulty of the transport in shale formation (Xiong, et al. 2012). The storage mechanisms can be as complicated as in four ways: natural fractures, matrix pores, adsorbed in kerogen bulk and dissolved in kerogen bulk (Swami, Settary and Javadpour 2013). Knowing the disorder fact of gain alignment in small scale, the anisotropy in transport and elasticity characteristics are caused by the organized larger scale grain alignment (Sondergeld, et al. 2010).

Proper fracture path configuration for contact area determination and reservoir simulator flow properties input are the factors influencing production estimation dramatically. (Dewers, et al. 2012) used focused ion beam-scanning electron microscopy (FIB-SEM) to visualize the pore networks of mudstone, such as pore properties, topology and tortuosity. Counting both effective Knudsen diffusivity and intrinsic permeability in the apparent permeability of organic matter calculation gives better transport behaviors (Chen, et al. 2015). Civan (2010) pointed out that including relevant gas retention and transport in shale gives better apparent shale gas permeability and diffusivity description. The constant diffusion coefficient obtained from modeling of the gas flow in nanopores

with a diffusive transport regime helped to count slip boundary conditions on the surface of the nanopores (Javadpour, Fisher and Unsworth 2007). The more complicated permeability distribution actually happens when the formation is highly heterogeneous. Due to tectonic and other complex stress issues, the hypothesis of forming simple two-wings fracture pattern are not likely to happen. Instead, it is highly possible to appear as complex fracture network showing in **Figure 1**. In heterogeneous reservoir, the permeability is appeared in log-normal for permeability and the local capillary trapping could occur (Saadatpoor, Bryant and Sephernoori 2010). This characteristic leads to the extra difficulties for fluid flow in porous media.

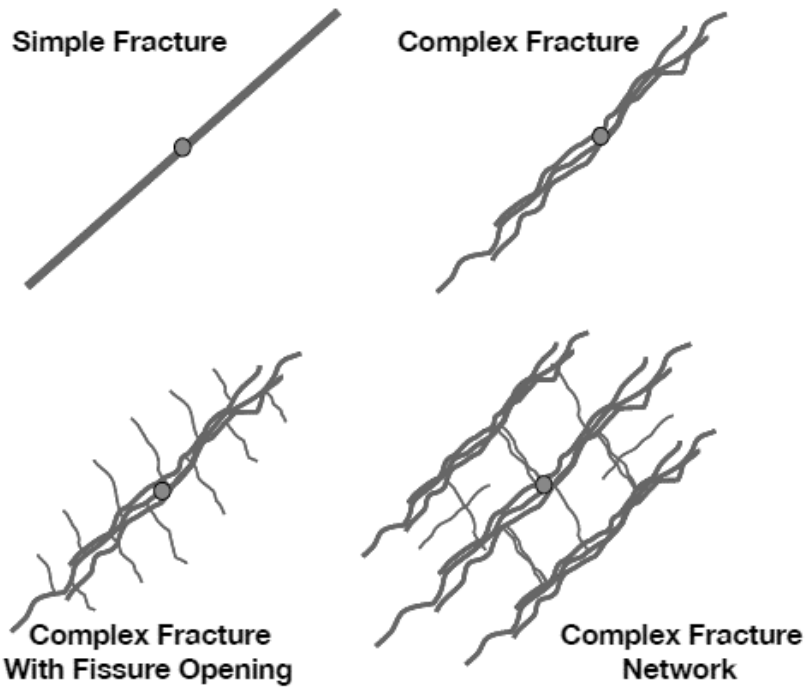

Figure 1. Fracture pattern complexity example. (Fisher et al., 2002)

2.2 Fluid Flow Behaviors in Tight Reservoirs

2.2.1 Fluid Flow Behaviors

The transport property especially the gas permeability is essentially influenced by the absorption and slippage phenomenon on the pore walls in nanoscale permeability reservoirs (Sakhaee-Pour and Bryant, 2012). The high Knudsen number flow in nanopores is usually used to predict transport characteristics (Roya, et al. 2003). The sorbed phase should be adjusted in the gas in place estimation in shale (Ambrose, et al. 2012, Hartman, et al. 2011). Desorption-adsorption models (Shabro, et al. 2014, Ambrose, et al. 2012), Knudsen's number, Knudsen and slip flow models (Freeman, et al. 2012, Darabi, et al. 2012) provide better understanding of tight reservoir simulation while few of these works imposed the effect to pressure/volume/temperature (PVT) properties and to flow behaviors from the pore size distribution (Pitakbunkate, et al. 2016). Wu et al. (2016) developed a new approach to investigate the adsorption effect with the existence of capillarity in tight formations. The larger drawdown from the reservoir to the bottom hole leads larger production rate. In shale reservoir, the liquid dropout forms due to the pressure excessive drop below the bubble point near the wellbore. Such reservoirs are called liquid rich shale (LRS). The production data and numerical modeling of LRS should be incorporated to establish accurate phase behavior models (Ganjdanesh, et al. 2016).

Figure 2 is obtained from the computational fluid dynamics (CFD) simulation through the ultralow permeability rock with varies pore throat sizes. The actual volume mesh and is showing in the **Figure 2 (a)** whereas the streamlines through the volume is showing in

the **Figure 2 (b)**. The color differences show the different velocities. The varies flow velocities and distribution give the indirect flow complexity indication in the tight rocks or shales.

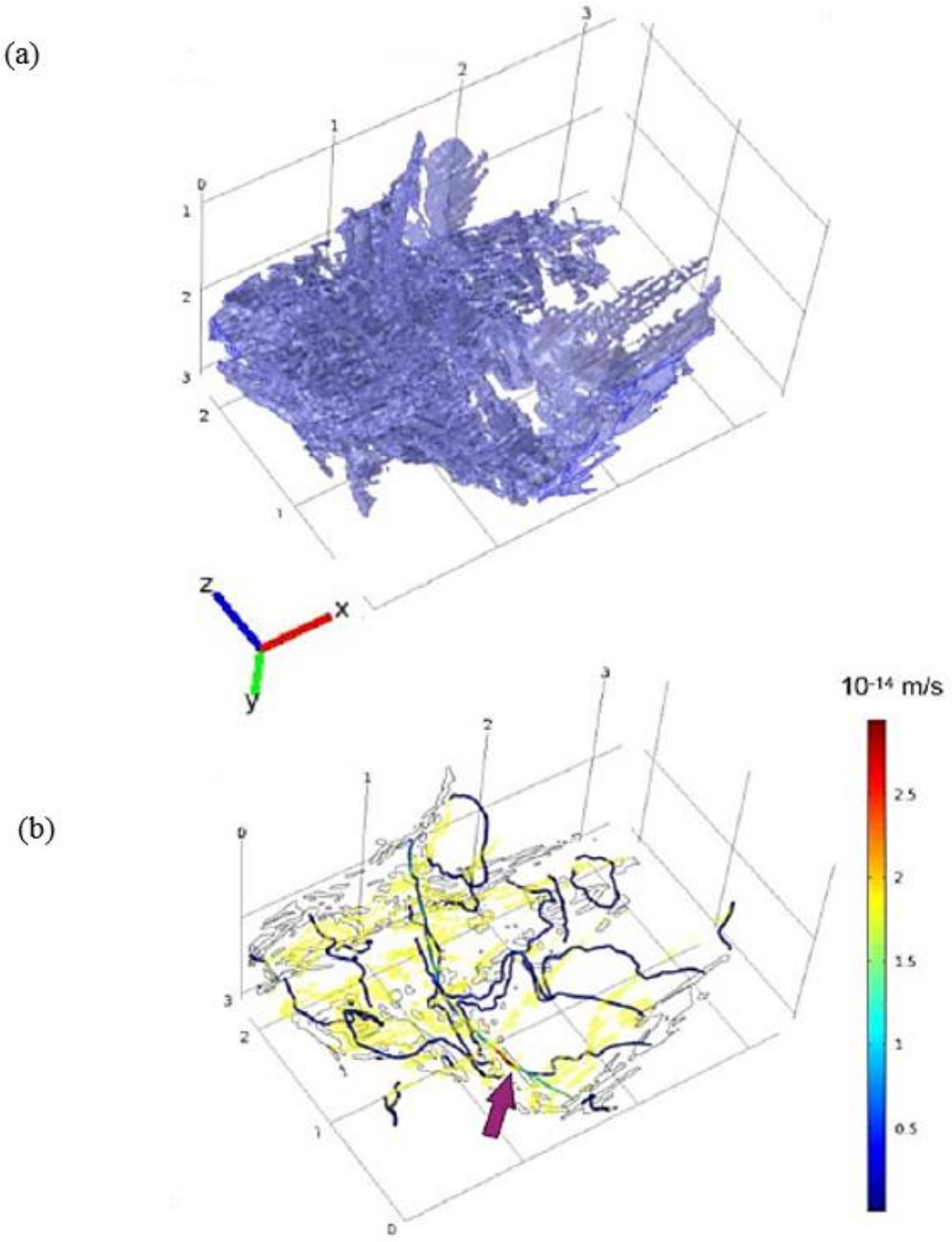

Figure 2. Fluid flow through the complex connected network (Dewers, et al. 2012).

2.2.2 Permeability and Permeability Measurement

The (Corey 1954) Model gives a simple and a representative description for the relationship between the relative permeabilities and the saturations. Shad et al. (2010) extended Corey (1954) Model's theory, they concluded that in the natural fracture reservoirs, the relative permeabilities are the function of both saturations and the fracture orientations.

The difficulties of shale permeability measurement are not only caused by the technical limitations but also the versatile shale characteristics. Obtaining the petrophysical properties from core analysis is time consuming and economical unfriendly. The dominant pore throat sizes become more essential compared to the physical geometry of the pore-size distribution while measuring the permeability in ultra-tight formation (Shabro, et al. 2014, Sakhaee-Pour and Bryant, 2014). The difference between the apparent permeability measured directly from the Darcy's law and the intrinsic permeability with Knudsen number considered could be significantly high with respect to the core plug local conditions (Civan, Rai and Sondergeld, 2011). The proper corrections for the permeability measurement results from transient techniques provide consistent results to that from the steady state techniques within 30% tolerance (Mathur, Sondergeld and Rai 2016).

The steady state method and the transient method are two major approaches of core plug based shale matrix permeability measurement. Saneifar et al. (2014) built the method which corporates well logs to the core measurement to assess the petrophysical and

compositional properties of the shale-gas reservoir, providing reliable rock classification method. Civan, Devegowda and Sigal (2013) made corrections regarding the permeability measurement so that the Knudsen diffusion and pore-proximity are included based on the combined method regarding the transient-state formulations. Tian et al. (2015) couples interporosity flow model with production data to determine the effective permeability.

The transport properties measurements, such as permeability and porosity, are also largely affected by the net stress, pore pressure and the temperature (Zamirian, Aminian and Fathi 2014, Sinha, et al. 2013). The change in the confining pressure has more significant effect compared to the change of pore pressure (Heller, Vermylen and Zoback 2014). In most shale, the confining-pressure-dependent permeability is caused by cracks, with the observations of three magnitude variabilities of permeability under different confining pressures (Tinni, et al. 2012). Latham et al. (2012) modeled the stress-dependent permeability caused by stress heterogeneity, and new / pre-existing fractures behaviors under the far-field stresses. Gaining the knowledge of pre-existing fault activation possibility for shale formations due to varies clay content aids in stimulation operations (Zoback, et al. 2012).

2.2.3 Capillary Pressure and J function

The capillary pressure is defined as the pressure difference between the non-wetting phase and the wetting phase at the its fluids interface.

$$p_c = p_{nw} - p_w \qquad (1)$$

Van Genuchten (1980) capillary pressure model is widely used describing the relationship between the saturation and capillary pressure.

$$p_c = \frac{1}{\alpha}\left(\overline{S}^{-\frac{1}{m}} - 1\right)^{1-m} \qquad (2)$$

The empirical parameters, α and m, are obtained for different soil types from laboratory measurements. However, the capillary pressure for multiphase flow in the heterogeneous, tight, heavily fractured reservoirs behaves more complicated. Leverett (1941) took the capillary pressure variance with different permeabilities and porosities into count for the same reservoir by *J*- Leverett function scaling. This *J* function is a function of wetting phase saturation.

2.3 Simple / Planar Fracture Models

The two-dimensional fracture geometry models under bunch of assumptions are usually being used for describing the hydraulic fractures for sake of simplicity. PKN (Perkins and Kern 1961, Nordgren 1972) and KGD (Geertsma and Klerk 1969) are famous two dimensional planar fracture models. Their geometries are showing in **Figure 3**. Both models assume planar fracture geometries with two wings that are formed in a horizontally isotropic in-situ stress field condition. In other words, these models assume that rock anisotropy and discontinuity do not influence the fracture path; the fracture propagation direction is perpendicular to the minimum horizontal principal stress direction.

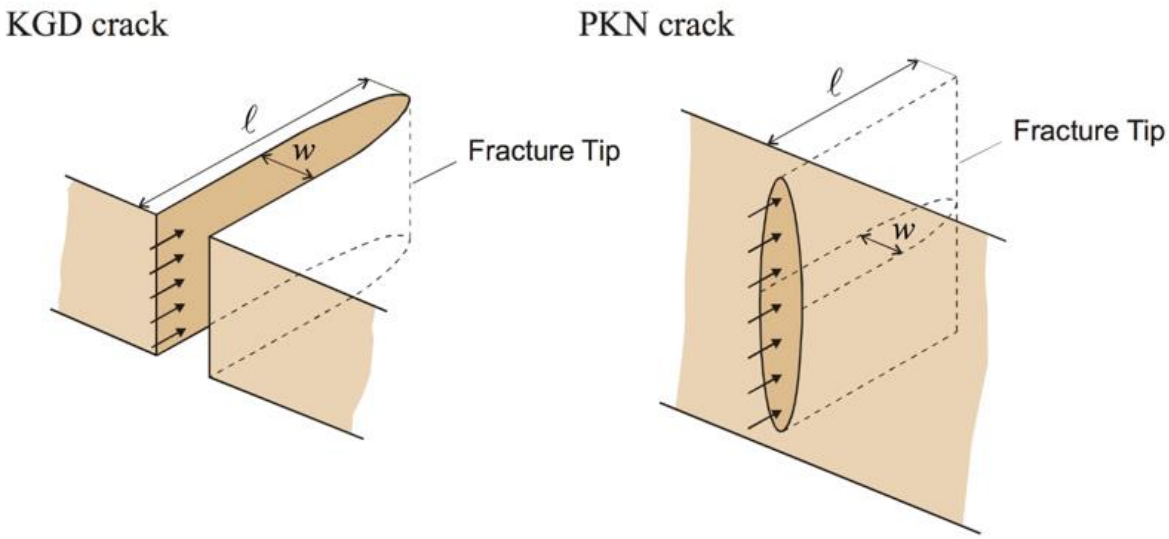

Figure 3. Schematic diagram of KGD and PKN fracture model. (University of Minnesota College of Science & Engineering 2012)

2.4 Improved Models / Simulators

2.4.1 Importance of Capturing Complex Fractures in Tight Formations

For heavily fractured reservoir, the fracture paths are not simply planar fractures. Instead, the multiple curved intersected fractures are the more realistic fracture geometries. The complex fracture networks can be formed by the complex geological events. The ununiformed stress-state and other mechanisms, such as complex deposition, tectonic movement, diagenesis and pre-existing natural fractures, possibly caused the dendritic fracture networks (Rylance 2013). The better capturing of the fracture paths leads to the precise hydrocarbon production estimation and forecasting. Thus, the advanced techniques to describing the fracture networks are essentially needed (Sakhaee-Pour and Wheeler 2016).

The fluid flow behaviors have developed as early as in the middle of last centuries. Barenblatt, Zheltov and Kochina (1960) studied the unsteady state fluid flow in porous media and introduced two types of fluid pressure regarding their locations. Warren and Root (1963) built a heterogeneous porous media model which is widely being accepted as the basis of heterogeneous reservoir simulation showing in **Figure 4**. Swaan (1976) developed a mathematical model which detects the pressure responses in natural fractures from the slightly compressible fluid flow. Kazemi et al. (1976) dramatically extended the simulation formulation from Warren and Root (1963)'s model. They took the three dimensions, multiphase, gravity effect and complex reservoir properties into consideration. Blaskovish et al. (1983) introduced a new model; it addressed the spatial framework, hydrocarbon fluid complexity and dual porosity/permeability in the reservoir simulator. Dean and Lo (1988) compared the hydrocarbon production from the single-porosity, dual-permeability and from dual-porosity simulation models in the natural fractured reservoirs.

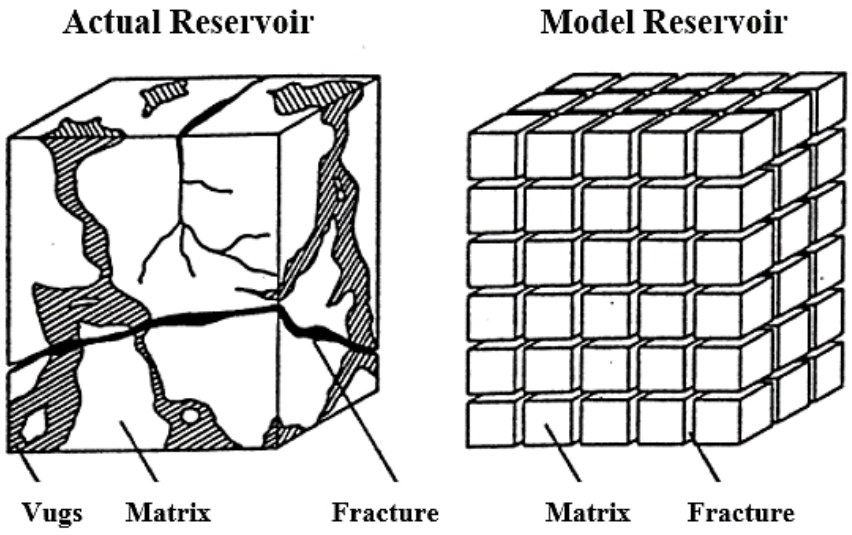

Figure 4. Idealized Sugar Cube model (Warren and Root 1963).

2.4.2 Improved Models / Simulators

In the recent few years, researchers made efforts on building the representative model to characterize the shale reservoirs and the fluid flow in the tight / ultra-tight reservoirs. Balogun et al. (2007) verified the transfer function for dual porosity and dual permeability reservoirs in field scale. Hoteit and Firoozabadi (2008) used different approaches, including finite difference, finite volume and finite elements, to couple with discrete-fracture models for multiphase flow in porous media. This method introduces triangular shaped grids with all different meshed angles showing in **Figure 5**. Warpinski et al. (2009) pointed out that high production from the ultra-tight reservoir are ensured by appropriate fracture spacing and by enough delivery of hydrocarbon from the matrix to the fractures. Yin et al. (2011) conducted well drainage volume computation method for multistage fracturing shale reservoir. They also matched they stimulated reservoir volume with the drainage volume matching by the traditional history matching approach. Moinfar et al. (2013) generated a coupled model to describe the hydraulic fractures with EDFM approach and the natural fractures with dual continuum approach in an integrated system. They also extended the algorithm from Li and Lee (2008) by developing the embedded discrete fracture (EDFM) with fully implicit compositional reservoir simulator for the arbitrary orientated fractures. Al-Hinai et al. (2013) modeled multiphase fluid flow with complex fracture geometries by coupling mimetic finite difference method with the multipoint flux mixed finite element method. Yan et al. (2013) conducted a triple porosity system, including organic matter, inorganic matter and natural fractures, to simulate the fluid flow in shale reservoir in microscale. Olorode et al. (2013) studied the production

from coupled primary/secondary fractures with different inclined planar fractures along the completion zones showing in **Figure 6**.

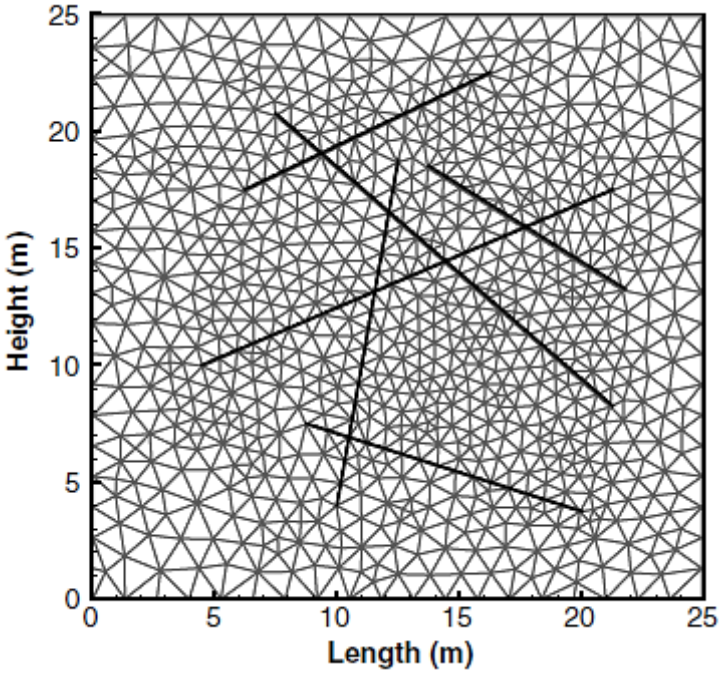

Figure 5. Diagram of triangular meshed fracture (Hoteit and Firoozabadi 2008).

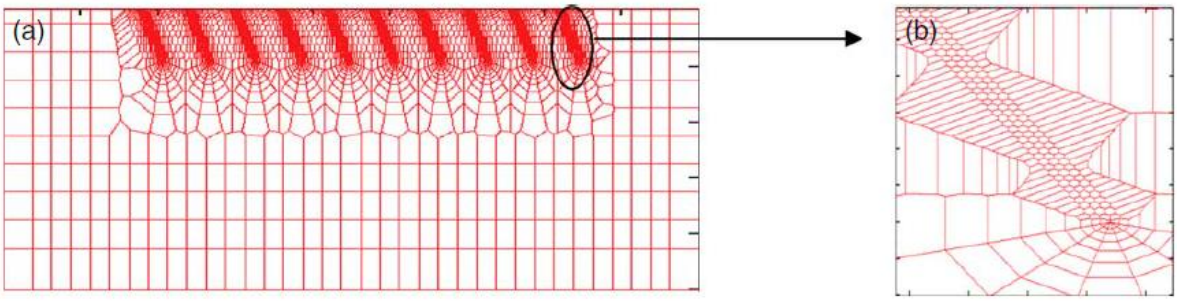

Figure 6. Diagram of unstructured grid meshed fracture (Olorode, et al. 2013).

In recent two years, Sakhaee-Pour and Wheeler (2016) developed Fracture-Cell model without performing local refinement to capture the nonplanarity of the fractures. This model considers the interactions of matrix-matrix, matrix-fracture and fracture-fracture in tight reservoirs. Xie et al. (2015) cooperated the fast marching method (FMM) to the geometric pressure approximation to estimate the drainage volume and well performance of shale reservoir with complex fracture networks, increasing the efficiency of reservoir properties estimation. Alfi et al. (2015) described the porous media in three sub-regions (inorganic matter, kerogen and fracture network) to configure the heterogeneity of the shale reservoir in micrometer scale. Filho et al. (2015) applied the Embedded Discrete Fracture Model (EDFM) to the IMPEC compositional reservoir simulator (UTCOMP) and coded the preprocessing code to adjust the discrete fracture patterns in the simulator.

Zheng et al. (2016) investigated the geomechanical effect, especially TPHM-based permeability as a function of effective stress on the production rate. This relationship is implemented in the simplified numerical model to estimate the production rate in tight reservoir. Shakiba et all. (2013) built the Distinct Element method, which studies the interactions between the hydraulic fractures and surrounding natural fractures. They found that the cumulative oil production increases if the hydraulic fracture extends and connects more natural fractures.

Chapter 3: Fracture-Cell Model

3.1 Fracture – Cell Model

Sakhaee-Pour and Wheeler (2016) developed the Fracture-Cell model to modify the effective multiphase transport properties for a cell containing fractures without local refinement. The main idea is to implement effective transport properties to account for the presence of fractures in an existing code without developing a new code. In other words, the Fracture-Cell model can be used with the minimum changes, which is desired, in the existing reservoir simulators when we are interested in their influence on hydrocarbon productions. Other recently developed codes usually couple different codes or mesh refinements around the fractures to capture its complex topology.

The Fracture-Cell model determines the effective multiphase transport properties of a reservoir cell with a fracture to account for its interactions with a neighboring cell. The fracture cell can interact with a neighboring cell via matrix (*M-F* in **Figure 7**) or fracture (*F-F* in **Figure 7**). The determined effective transport properties include porosity, absolute permeability, relative permeability, and capillary pressure. The geometry and number of fractures are arbitrary.

The Fracture-Cell model by its name generally counts the interactions between the matrix and fractures. In the model, we specify matrix cell as non-fracture passed cells while the fracture cell as fracture passed cells. As a results, the three types of interactions are showing in the **Figure 7**. There are generally three types of interactions in this models with respect to fracture and matrix: 1. Matrix-matrix interaction; 2. Fracture-matrix

interaction; 3. Fracture-fracture interactions. The most importance of the Fracture-Cell model is that the uniform size of the cells is used in the reservoir simulation model without local refinement. It provides a more efficient and economical utilization in the simulation works. The analytical calculated flow properties are implemented to compensate the uniform cell size utilization.

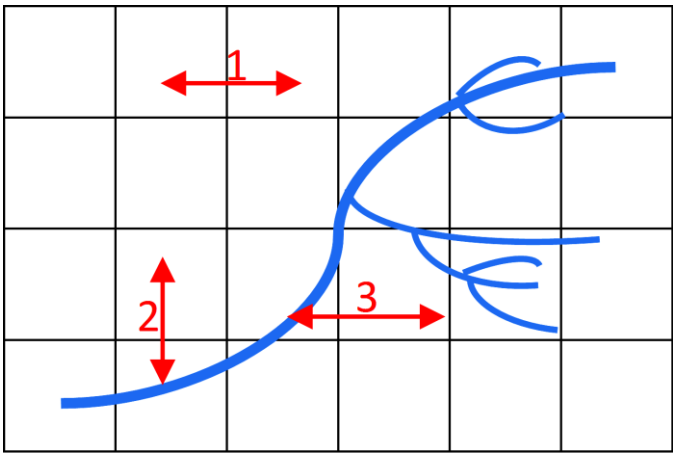

Figure 7. Schematic of interactions between reservoir cells and neighboring cells. There are three types of interactions between the reservoir cell: matrix-matrix (1), matrix-fracture (2), and fracture-fracture (3). The fracture cell model (Sakhaee-Pour and Wheeler 2016) determines the effective transport properties for *M-F* and *F-F*, whereas standard core measurements characterizes *M-M*.

Figure 8 (a) shows an arbitrary fracture path in the grid meshes or cells. The fracture cells are defined as the cells that have at least one fracture passing by in the grid meshes. They are denoted (1) to (9) in the **Figure 8 (b)**. The matrix cells are the grids that have no fracture passing by. All the grid meshes in here are having the uniformed size in square shape. The interactions between the fracture cells and matrix cells are counted by three types of effective permeabilities in the Fracture-Cell model.

The term k_{FF} is the effective permeability of the fracture cells interactions. It is calculated by

$$k_{FF} = (\frac{l_C}{l_f}) \frac{w^3}{12h} \quad (3)$$

Where the （l_C/l_f） is length ratio of representative path length showing in **Figure 8 (b)** and actual fracture length showing in **Figure 8 (a)**, *w* is the width of the fracture, and *h* is the cell size.

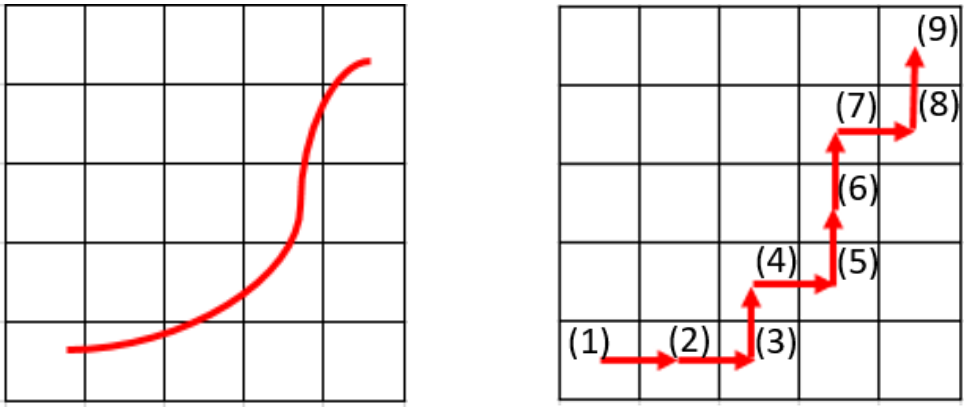

(a) **(b)**

Figure 8. lf is the patch of the fracture length in two visualizations

The matrix-fracture effective permeability k_{MF} is obtained by considering the speial contributions of different regions in a fracture cell for both fracture surrounding region and other matrix regions on a specific direction. We use a rectangular shape to cover the fracture passed area and define several regions as showing in **Figure 9** regarding fracture passed region (S) and other areas denoted in numbers (2) to (4). For example, in the **Figure 9**, part (S) and part (3) are parallel flow in the *x* direction; and the combined middle region along with part (2) and part (4) are series flow on the *x* direction. That is

how we obtained the expression for the k_{MF-x} on the *x* direction in this fracture cell. The k_{MF-y} is obtained by using the same approach. Their expressions are shown below:

$$k_{MF-x} = \frac{1}{\frac{1-\frac{b}{h}}{k_m} + \frac{\frac{b}{h}}{\frac{a}{h}k_{S-x} + (1-\frac{a}{h})k_m}} \quad (4)$$

$$k_{MF-y} = \frac{1}{\frac{1-\frac{a}{h}}{k_m} + \frac{\frac{a}{h}}{\frac{b}{h}k_{S-y} + (1-\frac{b}{h})k_m}} \quad (5)$$

Where (*a*/*h*) is the span ratio and (*b*/*h*) is the penetration ratio. k_{S-x} and k_{S-y} are the equivalent permeability of fracture surrounding region. Term *a*, *b* and *h* are visualized in the **Figure 9**. The red segment is the fracture path within this fracture cell. Term *a* is length along the *y* axis for fracture passed region while *b* is that of the *x* axis.

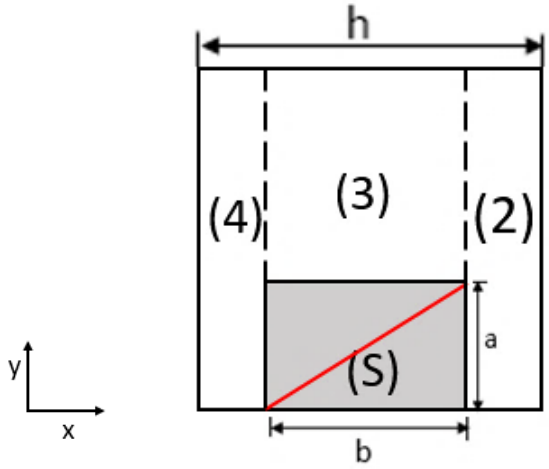

Figure 9. Visualization of the fracture-passed cell dimensions.

Since the permeability of surrounding region k_{S-x} and k_{S-y} have much higher order of magnitude than the matrix permeability due to the existence of the fracture in (*S*) region, the k_{MF} equations showing above can be simplified to

$$k_{MF-x} = \frac{k_m}{1-\frac{b}{h}} \quad (6)$$

$$k_{MF-y} = \frac{k_m}{1-\frac{a}{h}} \quad (7)$$

For the effective permeability k_{MM} that counts matrix-matrix interactions, it is simply equals to the matrix permeability k_m that is measured from the laboratory. We simply substitute the k_{MM} with k_m in the equation (4) to equation (7).

If a fracture cell has more than one fracture segments passing through, it is advisable to use a rectangular shape dyed with blue in **Figure 10** to group the whole fractures passed area within this single fracture cell. The length of *a* will be the *y* axis length of blue rectangular and *b* will be the *x* direction length of the blue rectangular. **Figure 10** gives a better explanation of the measurement.

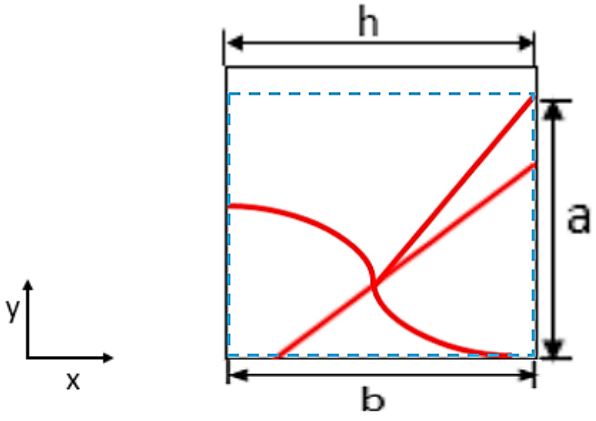

Figure 10. Measurement of parameters with multiple fracture paths.

3.2 Representative Reservoir model

3.2.1 Implementation Attempt

Figure 10 (a) below shows a single curved fracture dyed with blue. The colored gridblocks showing in **Figure 10 (b)** are the fracture passed gridblocks and they are numbered in order to aid to the k_{MF} calculation.

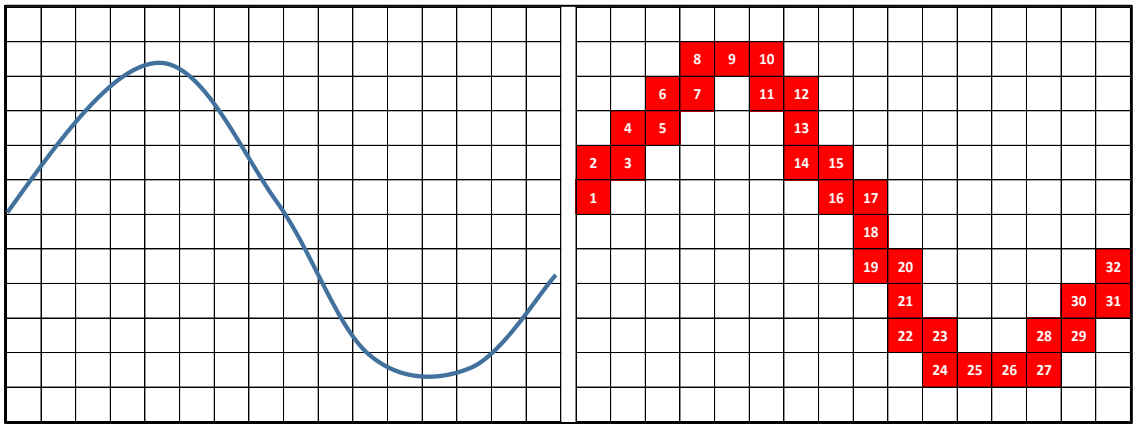

(a) **(b)**

Figure 11. Fracture path visualization of one part of 40 by 40 grids range.

(a) Single fracture is shown with blue curve.

(b) Fracture passed grid blocks. They are numbered in order.

Recalling the methodology to measure *a*, *b* and *h* for a single fracture cell, the measurements are done for every single fracture-passed cells showing **Figure 10 (b)**. As for the *h*, it is subjective to change.

Term *l* / *h* in each fracture cell is calculated by

$$\frac{l}{h} = \sqrt{\left(\frac{a}{h}\right)^2 + \left(\frac{b}{h}\right)^2} \qquad (8)$$

When we add up all the (l/h) terms for fracture cells, the length of the l_f is obtained by multiplying the summation of (l/h) by h.

A fracture cell, based on the Fracture-Cell model, has one or more fracture cell(s) as its neighbor(s) and/or one or more matrix cells at other side(s) of its adjacent sides as it is showed in the **Figure 11**. Therefore, there are two types of effective permeabilities for the fracture cell: k_{FF} and $k_{MF.}$ However, we are unable to input two values of permeabilities at a single fracture cell's location. So, we have to transfer one of these two effect permeability value onto its neighbor's to count both effective permeability for this fracture cell. We chose to transfer k_{MF} to its neighbor, a matrix cell in here. Since the effect of smearing the matrix cell's permeability is negligible.

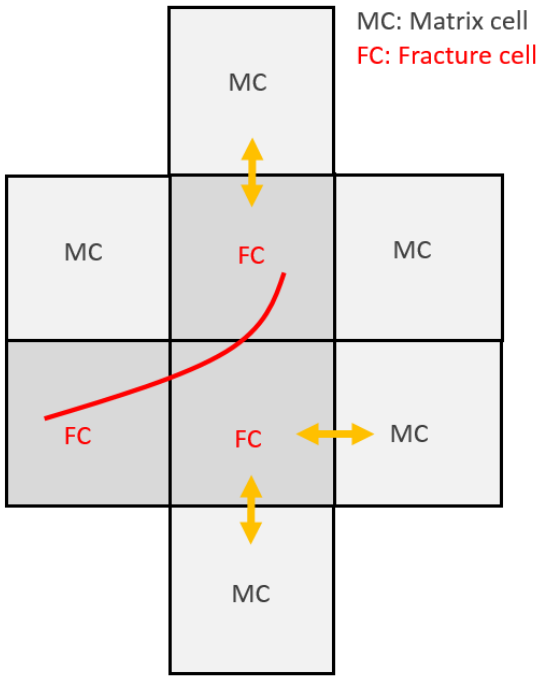

Figure 12. Fracture cell interactions between its adjacent cells.

This transferring process is considered with the transmissibility at the boundary of the fracture cell and the matrix cell. The physical reality of fracture cell and its adjacent matrix cell has k_{MF-x} and k_m input in their transmissibility's terms:

$$\frac{1}{T_{x\pm\frac{1}{2}}} = \frac{1}{2}\left(\frac{1}{T_i} + \frac{1}{T_{i\pm1}}\right) = \frac{1}{2}\left[\frac{1}{\left(\beta_c\frac{A_x k_x}{\mu_l B_l \Delta x}\right)_i} + \frac{1}{\left(\beta_c\frac{A_x k_x}{\mu_l B_l \Delta x}\right)_{i\pm1}}\right] = \frac{\mu_l B_l \Delta x}{2\beta_c A_x}\left(\frac{1}{k_i} + \frac{1}{k_{i\pm1}}\right) =$$

$$\frac{\mu_l B_l \Delta x}{2\beta_c A_x}\left(\frac{1}{k_{MF-x}} + \frac{1}{k_m}\right) \qquad (9)$$

For reservoir simulator input is having k_{FF} as permeability input in fracture cell transmissibility expression and a modified k'_{MF-x} permeability that will be assigned to the matrix cell to count the fracture-matrix interaction:

$$\frac{1}{T_{x\pm\frac{1}{2}}} = \frac{1}{2}\left(\frac{1}{T_i} + \frac{1}{T_{i\pm1}}\right) = \frac{1}{2}\left[\frac{1}{\left(\beta_c\frac{A_x k_x}{\mu_l B_l \Delta x}\right)_i} + \frac{1}{\left(\beta_c\frac{A_x k_x}{\mu_l B_l \Delta x}\right)_{i\pm1}}\right] = \frac{\mu_l B_l \Delta x}{2\beta_c A_x}\left(\frac{1}{k_i} + \frac{1}{k_{i\pm1}}\right) =$$

$$\frac{\mu_l B_l \Delta x}{2\beta_c A_x}\left(\frac{1}{k_{FF-x}} + \frac{1}{k'_{MF-x}}\right) \qquad (10)$$

To let the physical reality case equals reservoir simulator input case, equation yields:

$$\frac{\mu_l B_l \Delta x}{2\beta_c A_x}\left(\frac{1}{k_{MF-x}} + \frac{1}{k_m}\right) = \frac{\mu_l B_l \Delta x}{2\beta_c A_x}\left(\frac{1}{k_{FF}} + \frac{1}{k'_{MF-x}}\right) \qquad (11)$$

By canceling out the common terms in the transmissibility forms:

$$\frac{1}{k_{MF-x}} + \frac{1}{k_m} = \frac{1}{k_{FF}} + \frac{1}{k'_{MF-x}} \qquad (12)$$

Then, we rearrange the equation:

$$\frac{1}{k'_{MF-x}} = \frac{1}{k_{MF-x}} + \frac{1}{k_m} - \frac{1}{k_{FF}} \quad (13)$$

Since the fracture permeability k_{FF} is larger than matrix related permeability k_{MF-x} and $k_m$with several orders of magnitudes ($k_{MF-x}$and k_m are in the same magnitude), $\frac{1}{k_{FF}}$ term can be neglected in here.

The above equation is simplified to

$$\frac{1}{k'_{MF-x}} = \frac{1}{k_{MF-x}} + \frac{1}{k_m} \quad (14)$$

The modified matrix fracture permeability on the *x* direction is calculated by

$$k'_{MF-x} = \frac{k_{MF-x} + k_m}{k_{MF-x}\, k_m} \quad (15)$$

In the *y* direction, it is equal to:

$$k'_{MF-y} = \frac{k_{MF-y} + k_m}{k_{MF-y}\, k_m} \quad (16)$$

k_{MF-x} and k_{MF-y} are calculated by equation (6) and equation (7). Term k_m is 1 μd, 100 nd and 10 nd as three scenarios for investigating the ultra-tight formation. In here, we consider the matrix permeability is isotropic. It means k_m is same at both *x* and *y* directions.

At this point, the implementation of Fracture-Cell model is finished. The flowing works are upscaling based on the geostatistically representative fracture pattern.

3.2.2 Capturing Fracture Pattern with Different Cell Quantities

The Fracture-Cell Model is applied to the geostatistics generated fracture pattern with reduced cell quantities. **Figure 13** is fracture pattern generated by the geostatistics approach by Liu and Srinivasan (2002, 2004). The refined fracture pattern is a 100 × 100 cells scale which is 1000 *ft* × 1000 *ft* reservoir. The gray dyed cells are fracture cells while blank area is matrix. Four producers are perforated along *x* direction that intersect fractures on the far north edge of the reservoir.

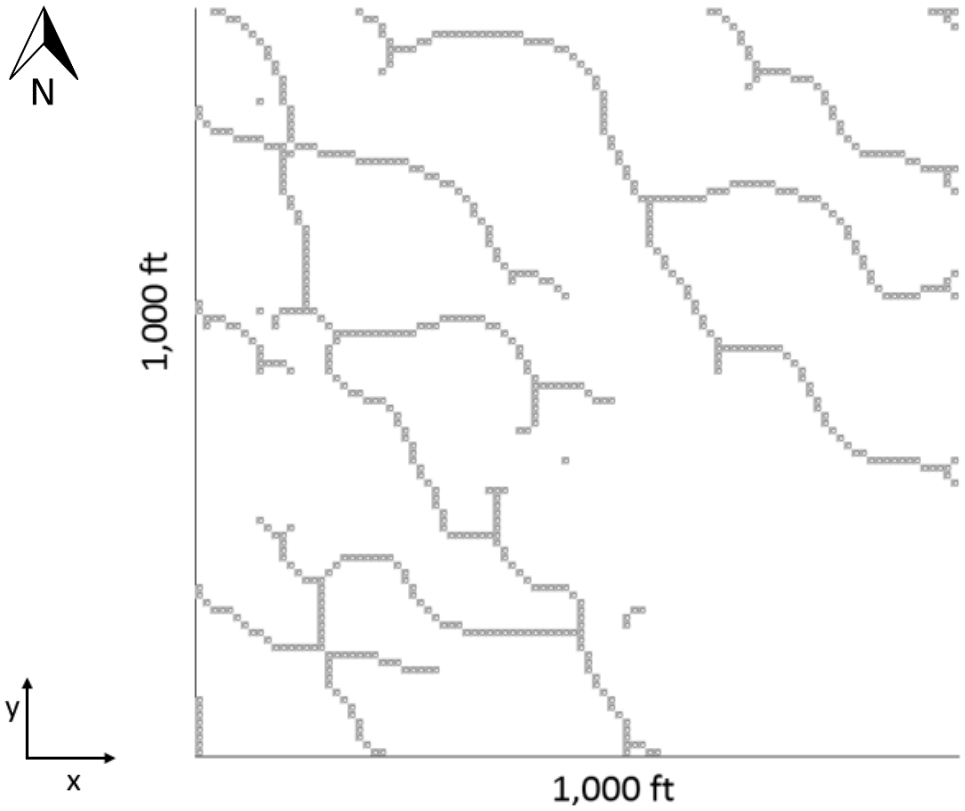

Figure 13. The reservoir dimensions of geostatistically generated pattern.

In this refined model, the grey gridblocks are actual fractures. The width of the fracture is assumed to be 1 mm while the *h* in the refined model is 10 ft. therefore, the fracture permeability is equal to 30.292 darcies. The difference between refined model and Fracture-Cell model is that in the fracture cell model, the cells with fracture paths are not fully occupied by the fracture paths while the cells are full occupied by the fracture in refined model in showing **Figure 13**.

It was concluded that the fractures that are not connect to the producers do not have contributions to the productions (Sakhaee-Pour and Wheeler 2016). As for the simplicity, the disconnected fractures on the southeast region showing in the **Figure 13** are neglected in the simulation.

Figure 14 shows the upscaling patterns (reduced models) of 20 × 20 cells, 40 × 40 cells, 80 × 80 cells from **Figure 14 (a)** to **Figure 14 (c)** based the refined model with 100 × 100 cells **Figure 14 (d)**. It is clear that the 80 × 80 cells pattern is close enough to the refined model with 100 × 100 cells. By comparing **Figure 14 (d)** to **Figure 13**, we can notice that some cells are modified to connect to adjacent cells to ensure the flow transient to pass.

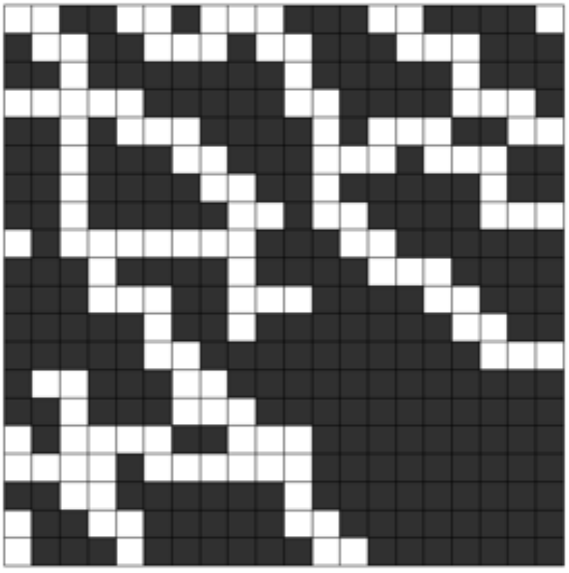

Figure 14 (a)

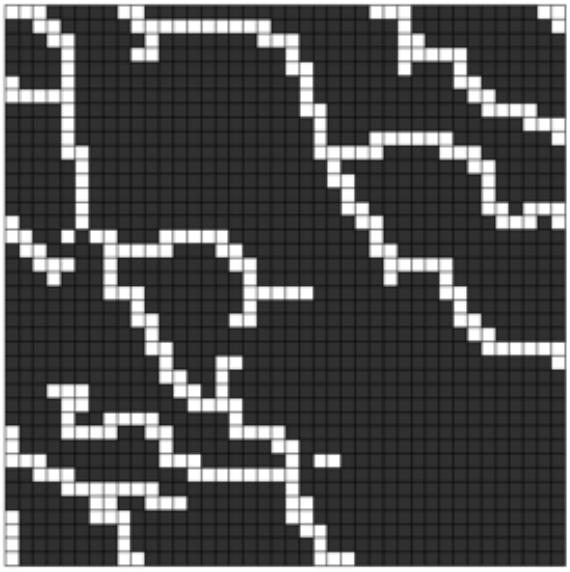

Figure 14 (b)

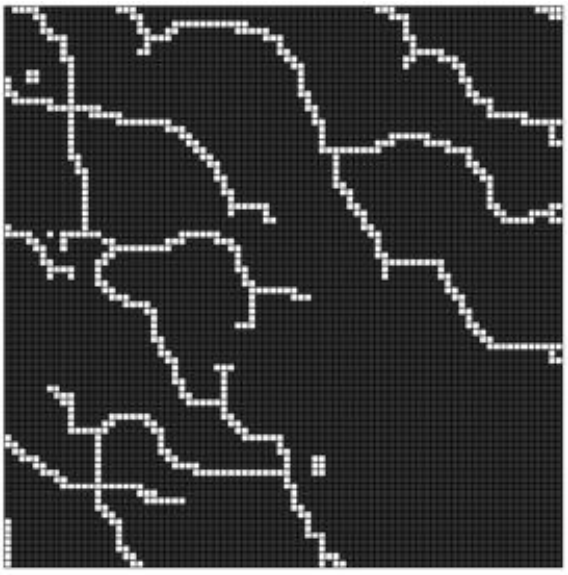

Figure 14 (c)

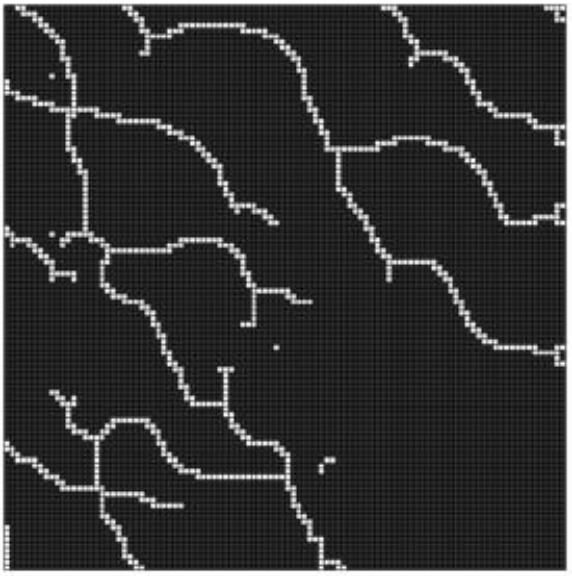

Figure 14 (d)

Figure 14. reduced pattern (a) to (c) and the refined pattern (d).

Chapter 4: Reservoir Simulation

4.1 Homogenous Case

The reservoir fluid type is black oil in our study. Two phases, including oil and water, are set in the reservoir. Therefore, the relative permeability and capillary pressure relationship with wetting phase saturation are defined in here.

The two-phase reservoir is ensured by controlling the bubble point pressure of generated fluid lower than the bottom hole flowing pressure (p_{wf} = 2000 psi).

The Corey model is used to describe the relative permeability relationship with the wetting phase saturation in the simulator:

$$k_{rw} = k_{rw}^{o}\overline{S}^{e_w} \tag{17}$$

$$k_{ro} = k_{ro}^{o}(1 - \overline{S})^{e_0} \tag{18}$$

Where k_{rw}^{o}, e_w , k_{ro}^{o} and e_0 are the pertinent parameters obtained from laboratory measurement.

In the equations above, $\overline{S}$ is the normalized wetting phase saturation. It is calculated by

$$\overline{S} = \frac{S_w - S_{wr}}{1 - S_{wr} - S_{or}} \tag{19}$$

Where S_{wr} is residual wetting phase (water in this study) saturation, S_{or} is the residual non-wetting phase (oil in this study) saturation.

The matrix capillary pressure affects two phase flow in the tight formations dramatically. In addition, fracture does not have capillary pressure effect due to its structure. In order to successfully run the simulator, a very small number of capillarity will be assigned to the fracture. The matrix capillary pressure is calculated by Van Genuchten Model:

$$p_c = \frac{1}{\alpha}\left(\overline{S}^{-\frac{1}{m}} - 1\right)^{1-m} \tag{20}$$

Where α and m are empirical parameters obtained from the laboratory measurements. Here α is assigned with value of 0.04, 0.0013 and 0.0004 for k_m = 1 μd, k_m = 100 nd and k_m = 10 nd; m input is 0.87.

The relative permeability data and capillary pressure data are summarized in **Table 1**.

Table 1. Relative permeability and capillarity for both matrix and fracture.

Matrix						Fracture					
Sw	Krw	Krow	Pc (km=1 μd)	Pc (km=100 nd)	Pc (km=10 nd)	Sw	Krw	Krow	Pc (km=1 μd)	Pc (km=100 nd)	Pc (km=10 nd)
0.2	0.0000	0.8000	383.5	1180.0	3835.0	0.05	0.0000	0.9000	0.40	1.22	3.97
0.24	0.0000	0.7031	376.3	1157.7	3762.6	0.11	0.0000	0.7416	0.39	1.20	3.90
0.28	0.0000	0.6125	336.9	1036.5	3368.7	0.16	0.0000	0.6029	0.36	1.12	3.64
0.31	0.0002	0.5281	314.5	967.8	3145.3	0.22	0.0001	0.4827	0.35	1.09	3.53
0.35	0.0008	0.4500	298.6	918.7	2985.9	0.28	0.0004	0.3797	0.34	1.05	3.41
0.39	0.0019	0.3781	285.9	879.7	2859.0	0.33	0.0012	0.2925	0.33	1.00	3.25
0.43	0.0040	0.3125	275.1	846.5	2751.0	0.39	0.0030	0.2197	0.31	0.96	3.12
0.46	0.0073	0.2531	265.5	816.8	2654.5	0.44	0.0064	0.1602	0.30	0.92	2.99
0.5	0.0125	0.2000	256.5	789.2	2565.0	0.5	0.0125	0.1125	0.29	0.88	2.86
0.54	0.0200	0.1531	247.9	762.8	2479.1	0.56	0.0225	0.0754	0.27	0.84	2.73
0.58	0.0305	0.1125	239.4	736.6	2393.9	0.61	0.0381	0.0475	0.26	0.80	2.60
0.61	0.0447	0.0781	230.7	709.7	2306.6	0.67	0.0614	0.0275	0.25	0.76	2.47
0.65	0.0633	0.0500	221.3	681.0	2213.4	0.73	0.0949	0.0141	0.23	0.72	2.34
0.69	0.0872	0.0281	210.8	648.7	2108.3	0.78	0.1416	0.0059	0.22	0.68	2.21
0.73	0.1172	0.0125	197.9	609.0	1979.3	0.84	0.2052	0.0018	0.21	0.64	2.08
0.76	0.1545	0.0031	179.1	551.2	1791.4	0.89	0.2897	0.0002	0.20	0.60	1.95
0.8	0.2000	0.0000	0.0	0.0	0.0	0.95	0.4000	0.0000	0.00	0.00	0.00

Figure 15 shows relative permeability curves and capillary pressure for both matrix cells and fracture cells. Since the relative permeability in the multiphase flow tight reservoir is still an active research, the Corey model is employed to express the relative permeability relationship with wetting phase saturation for the simplicity. The fracture in here is not assumed to be the smooth conduit when the surface roughness of the fracture is considered. In addition, in the Fracture-Cell model, the fracture cells contain both the fracture parts and the matrix parts. Therefore, the relative permeability curves of the fracture cells do not have constant slop. **Figure 16** shows the capillary pressure curves for permeability of 1 μd, 100 nd and 10 nd scenarios. The Van Genuchten capillary pressure model is used in our model since it has better ability to express the non-percolating characteristics of the capillary pressure relationship with the wetting phase saturation in shales. As it is showing in the **Figure 16**, the capillary pressures are abnormally high when we used the empirical coefficients that are obtained from laboratory measurement in Van Genuchten model. It could be explained by the inconsistent hydraulic connections to the surface. The geological barriers maybe exist in the system, causing the extreme high fluid pressure.

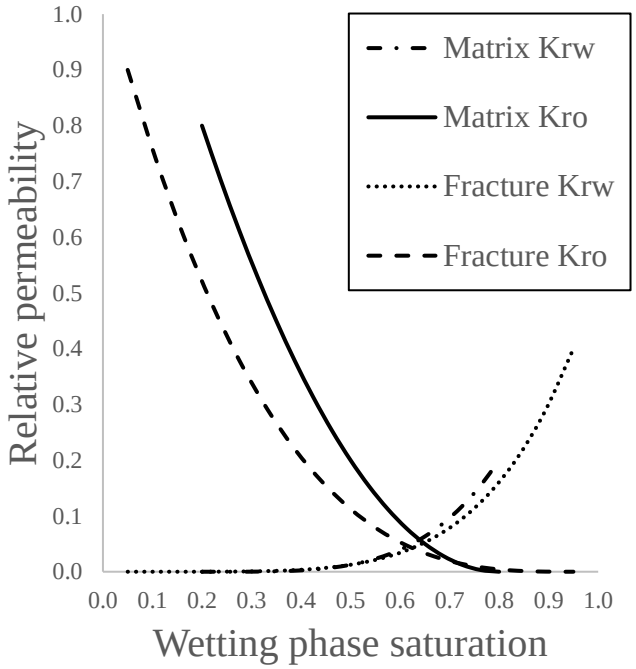

Figure 15. Relative permeability curves for both fracture cells and matrix cells.

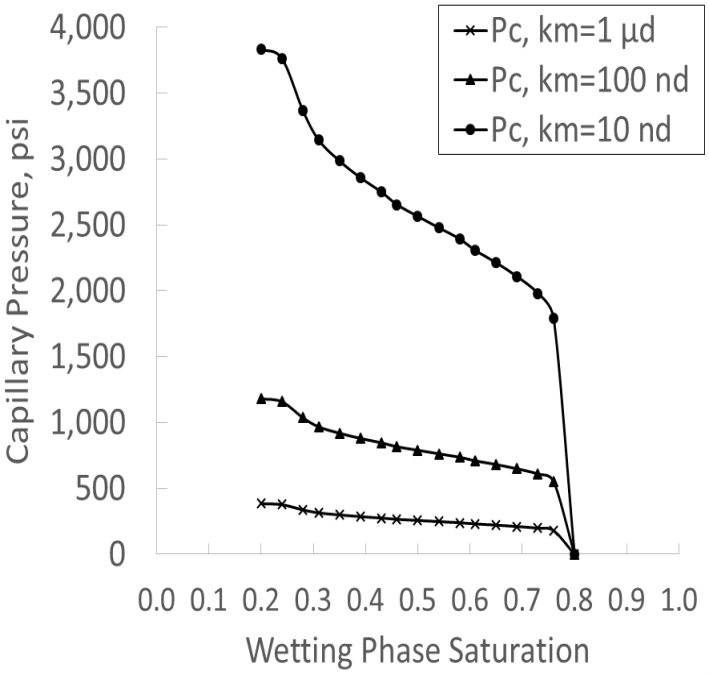

Figure 16. Capillary pressure curves for fracture for 1 µd, 100 nd and 10 nd.

As for the practical use of the simulator, in order to assign the fracture cells and matrix cells to different relative permeability relationships and capillarities, it is advisable to generate two rock types in the simulator. The fracture cells and matrix cells are assigned to two rock types separately.

Table 2 summarized the input data of the simulation.

Table 2. Input data for two-phase simulation of Fracture-Cell model.

Property	Value
Physical dimension	1000 ft × 1000 ft
Porosity/mean of porosity in heterogeneous cases	0.08
Corey model parameters (k_{rw}^{o}, k_{ro}^{o}, e_w, e_o)	(0.2, 0.8, 4.0, 2.0)
Mean/standard deviation of normal distribution for porosity	0.08, 0.01
Log Mean (k_m =1 μd, 100 nd, 10 nd) / log standard deviation of lognormal distribution for permeability	(-3, -4, -5) md / 0.02 md
Residual water/oil saturation of matrix	0.2, 0.2
Residual water/oil saturation of fracture	0.05, 0.05
Initial oil pressure	4000 psi
Bottom-hole pressure	2000 psi
Grid number	20 × 20, 40 × 40, 80 × 80, 100 × 100
Oil compressibility	1.0 E-6 (1/psi)
Oil viscosity	0.3 cp
Formation volume factor	1.0 RB/STB

The initial water saturation of matrix cells is 0.4 while it is 0.05 of the fracture cells. Four producers are located in the North side of *y* axis along the *x* axis and intersected fracture cells.

4.2 Heterogeneous Case

4.2.1 *J-Function Scaling*

In a same reservoir, the heterogeneous permeabilities results in the heterogeneous capillary pressure (Saadatpoor, Bryant and Sepehrnoori 2010). The Leverett *J* –function is widely used to count the heterogeneity capillary pressures in the same reservoir (Leverett 1941). The *J* function is calculated by

$$J(S_w) = \frac{p_c}{\sigma\, cos\theta}\sqrt{\frac{k}{\phi}} \tag{21}$$

where S_w is the wetting phase saturation, p_c is the capillary pressure, ϕ is the porosity, σ is the surface tension, θ is the contact angle and k is the absolute permeability of the rock. Rocks that are from the same field or share the same lithology have same *J* function setting to normalize the capillarity. The equation (21) explicitly shows that the differences of capillary pressures are caused by the wetting properties, heterogeneous permeabilities and porosities.

In our study, two assumptions are made regarding heterogeneous capillary pressure: first, the interfacial tension and contact angle do not change; second, the capillary pressure shape remains same. The capillary pressure variations can be obtained based on the reference capillary pressure and their permeabilities and porosities showing in equation below:

$$P_{c2}(s_w) = P_{c1}(s_w)\sqrt{\frac{k_1}{k_2}\frac{\phi_1}{\phi_2}} \tag{22}$$

Then the *J* function is implemented in the simulator as normalized expression of the heterogeneous capillary pressures.

4.2.2 *Subsurface Uncertainty*

In the heterogeneous reservoir, the porosity is normally distributed while the permeability appears to be log-normally distributed. In our study, the permeability heterogeneity and the porosity heterogeneity of the tight formations are specified by utilizing these two distributions. The random permeability value is sampled from the specified log-normal distribution and assigned to the matrix cells locations. Similarly, the random porosity value is sampled from the specified normal distribution and assigned to cells. Again, this process introduced heterogeneous characteristics or uncertainties in the reservoirs.

In order to compare the homogeneous case with heterogeneous cases, the mean of the porosity normal distribution in the heterogeneous case is set with the porosity value in the homogeneous case (0.08). The random sampled matrix permeability values from log-normal distribution are assigned to the matrix cells. The modes of the permeabilities distributions have the same values of homogeneous permeability cases (1μd, 100 nd or *10* nd) with specified uncertainties in the log-normal distribution.

Figure 15 is an example of histogram graph for normally distributed porosity for 80 × 80 cells dimension. **Figure 16** gives an example of the matrix permeabilities histogram with log-normal distribution of the same dimension.

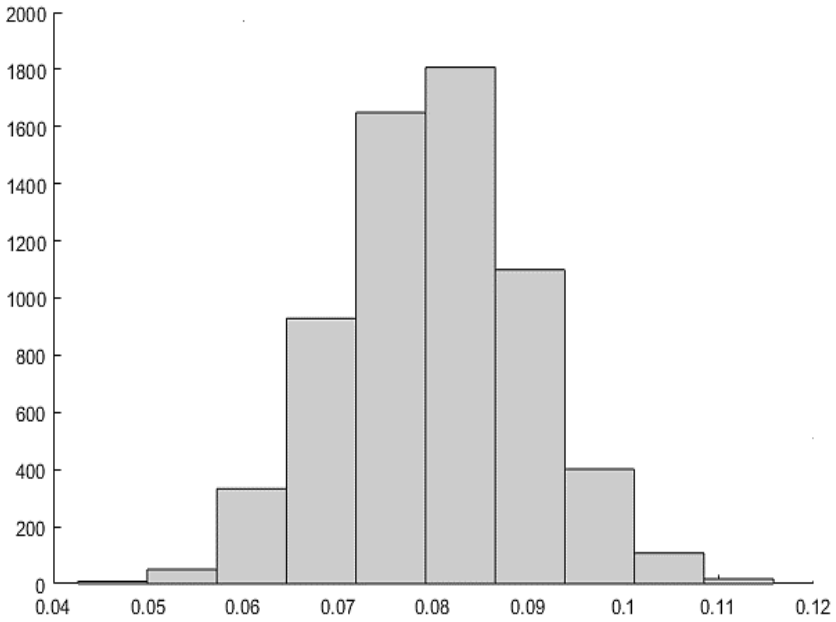

Figure 17. Histogram of the heterogeneous porosity distribution with 80 × 80 cells.

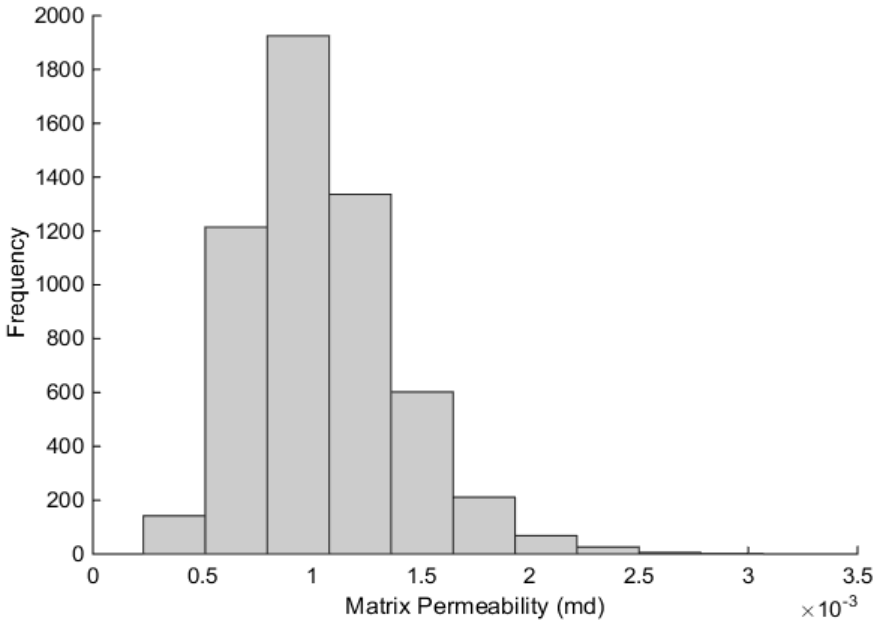

Figure 18. Histogram of matrix permeability distribution with 80 × 80 cells.

Five cases are designed in this study. The combinations of matrix permeability, porosity and capillary pressure regarding their heterogeneities are summarized in **Table 3** below.

Case 1 is with homogeneous matrix permeability, homogeneous porosity and homogeneous capillary pressure curve (without scaling). Case 2 is specified as heterogeneous matrix permeability, homogeneous porosity and heterogeneous capillary pressure with *J* function scaling. Case 3 is specified with heterogeneous matrix permeability, heterogeneous porosity and heterogeneous capillary pressure with *J* function scaling. Case 4 is specified with heterogeneous matrix permeability, homogeneous porosity and homogeneous capillary pressure (without scaling). Case 5 is specified with heterogeneous matrix permeability, heterogeneous porosity and homogeneous capillary pressure (without scaling).

Case 1 will be compared with case 3. The reason for this set of comparison is because case 1 is generally be used in the fractured reservoir simulation settings while case 3 is considered as a more realistic fractured reservoir condition. The effect of *J* function (formation heterogeneity) is investigated by comparing case 2 with case 4 and by comparing case 3 with case 5.

Table 3. Homogeneous case and heterogeneous cases numbering.

	Case 1	Case 2	Case 3	Case 4	Case 5
Matrix Permeability	Homogeneous	Heterogeneous	Heterogeneous	Heterogeneous	Heterogeneous
Porosity	Homogeneous	Homogeneous	Heterogeneous	Homogeneous	Heterogeneous
Capillarity	Homogeneous	Heterogeneous	Heterogeneous	Homogeneous	Homogeneous

Three scenarios, k_m= 1 µd, k_m= 100 nd and k_m= 10 nd, are considered in this research. Each scenario contains 5 cases that are summarized in the **Table 3**. Furthermore, each case was performed with 4 dimensions regarding different cell quantities. These

dimensions are 400 cells (20 × 20 cells) reduced model, 1600 cells (40 × 40 cells) reduced model, 6400 cells (80 × 80 cells) reduced model and 10,000 cells (100 ×100 cells) refined model. The refined model (10,000 cells) is geostatistics generated model which is considered as reference base model in this study.

From case 2 to case 5 in each scenario, the heterogeneous permeabilities and porosities are random generated with specified distributions. The random location are picked to assign the permeabilities and porosities. Therefore, huge uncertainties are inevitably introduced when we want to study the cumulative oil production from these heterogeneous reservoirs. As a results, enough realizations are needed to ensure a stable averaged representative EUR for that heterogeneous reservoir. A number of 50 realizations is selected in this study since it delivers stable averaged representative EUR for all heterogeneous cases.

Chapter 5: Results

5.1 Example of Realizations in Heterogeneous Cases and Representative Average

Figure 19 shows relationship between cumulative oil production and time with both realizations and representative average. The k_m=100 nd scenario with 80 × 80 cells dimension is shown in here. Again, due to the randomness location assignment of heterogeneous permeability and porosity values within their distributions, large uncertainties are introduced into the tight reservoir. The enough realizations should be performed to ensure the representative EUR for the heterogeneous cases. Therefore, from case 2 to case 5, each case was performed with 50 realizations with whom give stabilized representative average of EUR. The average curve is calculated and shown as dark solid curves in each graphs in **Figure 19**.

The range of the EUR realizations in case 2 is 10,000 STB to 150,000 STB. It is 10,000 STB to 250,000 STB in case 3. While the range of EUR is 28,000 STB to 330,000 STB in case 4 and it is 26,000 STB to 350,000 STB in case 5. From **Figure 19** and ranges of all heterogeneous cases, we can notice that the smaller ranges of EUR realiztions are shown in the heterogenous capillary pressure cases (case 2 and case 3). In other words, the heterogeneous capillary pressure scaling reduces the uncertainties of cumulative oil production estimation in the tight heterogeneous reservoirs.

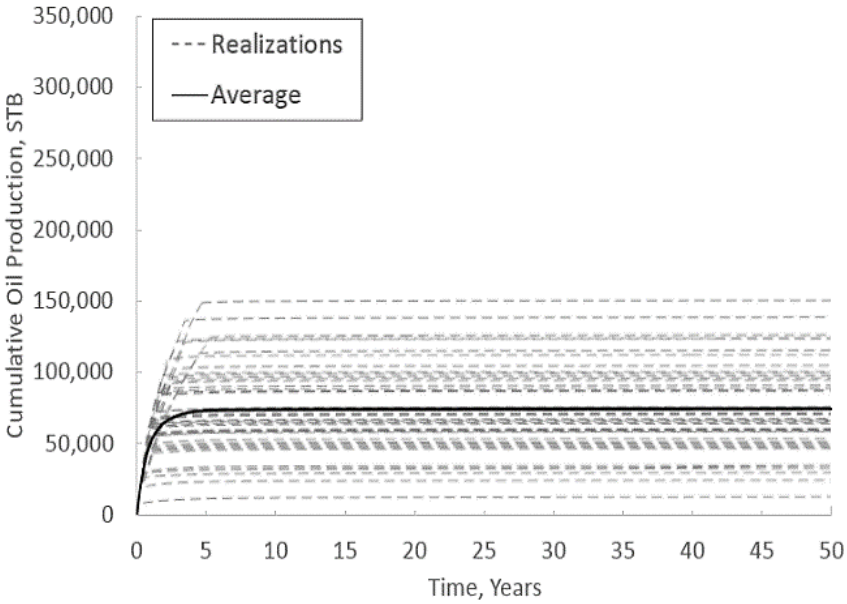

Figure 19 (a). Case 2

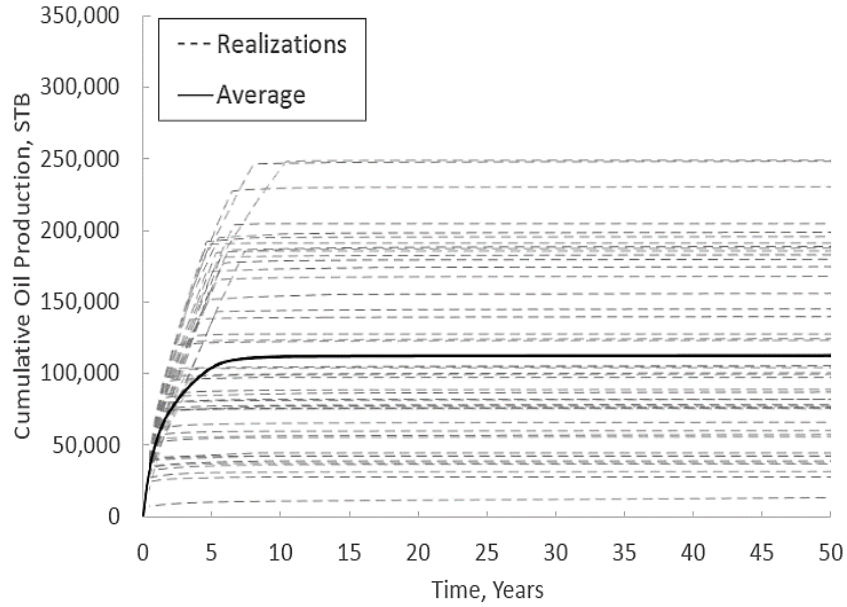

Figure 19 (b). Case 3

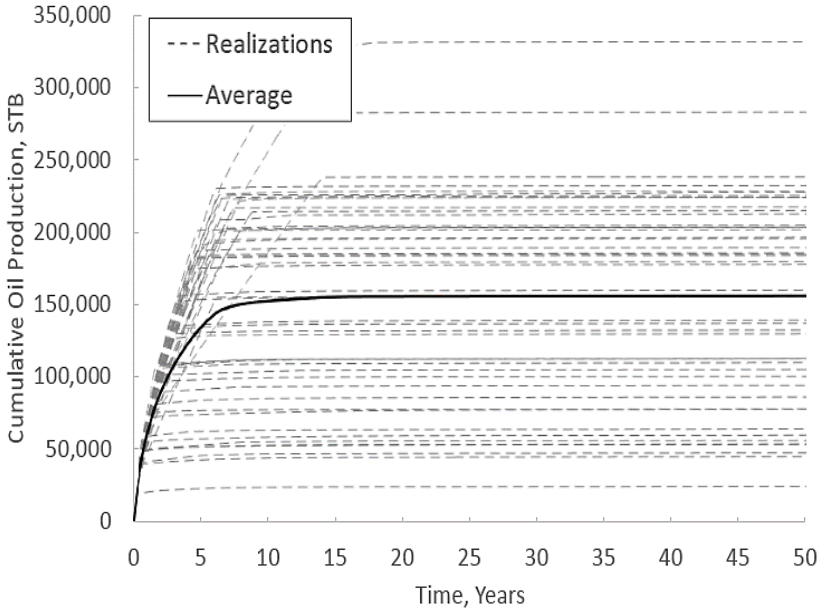

Figure 19 (c). Case 4

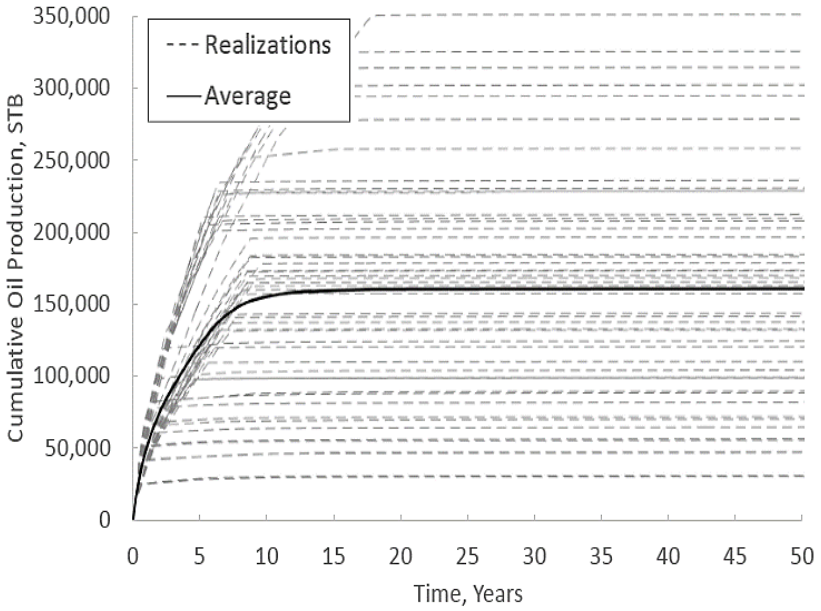

Figure 19 (d). Case 5

Figure 19. Average cumulative oil production curves with 50 realizations.

5.2 Cell Size Effect on Transport Properties of Heterogeneous Reservoir

The effect of mesh sizes was analyzed in the past for homogeneous reservoirs (Sakhaee-Pour and Wheeler 2016). Each graph in **Figure 20** shows the relationship between the cumulative oil production for 4 dimensions that we specified for both case 1 and case 3 with all three scenarios. Again, we use 100 × 100 cells dimension as the reference in this study.

We have to pay attention that this work is not an upscaling research. The initial setting for different dimensions are different. Specifically, the original oil in place in different dimensions vary due to the quantities of fracture cells vary from different dimensions (oil saturations for the matrix cell and the fracture cell are different). However, as for the 80 × 80 cells reduced model, it is more representative when we want to compare the Fracture-Cell model with 100 ×100 cells refined model (reference dimension). In other words, the 20 × 20 cells reduced model and the 40 × 40 cells reduced model are not representative Fracture-Cell models compared to our reference dimension.

In **Figure 20**, it is obvious that cumulative oil production of case 3 with 80 × 80 cells dimension in all permeability scenarios are fairly close to that of the references with acceptable uncertainties.

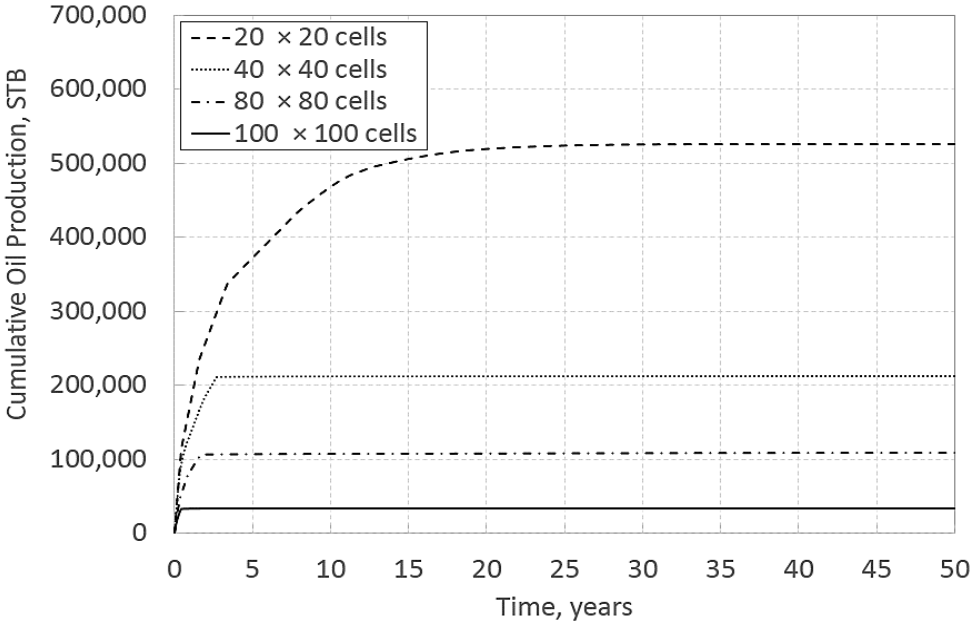

Figure 20 (a1). k_m =1 µd, Case 1

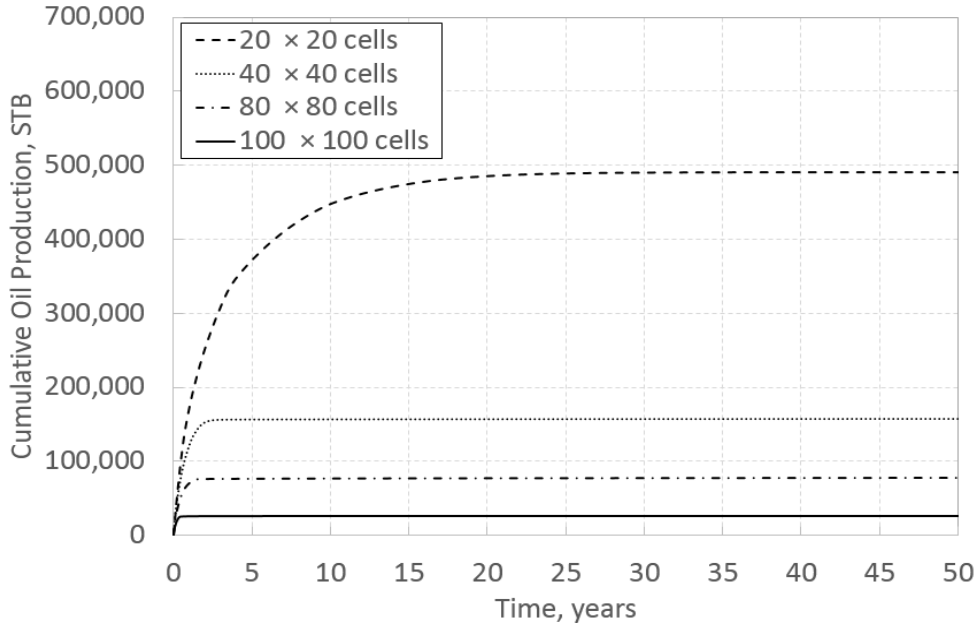

Figure 20 (a2). k_m =1 µd, Case 3

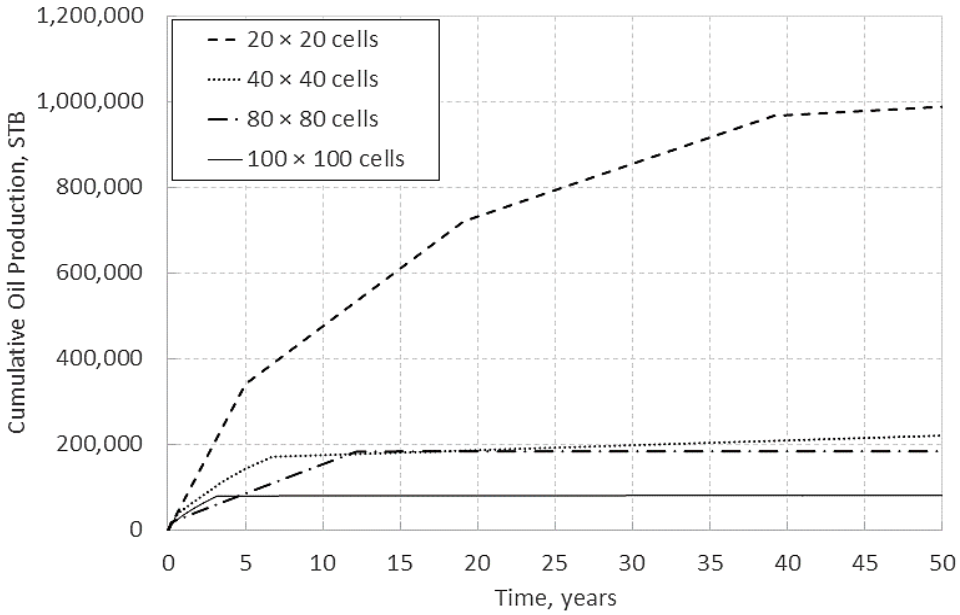

Figure 20 (b1). k_m=100 nd, Case 1

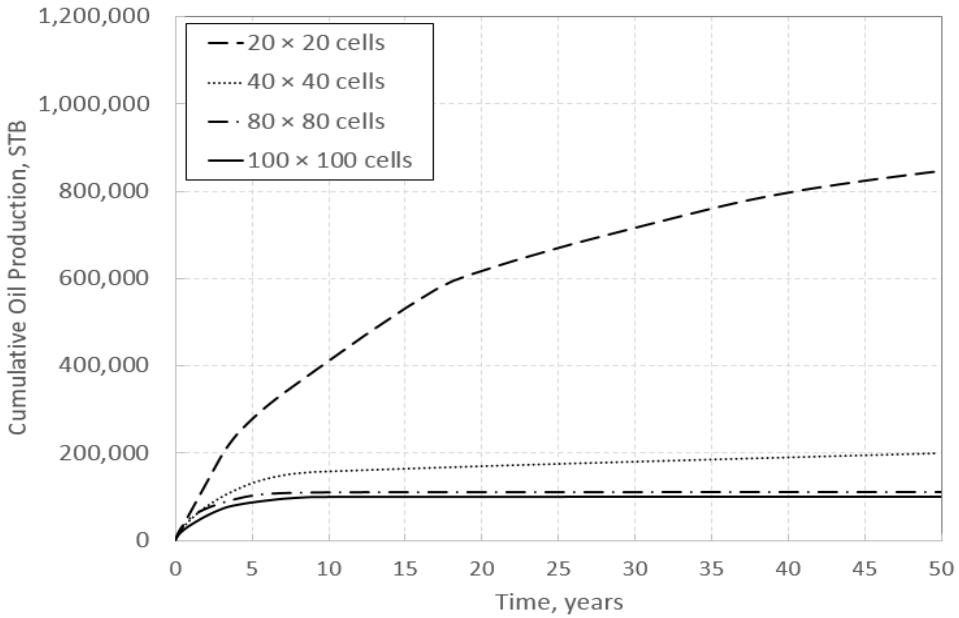

Figure 20 (b2). k_m=100 nd, Case 3

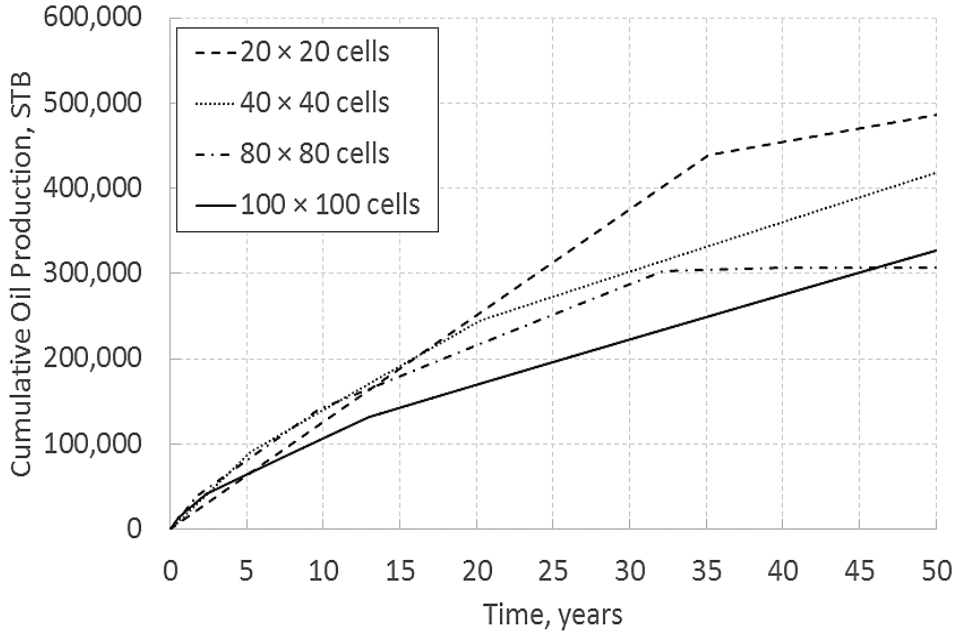

Figure 20 (C1). k_m=10 nd, Case 1

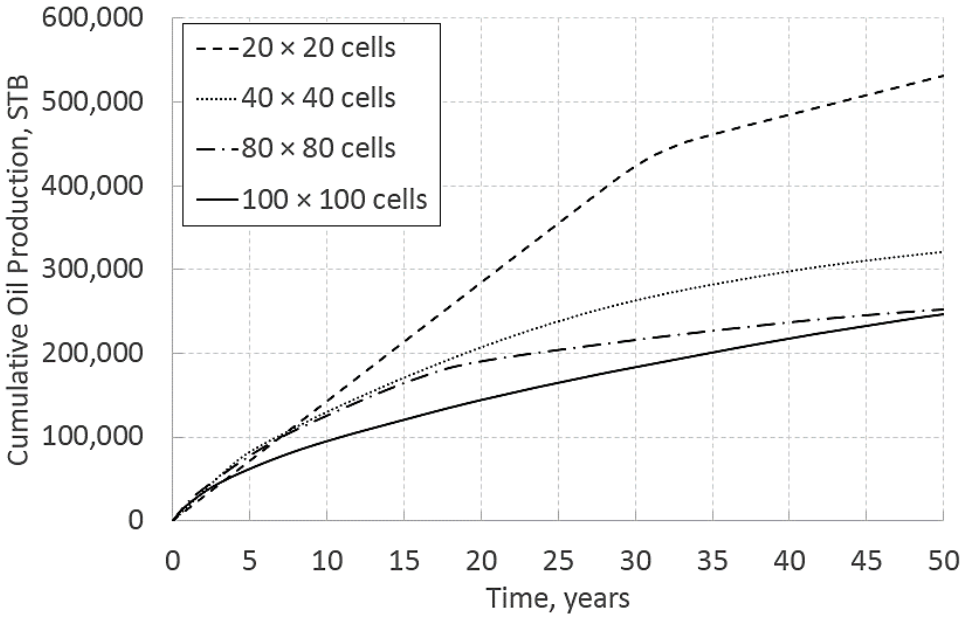

Figure 20 (C2). k_m=10 nd, Case 3

Figure 20. Cumulative oil production summary with time for first 50 years.

5.3 Effect of Reservoir Heterogeneity for 80 × 80 Cells

We compared the homogeneous case 1 with the most realistic heterogeneous condition case 3. Pressure profiles are showing below in **Figure 21**; the corresponding oil saturation profiles are showing in **Figure 22 and Figure 23** in two scales.

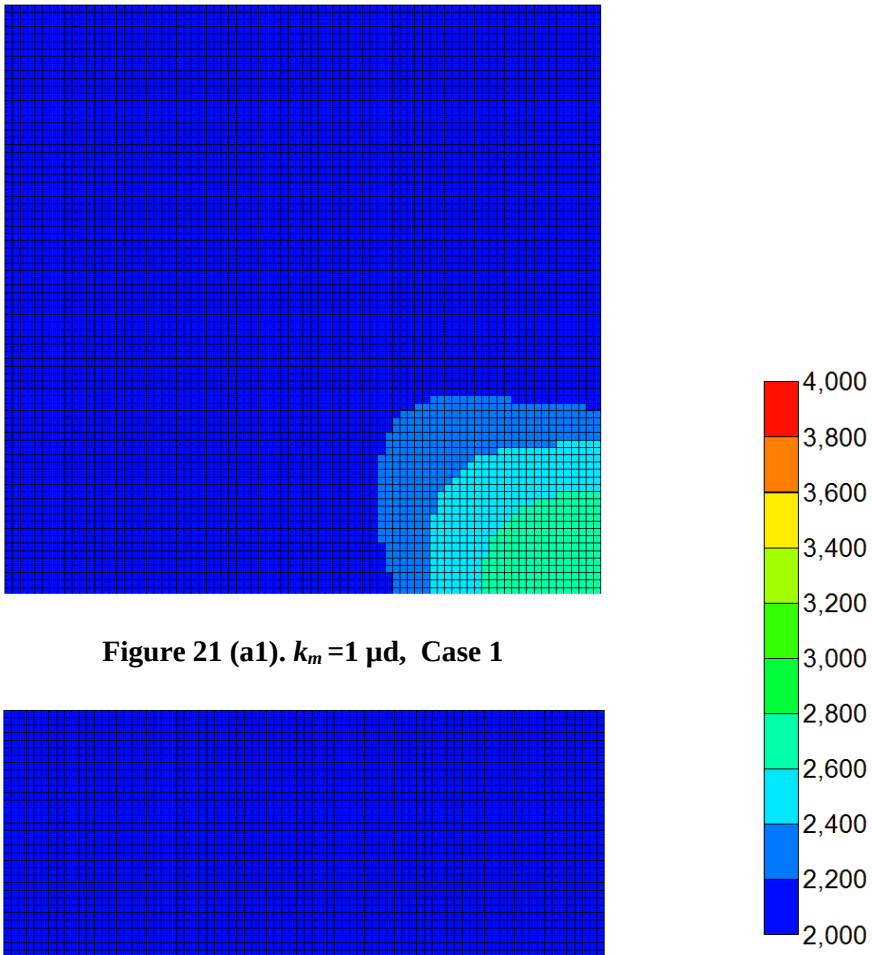

Figure 21 (a1). k_m =1 μd, Case 1

Figure 21 (a2). k_m =1 μd, Case 3

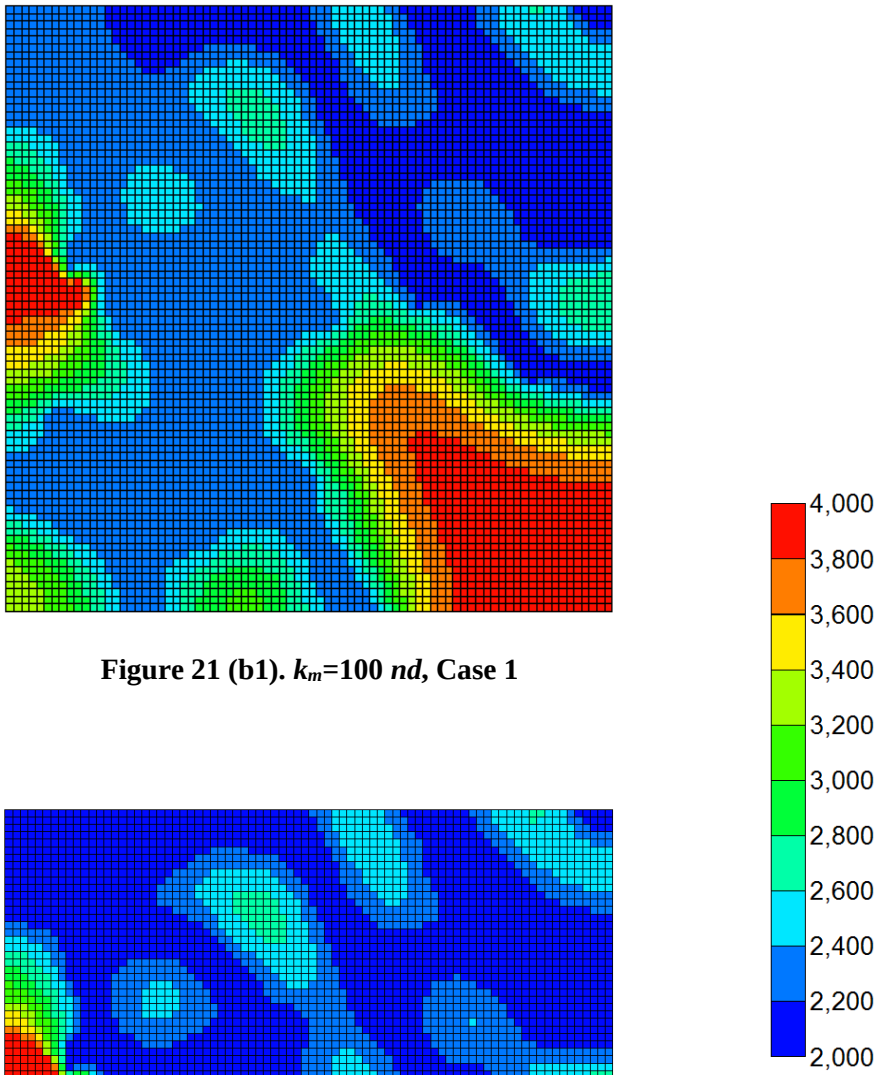

Figure 21 (b1). k_m**=100** ***nd*****, Case 1**

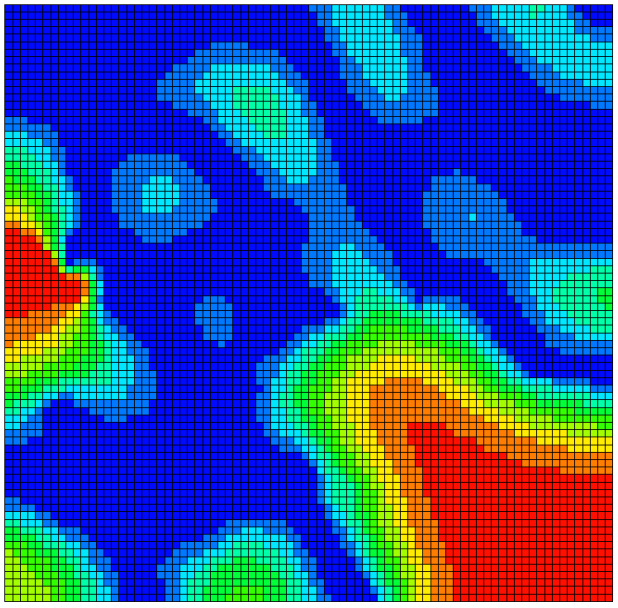

Figure 21 (b2). k_m**=100** ***nd*****, Case 3**

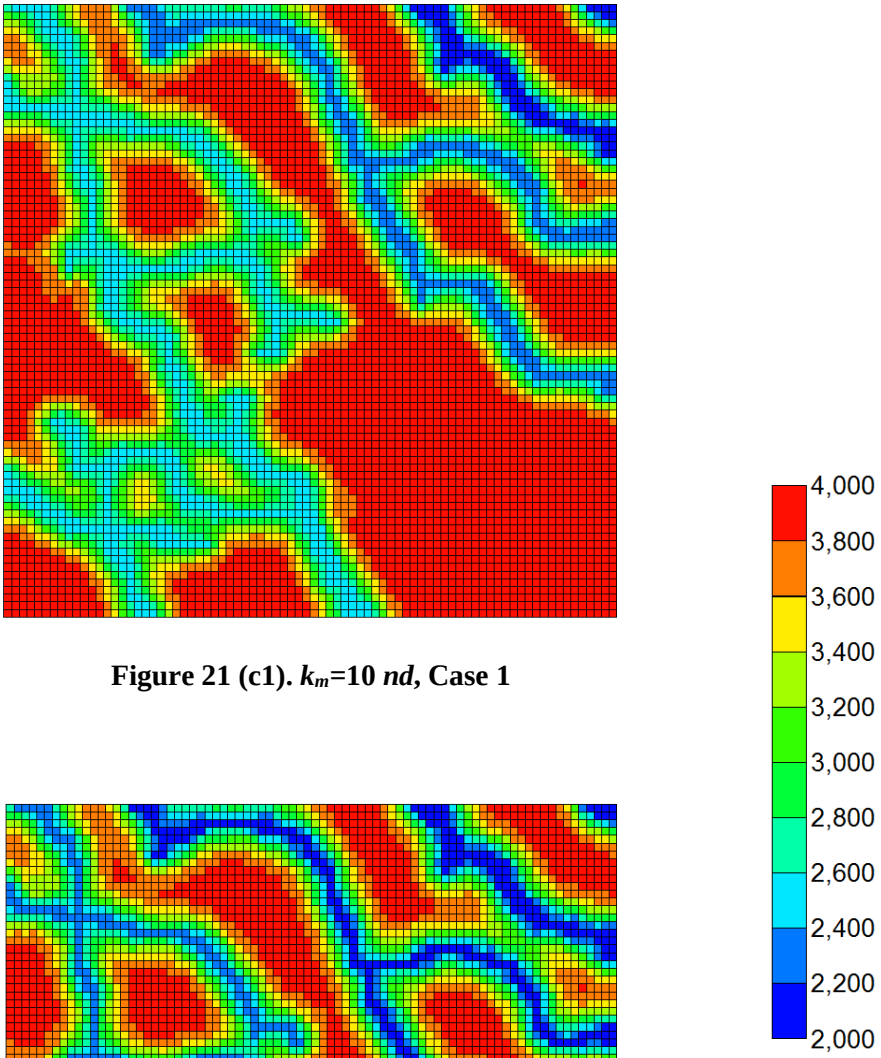

Figure 21 (c1). k_m**=10** ***nd*****, Case 1**

Figure 21 (c2). k_m**=10** ***nd*****, Case 3**

Figure 21. Pressure profiles after 7 years of production for 80 × 80 cells.

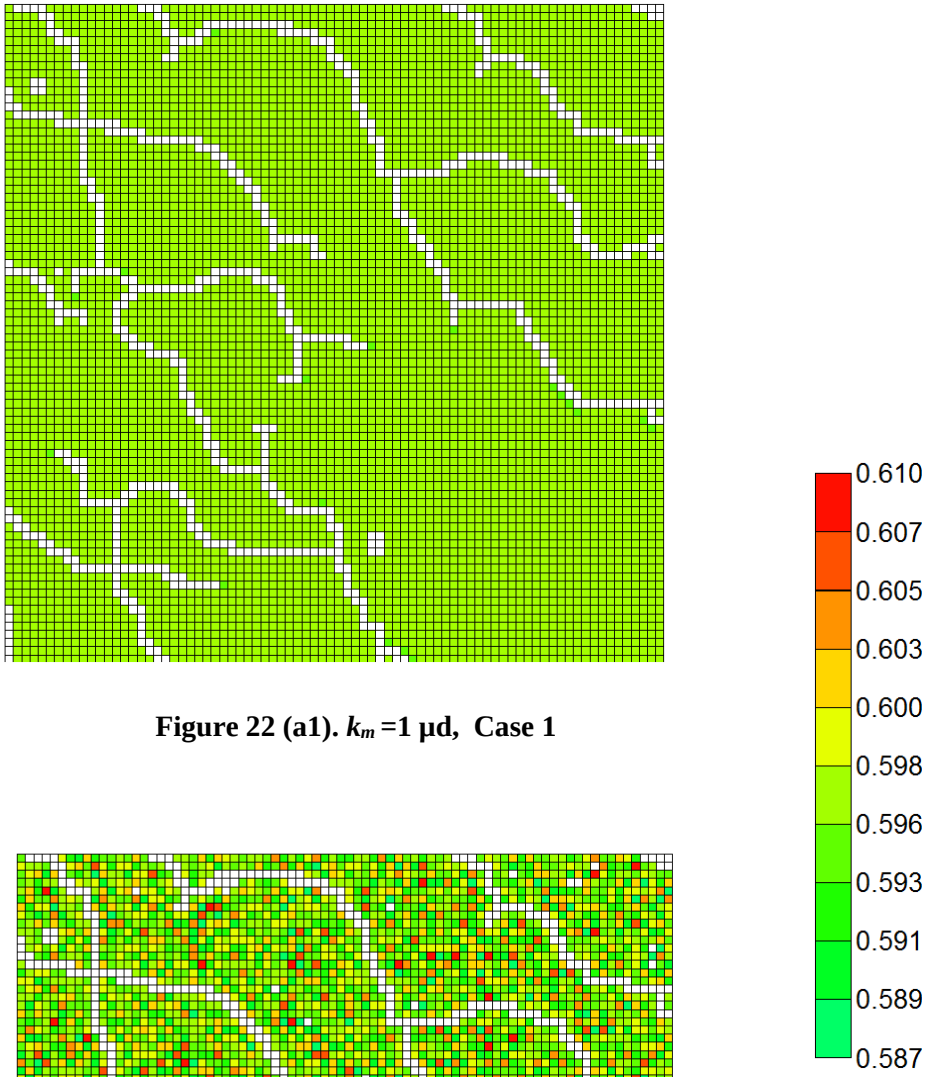

Figure 22 (a1). k_m **=1 μd, Case 1**

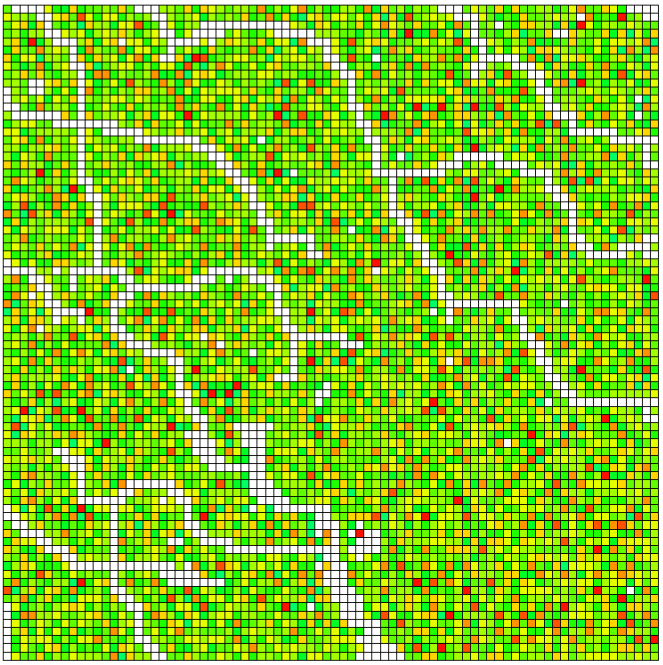

Figure 22 (a2). k_m **=1 μd, Case 3**

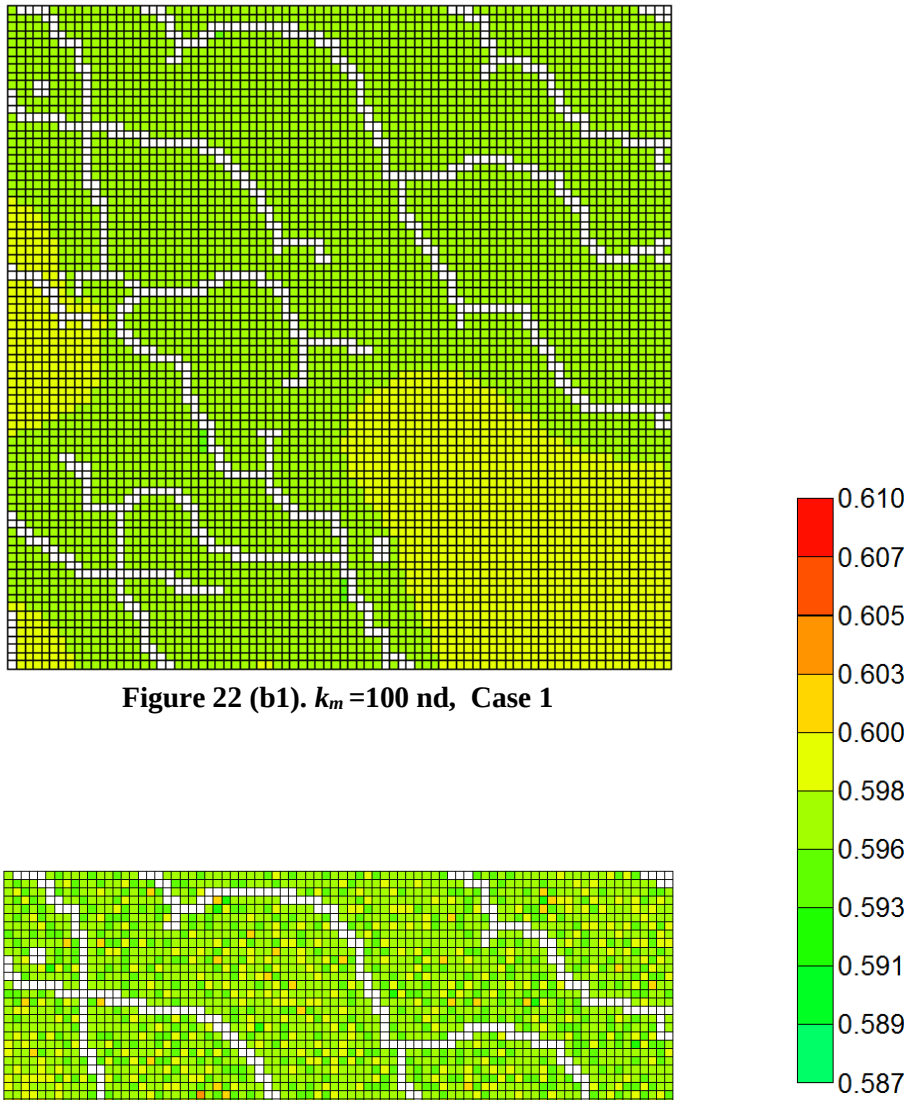

Figure 22 (b1). k_m =100 nd, Case 1

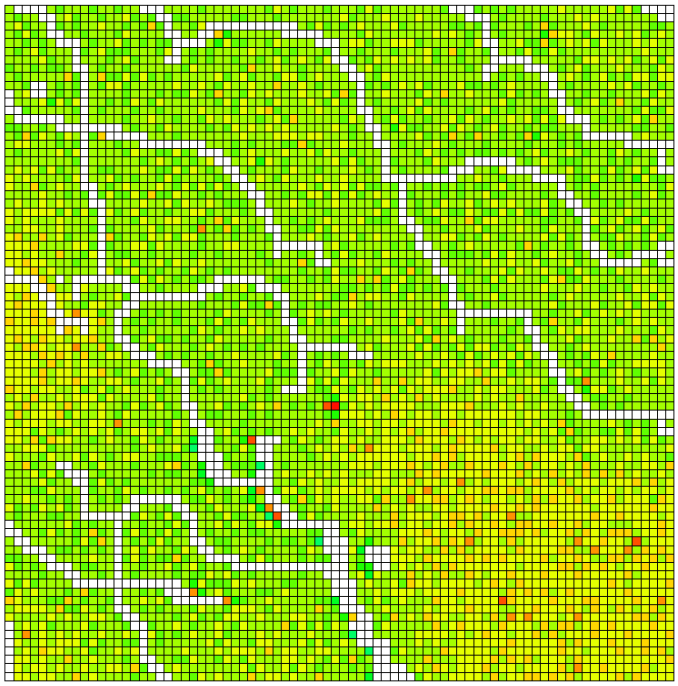

Figure 22 (b2). k_m =100 nd, Case 3

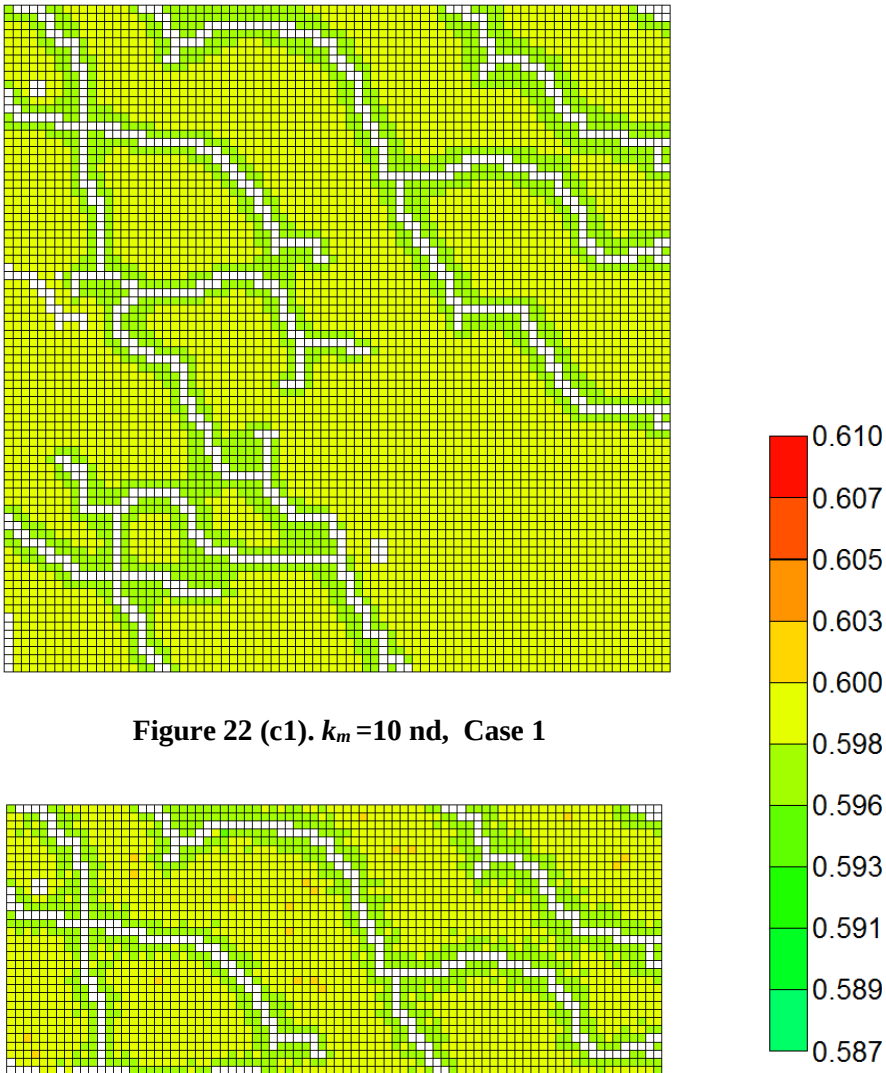

Figure 22 (c1). k_m **=10 nd, Case 1**

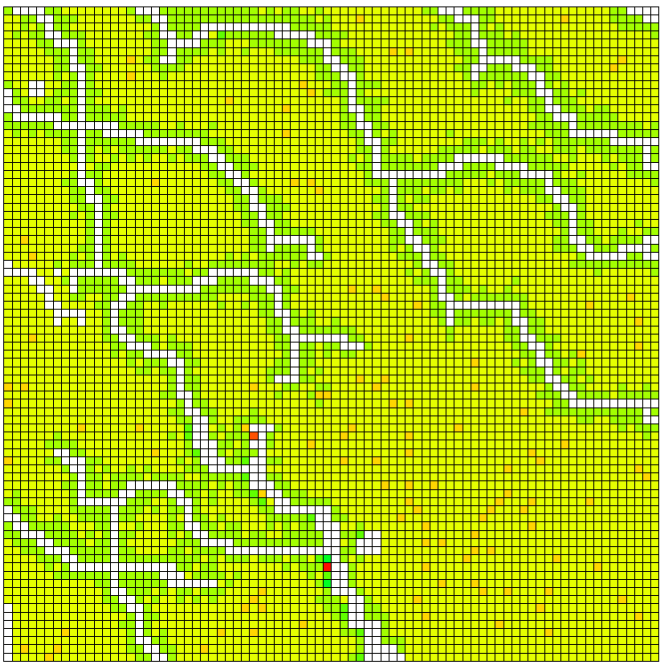

Figure 22 (c2). k_m **=10 nd, Case 3**

Figure 22. Oil saturation profiles after 7 years of production for 80 × 80 cells.

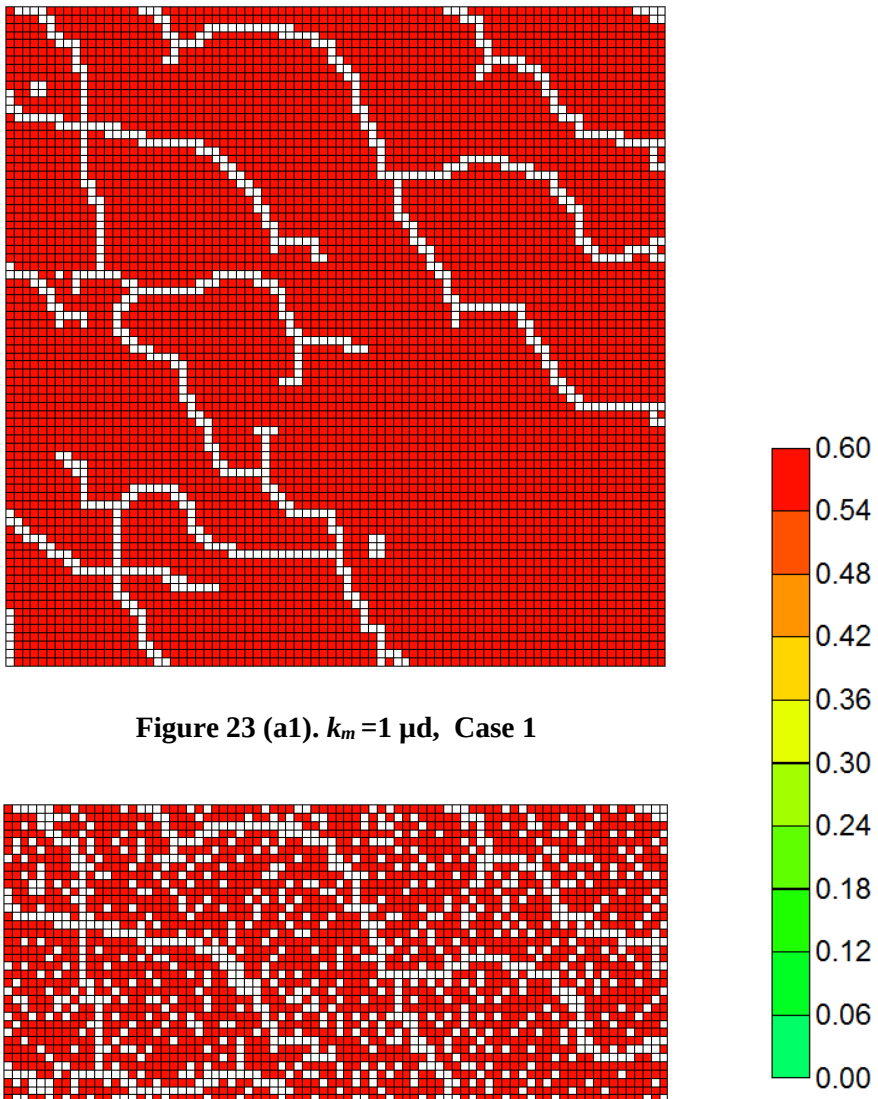

Figure 23 (a1). k_m **=1 μd, Case 1**

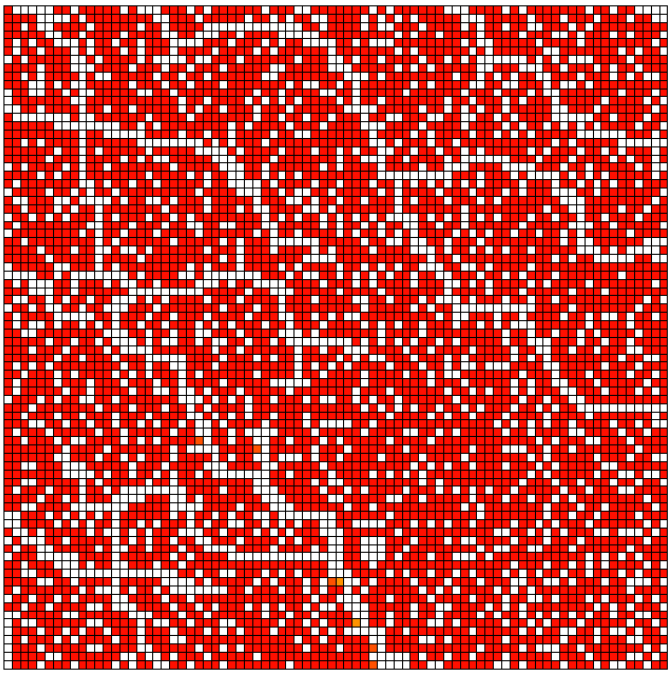

Figure 23 (a2). k_m **=1 μd, Case 3**

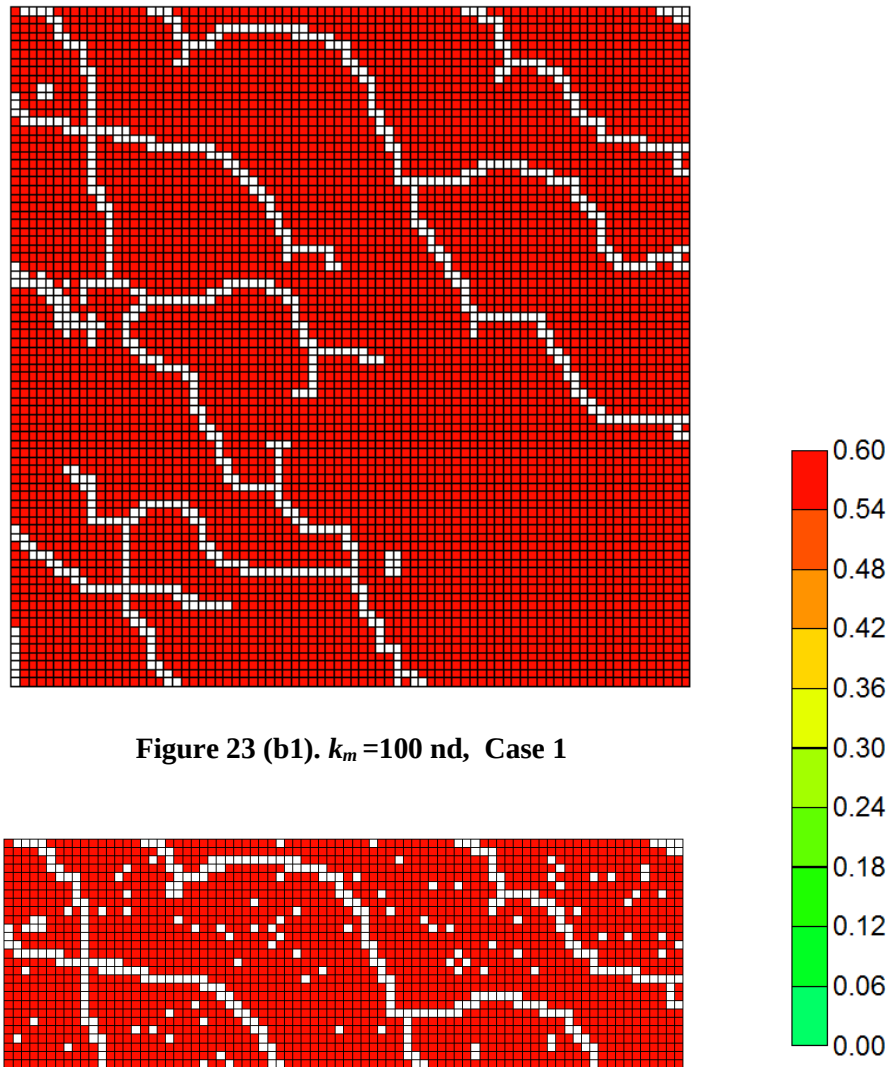

Figure 23 (b1). k_m **=100 nd, Case 1**

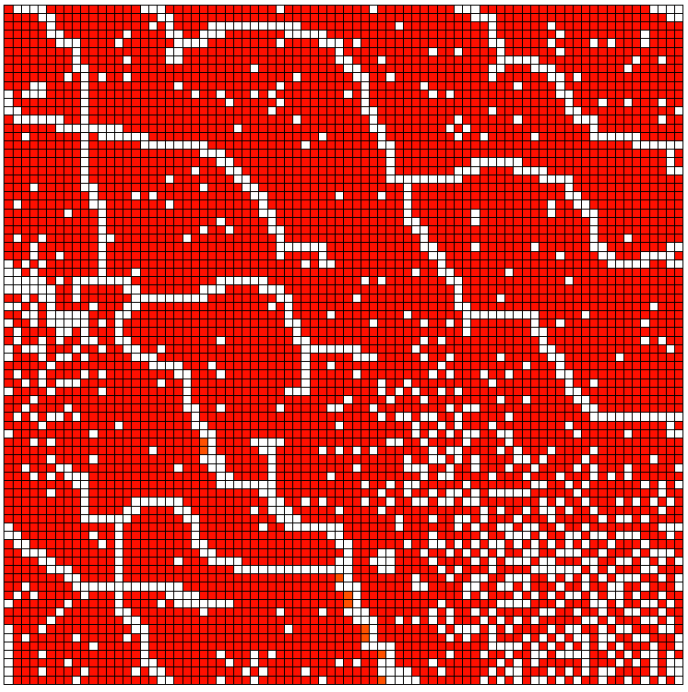

Figure 23 (b2). k_m **=100 nd, Case 3**

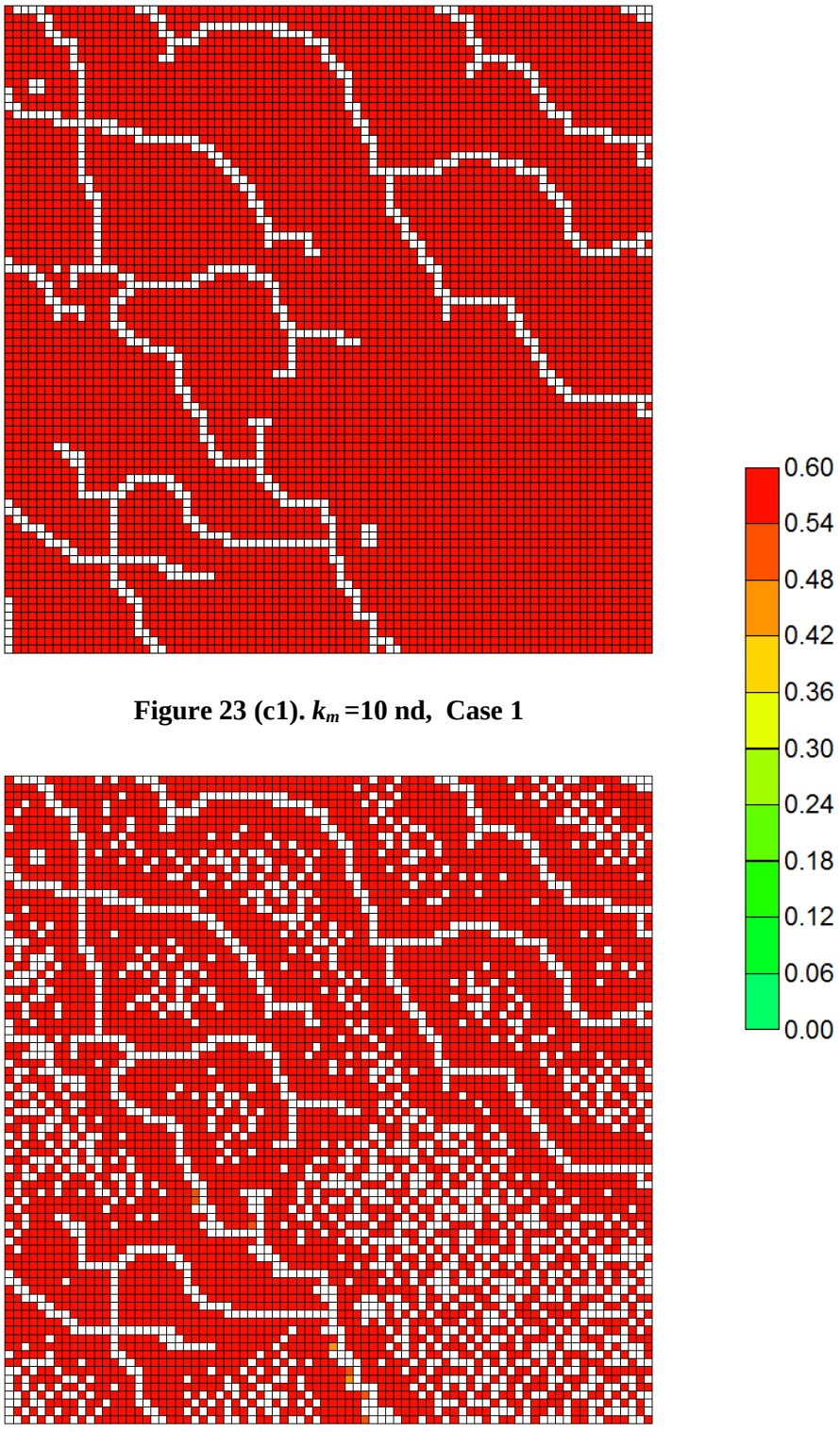

Figure 23 (c1). k_m **=10 nd, Case 1**

Figure 23 (c2). k_m **=10 nd, Case 3**

Figure 23. Saturations after 7 years for 80 × 80 cells in a different legend scale.

In the oil saturation profiles, we can observe the sharp fluid front in the homogeneous capillary pressure case in all scenarios while the gradually changed fluid saturation profiles are shown in the heterogeneous capillary pressure case in the oil saturation profile. This gradually changed fluid front is called ramified fluid front.

In addition, there are some extremely high oil saturation cells. There are two possibilities for this phenomenon. First, the local capillary trapping causes ultra difficulties for oil to flow in the tight formation. Second, the numerical dispersion occurred during the simulation.

5.4 Effect of *J* Function on Developing a Representative Model for 80 × 80 Cells

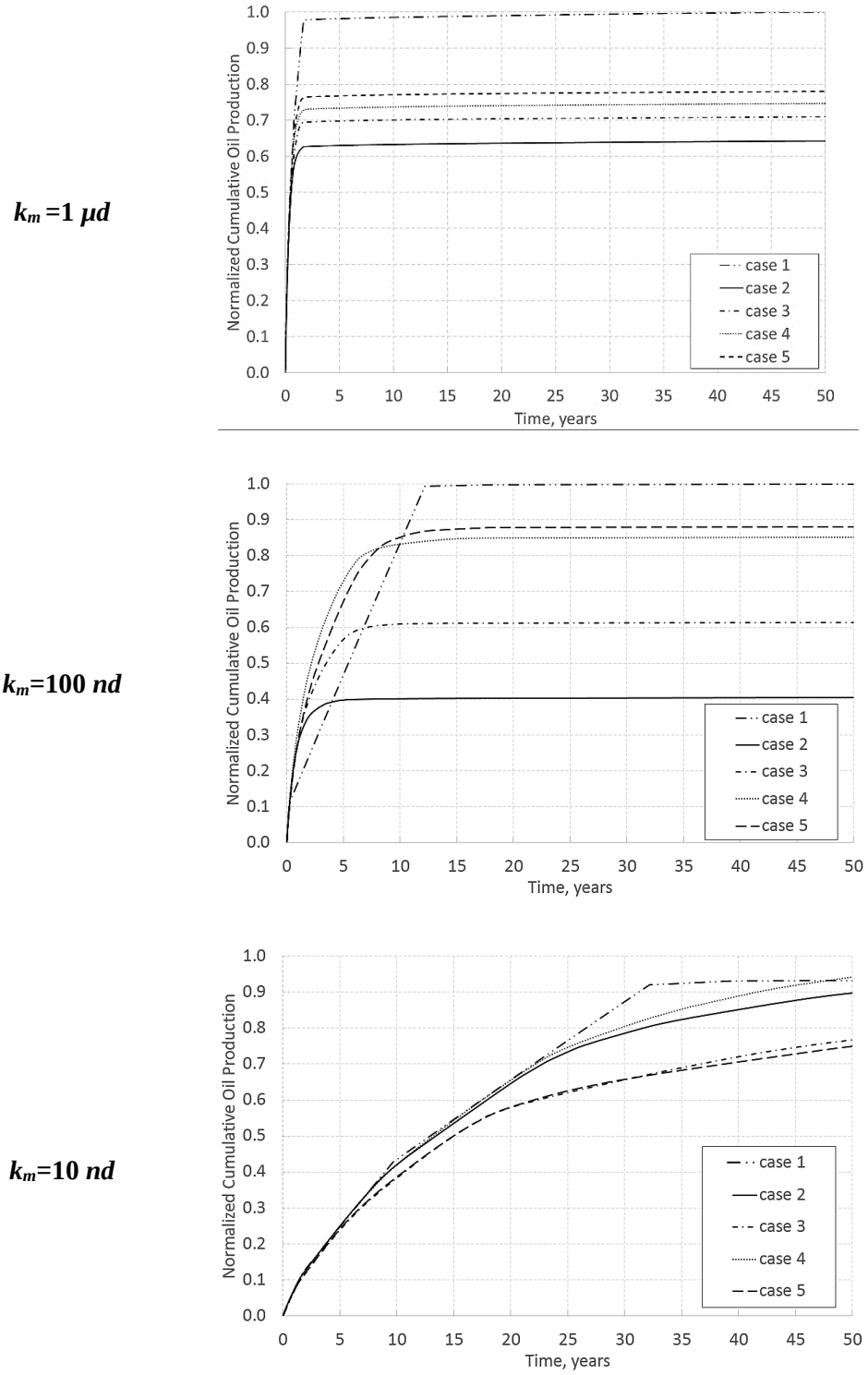

Figure 24. Cumulative production with time for first 50 years with 80 × 80 cells.

The **Figure 24** above summarized the three different matrix permeability scenarios of five cases for 80 × 80 cells dimension. The first two scenarios reached plateau in the cumulative oil production graph while the cumulative production for heterogeneous cases are still increasing for the last scenario. For first two scenarios, same decreasing trend for 5 cases within the scenario is observed: case 1> case 5> case 4> case 3>case 2.

As for investigating the effect of the *J* function (heterogenous capillary pressure) on EUR in the tight formation, case 2 will be compared with case 4 while the case 3 will be compared with case 5. The decreasing trends from both comparison are observed. So we can conclude that the heterogenous capillary pressure apprearence in the tight reservoir reduce the cumulative oil production from that of the homogenous capillary pressure.

The two aspect of comparisons that we discussed are summarized in the **Table 4** below. Noting that the first two scenarios are used to make the EUR conclusions, since the cumulative production curves of last scenario has not reached plateau in the current time span.

Table 4. Trend summary for 50 years with 80 × 80 cells.

Trend Summary			
	Capillary pressure heterogeneity		Homogeneous to heterogeneous (capillarity, permeability, porosity)
	case 4 to case 2	case 5 to case 3	case 1 to case 3
k_m =1 μd	↓	↓	↓
k_m=100 nd	↓	↓	↓
k_m=10 nd	↓	↑	↓

Case 2 vs case 4

The pressure and oil saturation profiles after 7 years of production are showing below for case 2 and case 4.

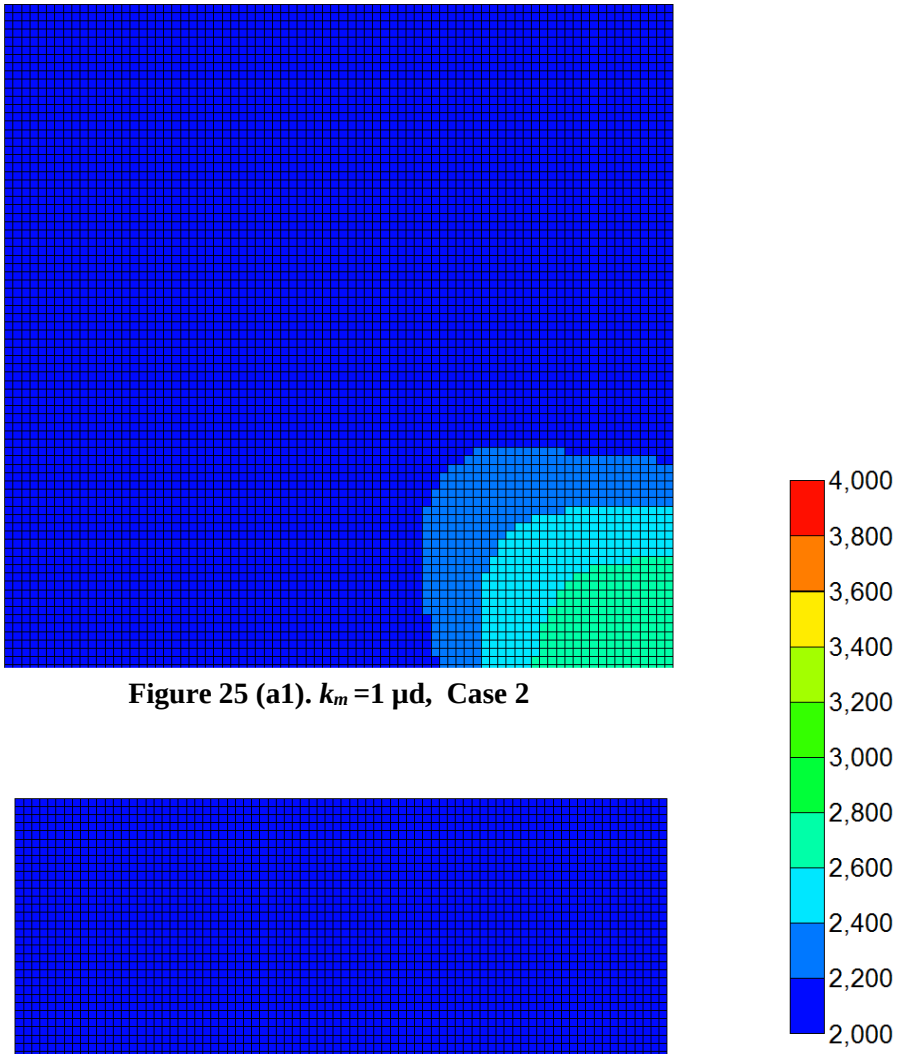

Figure 25 (a1). k_m =1 µd, Case 2

Figure 25 (a2). k_m =1 µd, Case 4

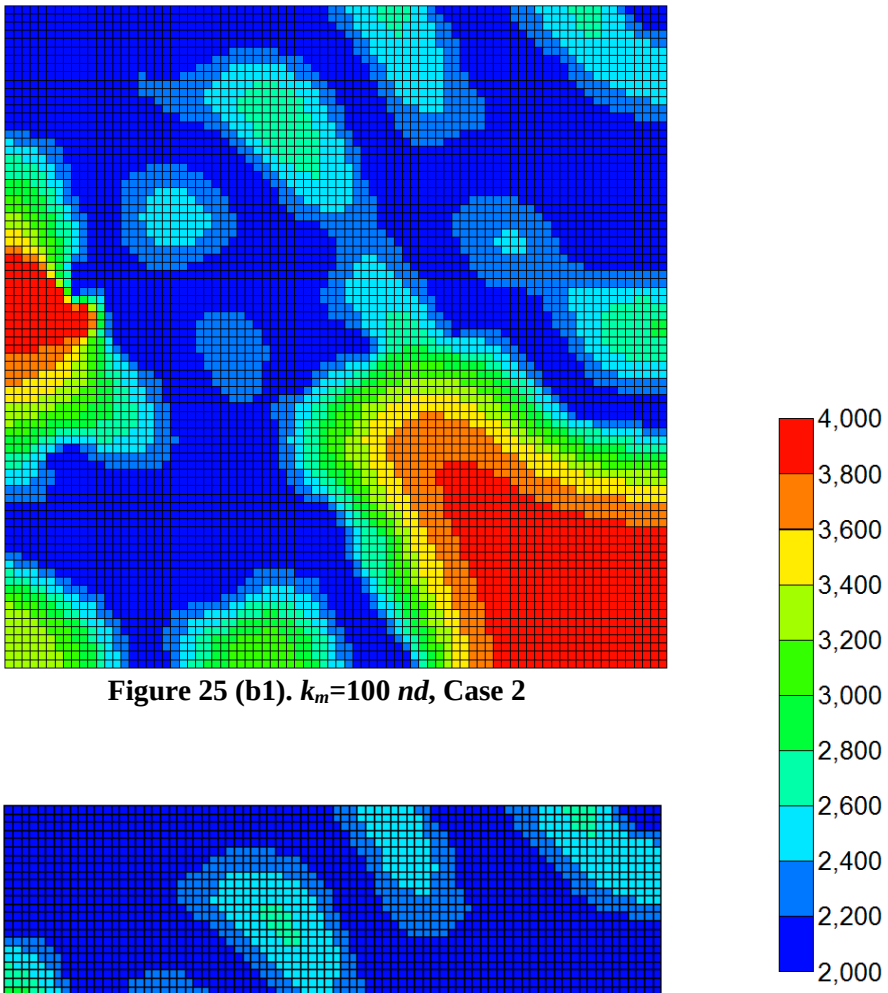

Figure 25 (b1). k_m**=100** ***nd*****, Case 2**

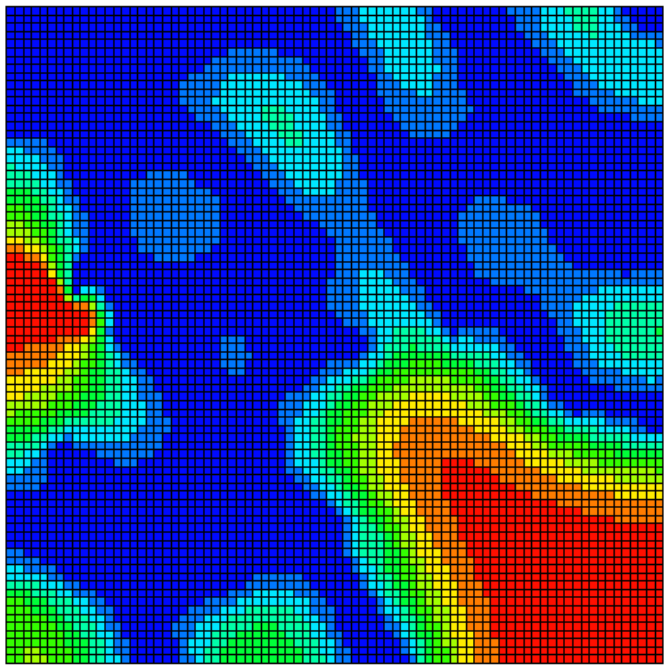

Figure 25 (b2). k_m**=100** ***nd*****, Case 4**

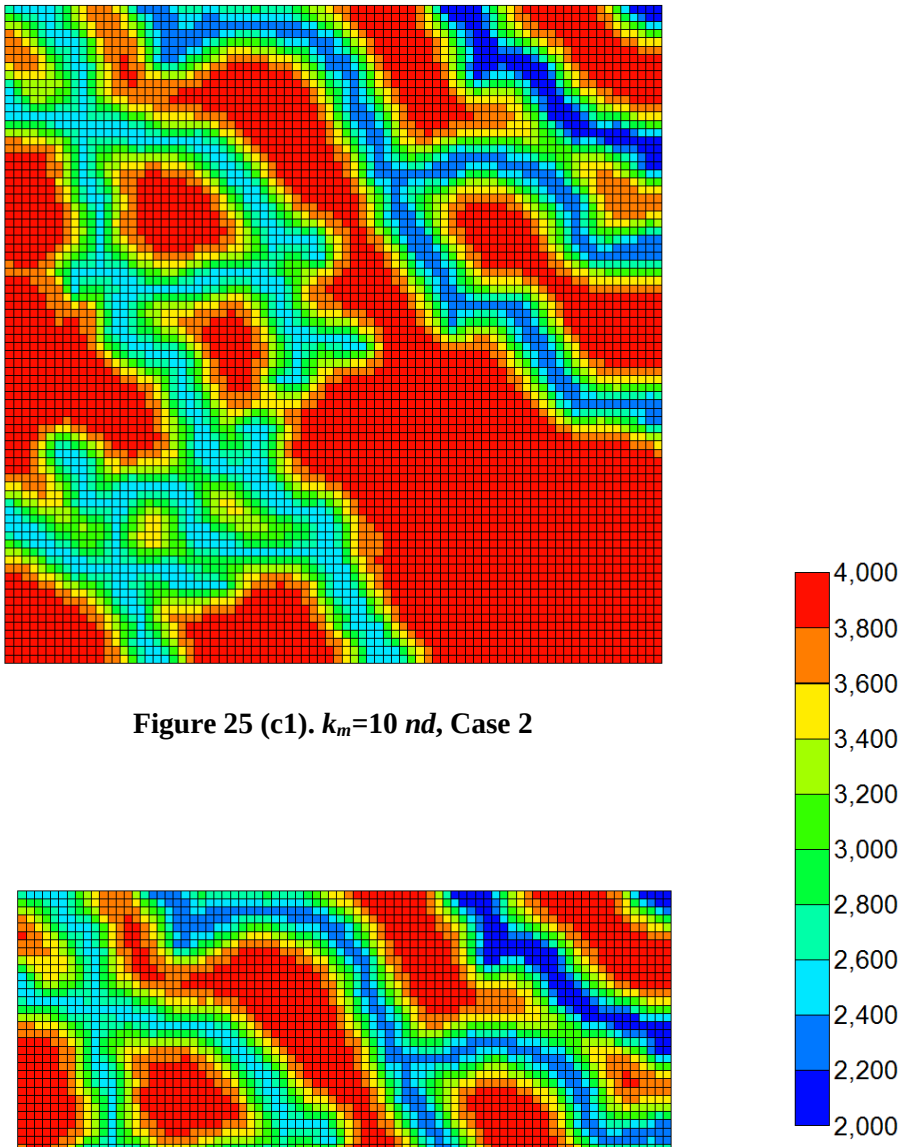

Figure 25 (c1). k_m**=10** ***nd*****, Case 2**

Figure 25 (c2). k_m**=10** ***nd*****, Case 4**

Figure 25. Pressure after 7 yr of production with 80 × 80 cells for case 2 and 4.

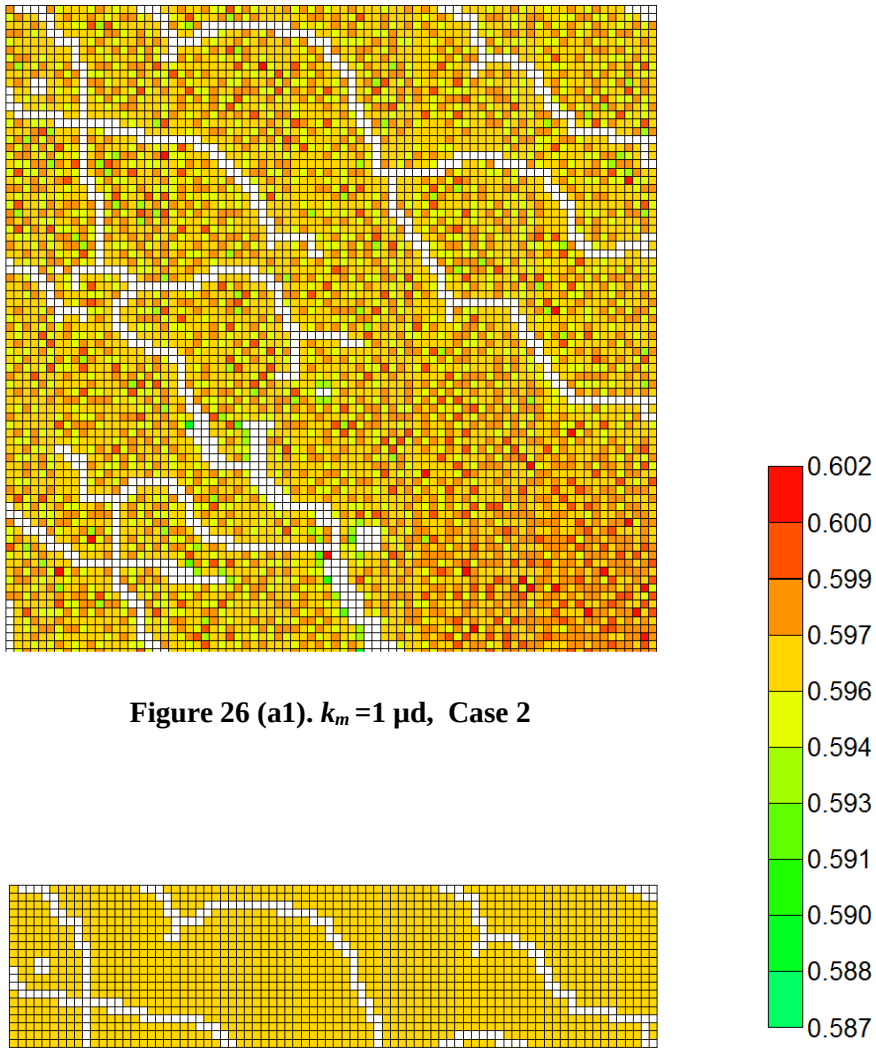

Figure 26 (a1). k_m **=1 µd, Case 2**

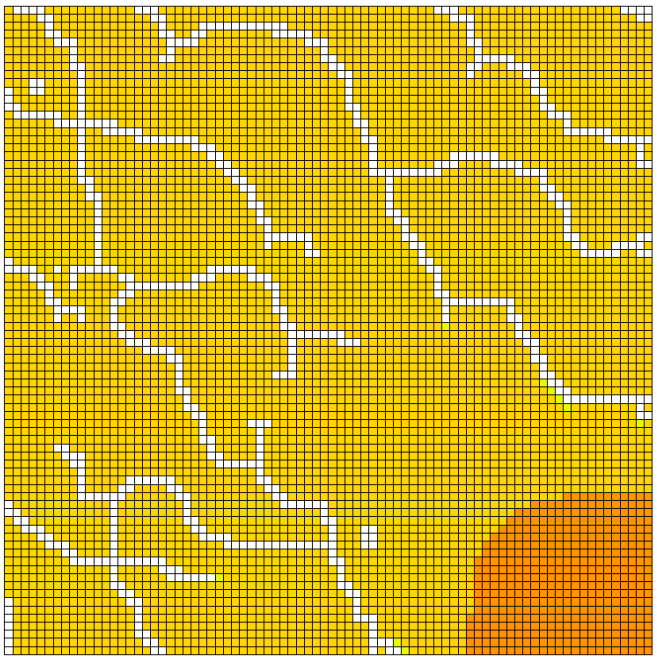

Figure 26 (a2). k_m **=1 µd, Case 4**

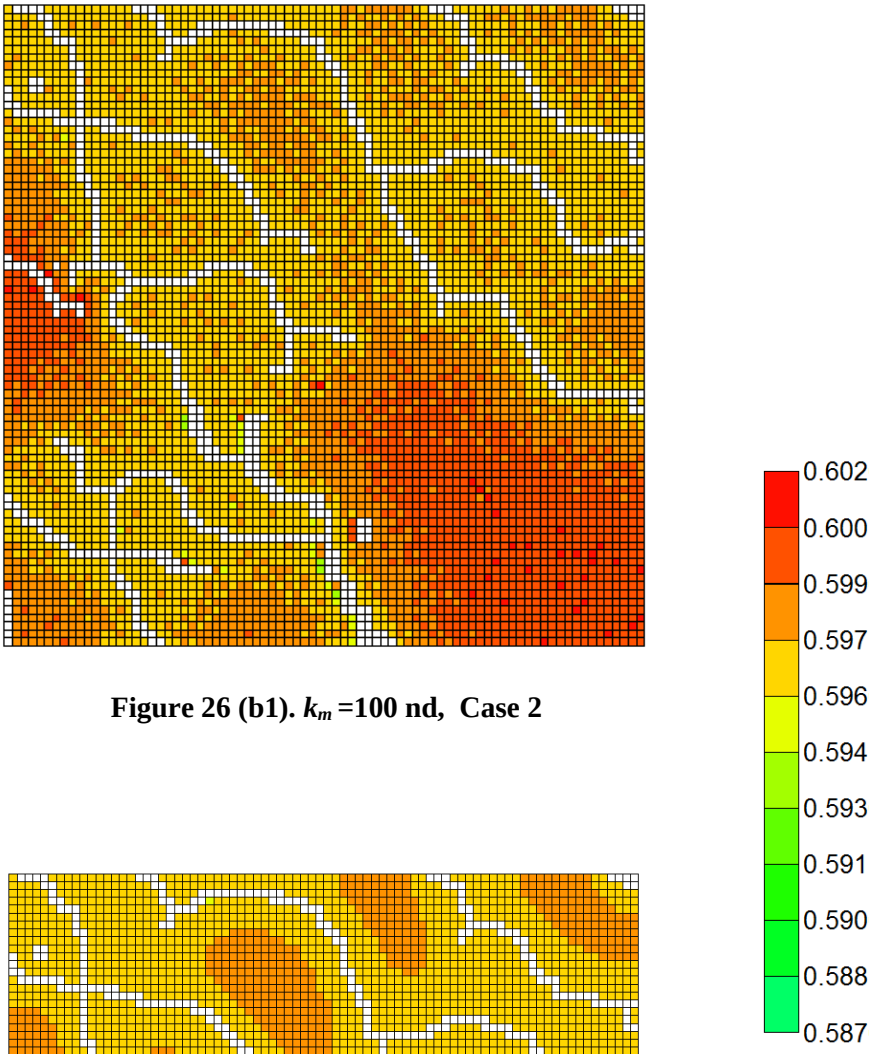

Figure 26 (b1). k_m **=100 nd, Case 2**

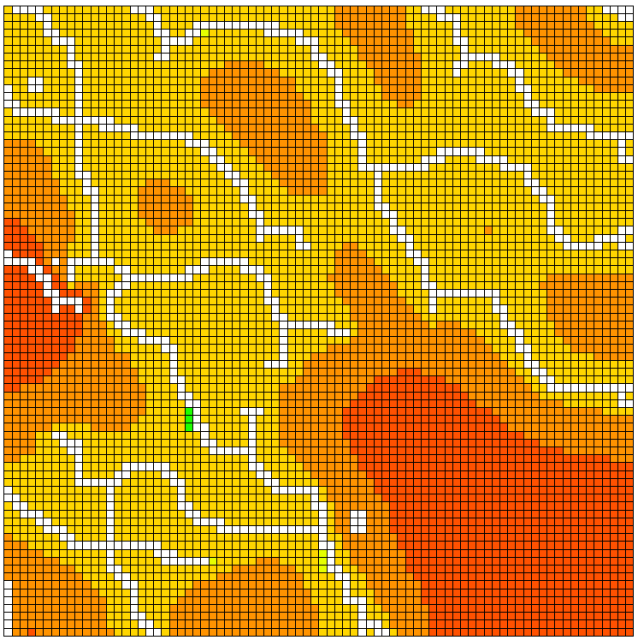

Figure 26 (b2). k_m **=100 nd, Case 4**

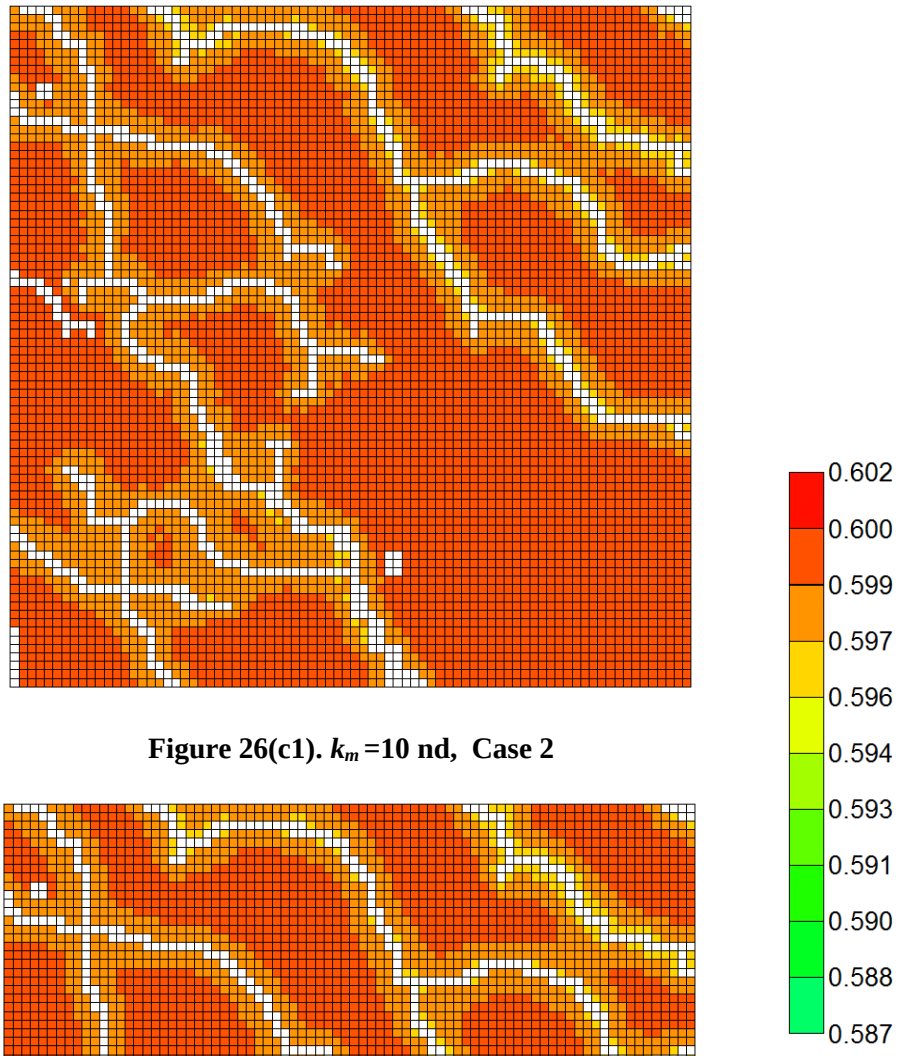

Figure 26(c1). k_m =10 nd, Case 2

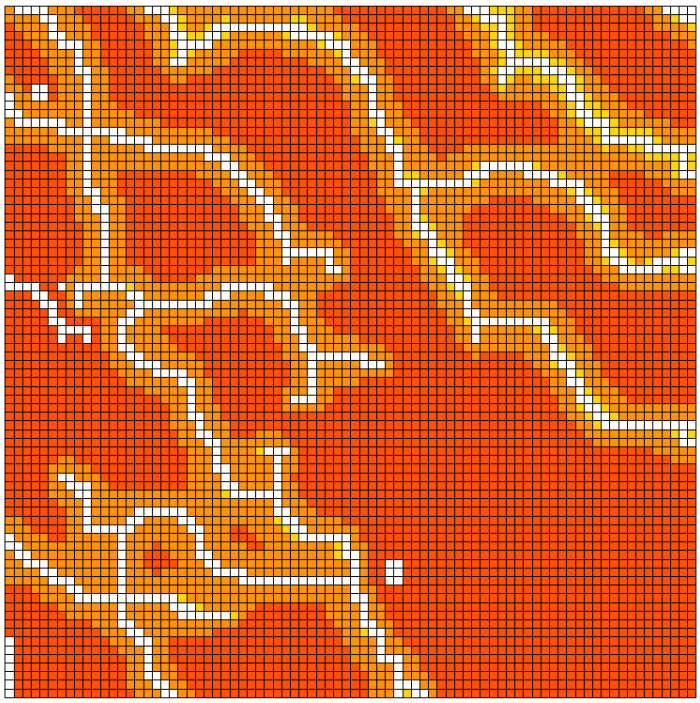

Figure 26 (c2). k_m =10 nd, Case 4

Figure 26. Saturations after 7 yr of production with 80 × 80 cells for case 2 and 4.

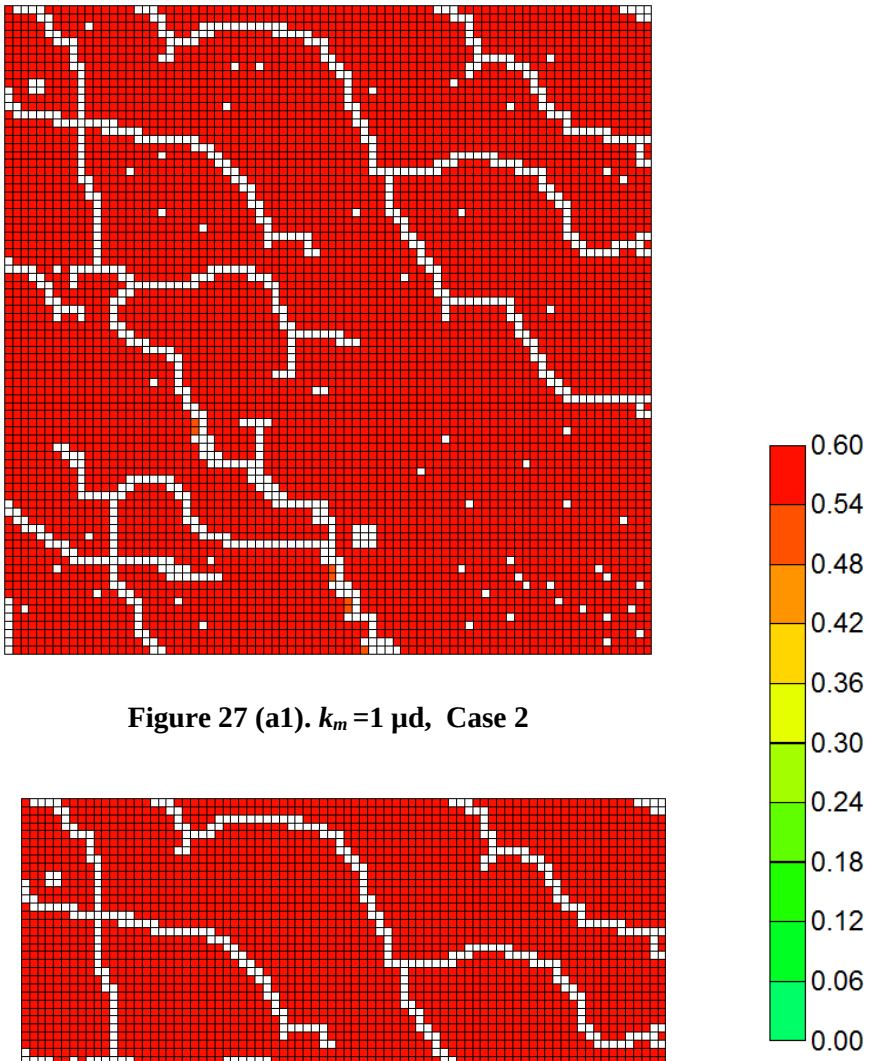

Figure 27 (a1). k_m **=1 μd, Case 2**

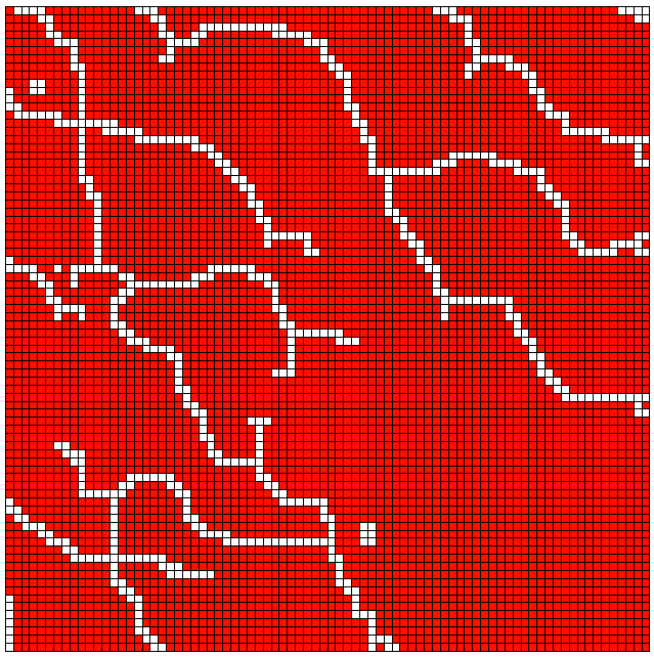

Figure 27 (a2). k_m **=1 μd, Case 4**

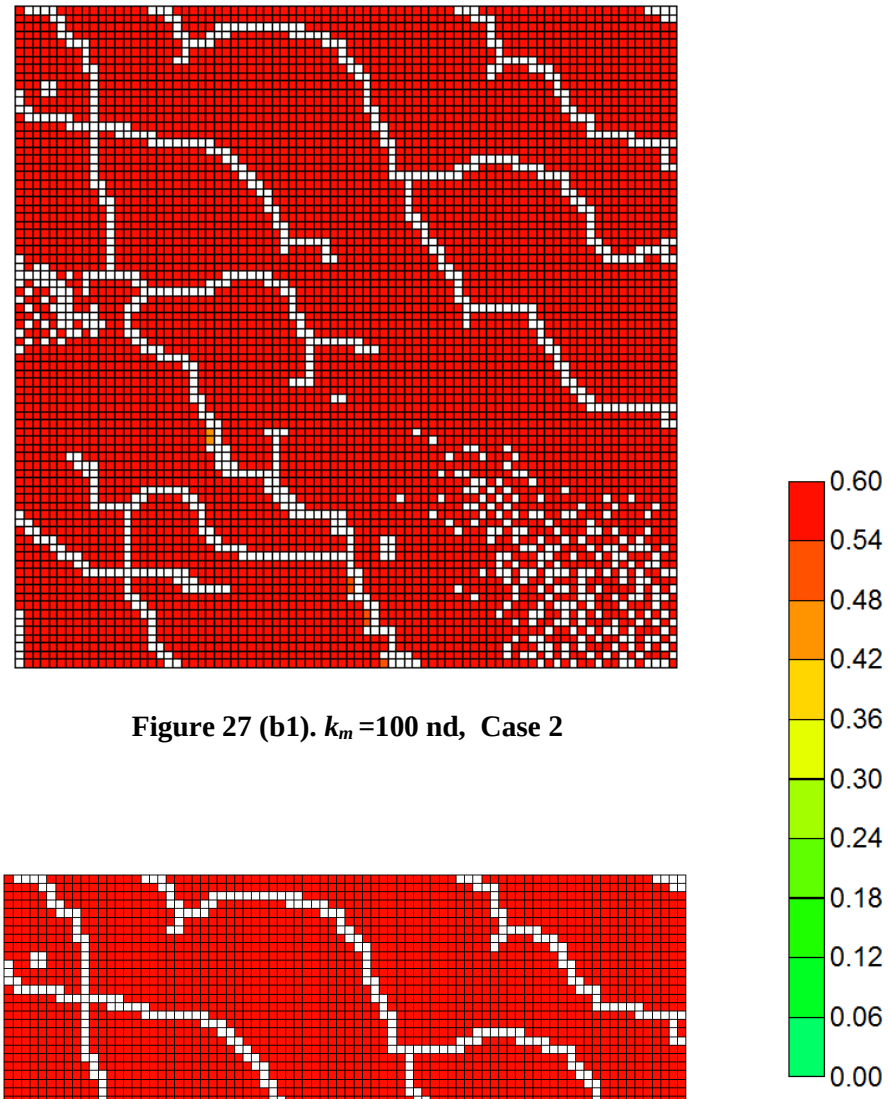

Figure 27 (b1). k_m **=100 nd, Case 2**

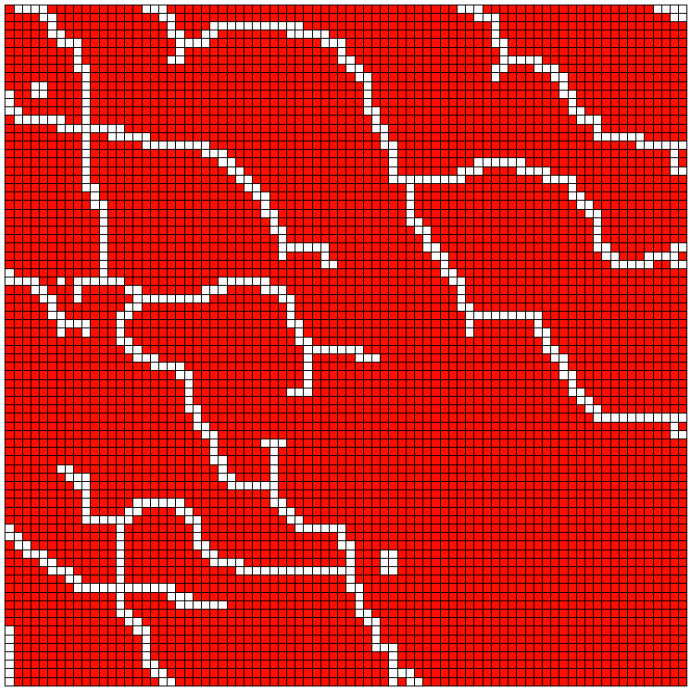

Figure 27 (b2). k_m **=100 nd, Case 4**

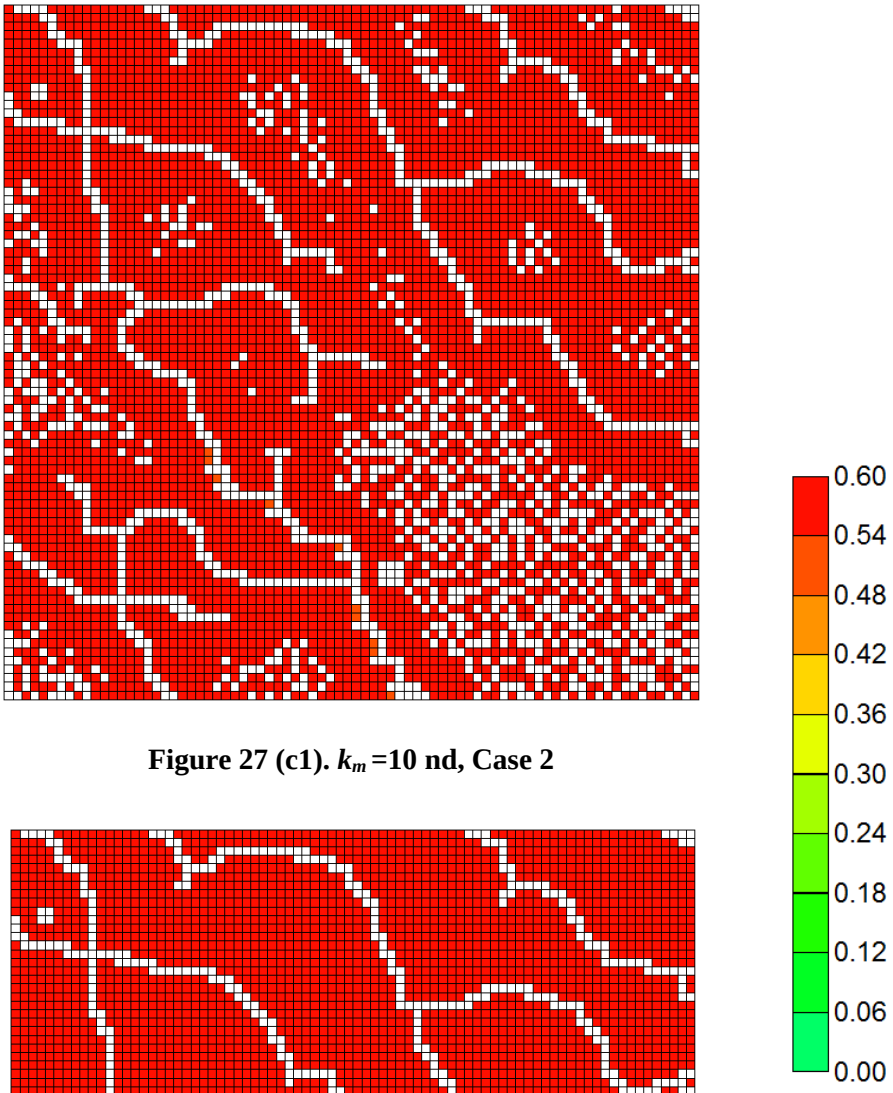

Figure 27 (c1). k_m =10 nd, Case 2

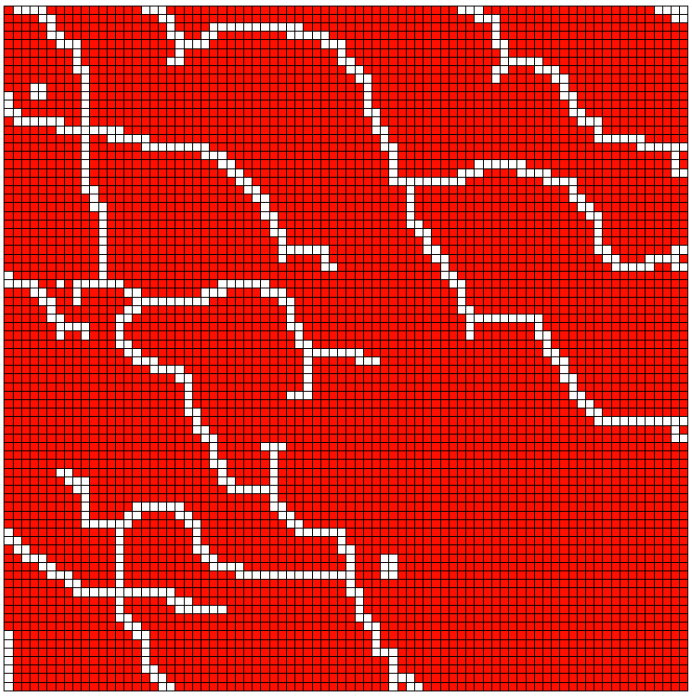

Figure 27 (c2). k_m =10 nd, Case 4

Figure 27. Saturations after 7 yr for case 2 and case 4 with another scale.

Case 3 vs case 5

Similarly, the pressure and oil saturation profiles after 7 years of production are showing below for case 3 and case 5 from **Figure 28** to **Figure 30**.

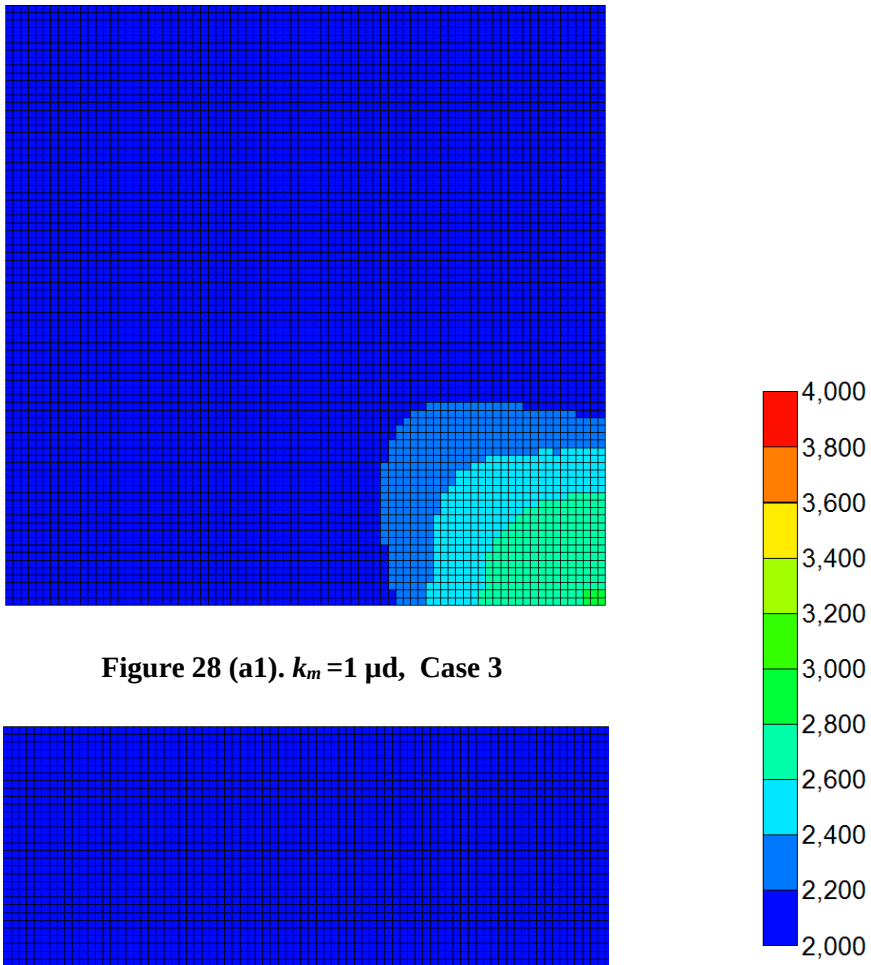

Figure 28 (a1). k_m **=1 µd, Case 3**

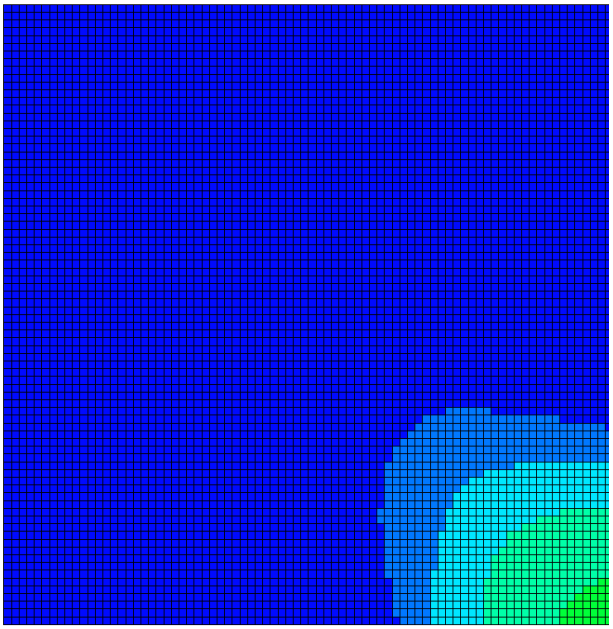

Figure 28 (a2). k_m **=1 µd, Case 5**

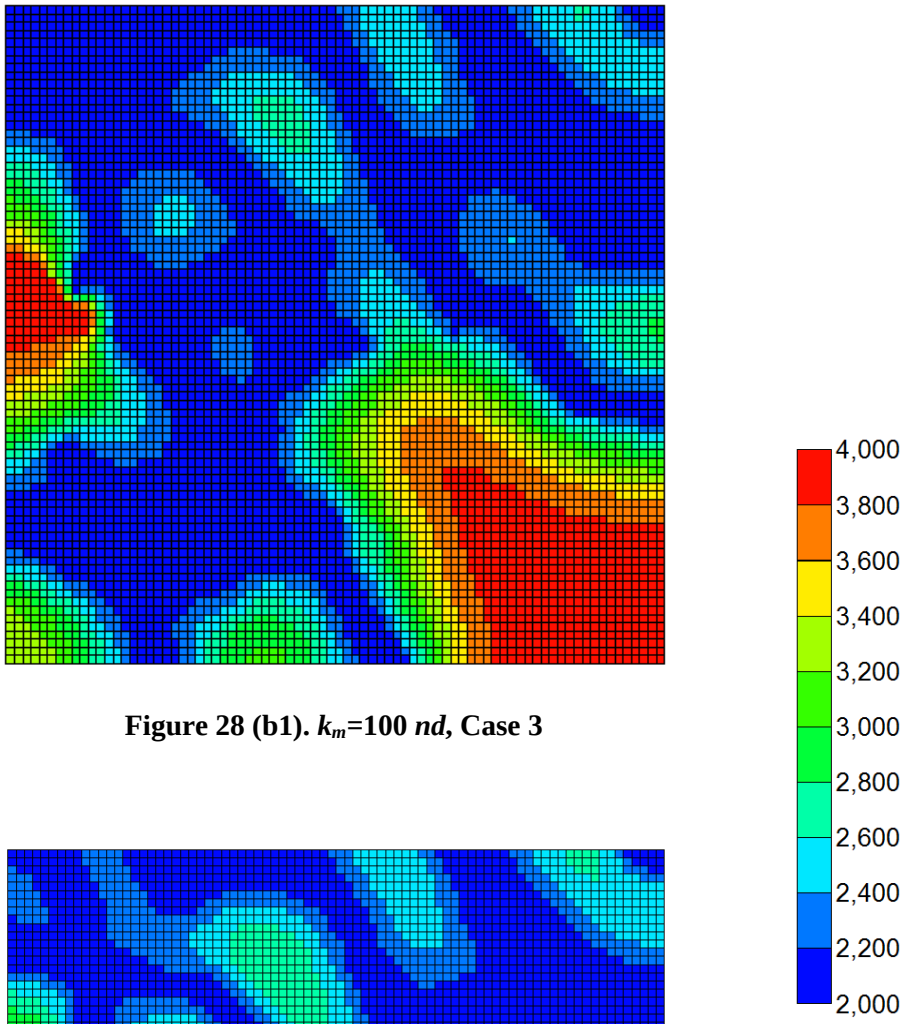

Figure 28 (b1). k_m**=100** ***nd*****, Case 3**

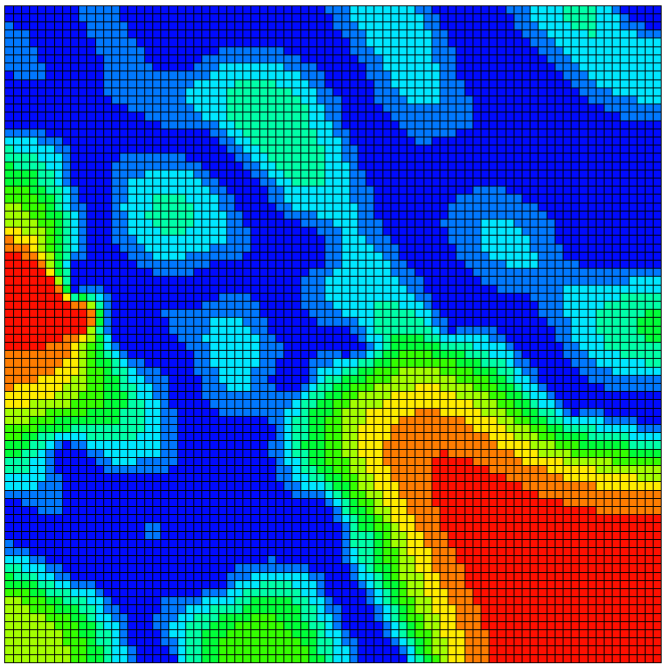

Figure 28(b1). k_m**=100** ***nd*****, Case 5**

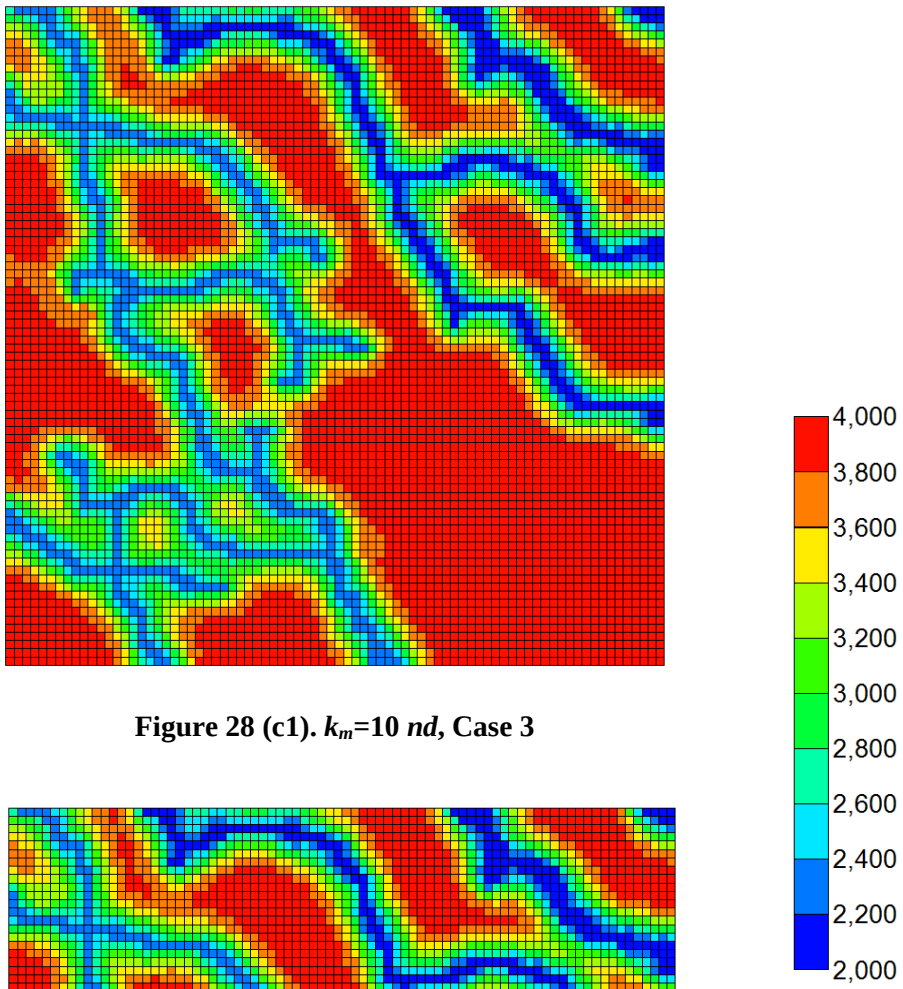

Figure 28 (c1). k_m=10 *nd*, Case 3

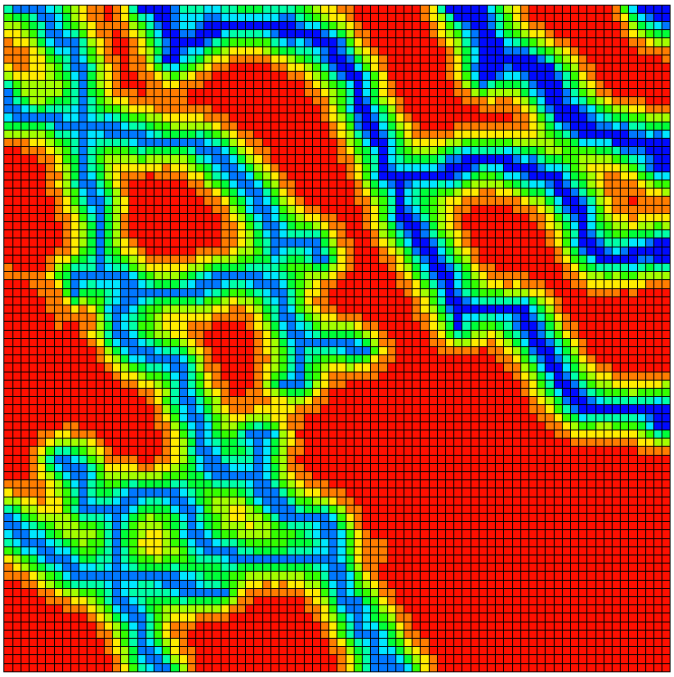

Figure 28 (c2). k_m=10 *nd*, Case 5

Figure 28. Pressures after 7 yr of production with 80 × 80 cells for case 3 and 5.

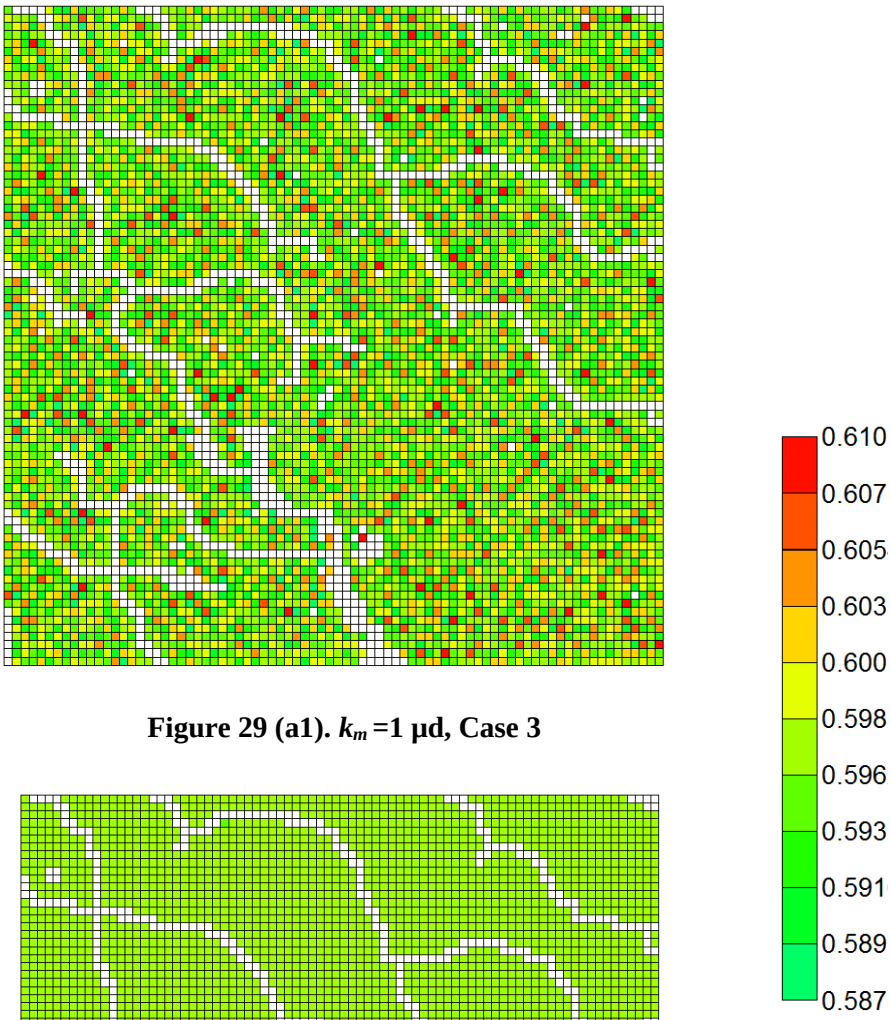

Figure 29 (a1). k_m **=1 µd, Case 3**

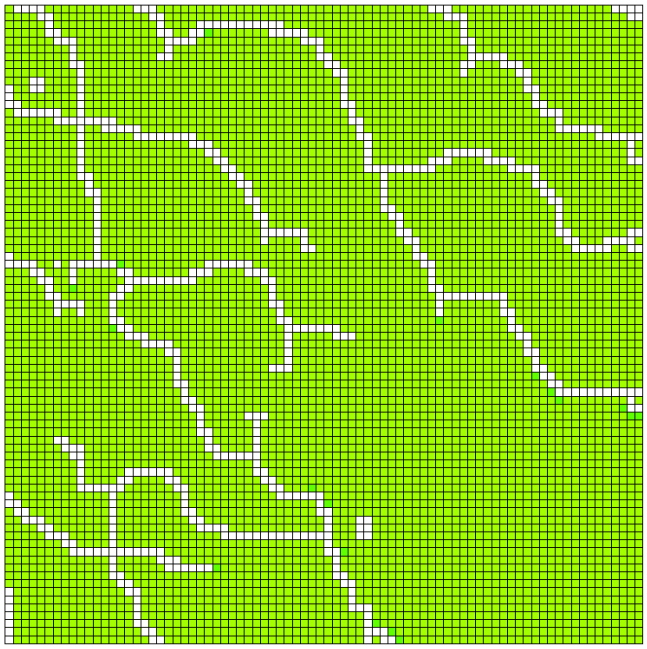

Figure 29 (a2). k_m **=1 µd, Case 5**

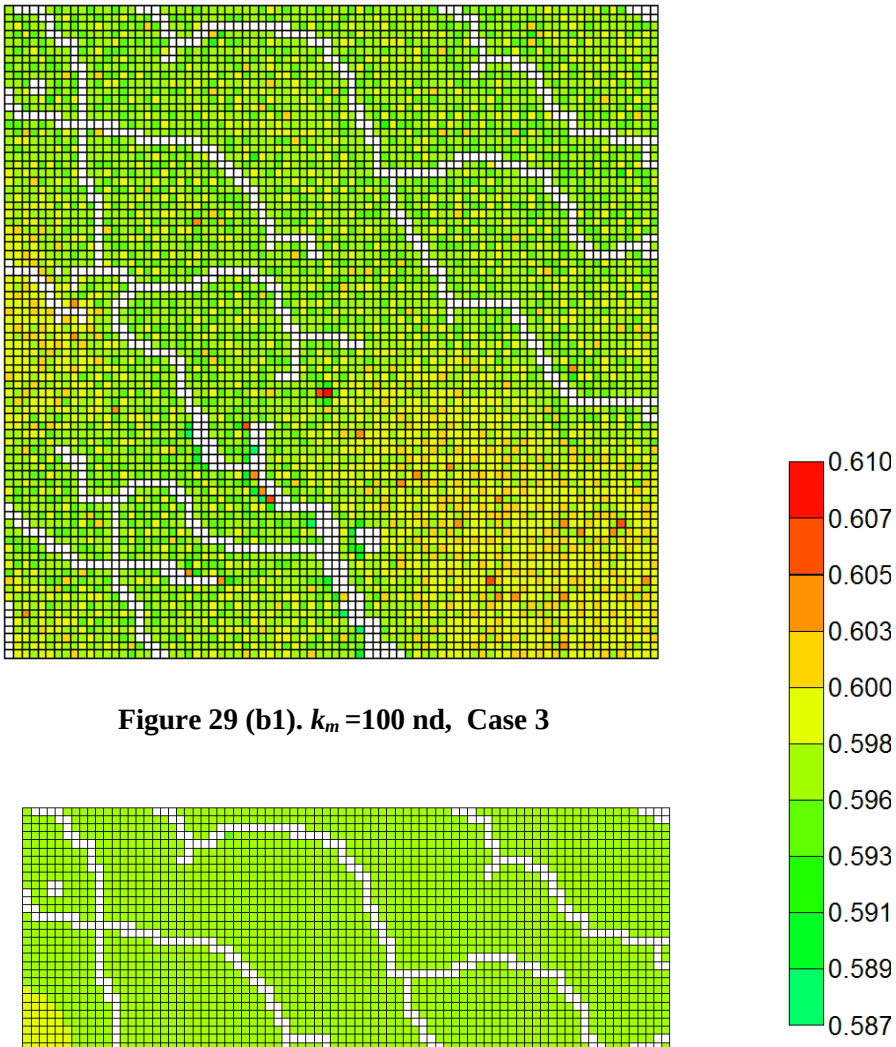

Figure 29 (b1). k_m =100 nd, Case 3

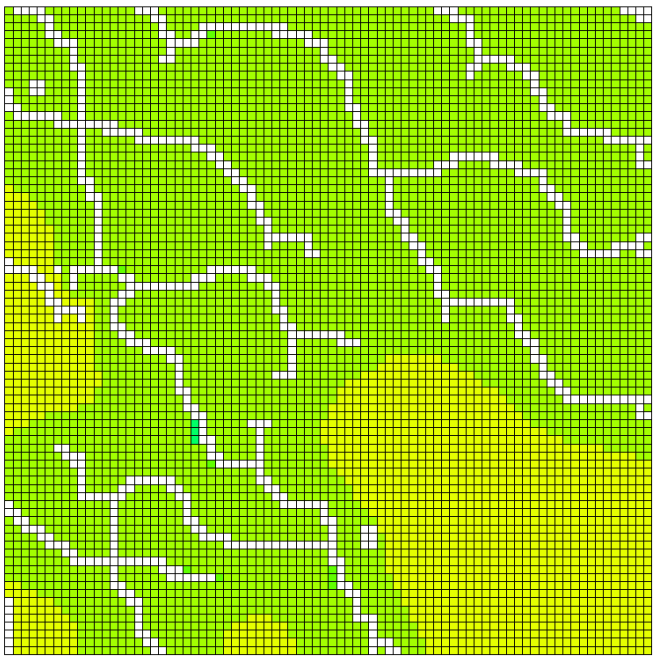

Figure 29 (b2). k_m =100 nd, Case 5

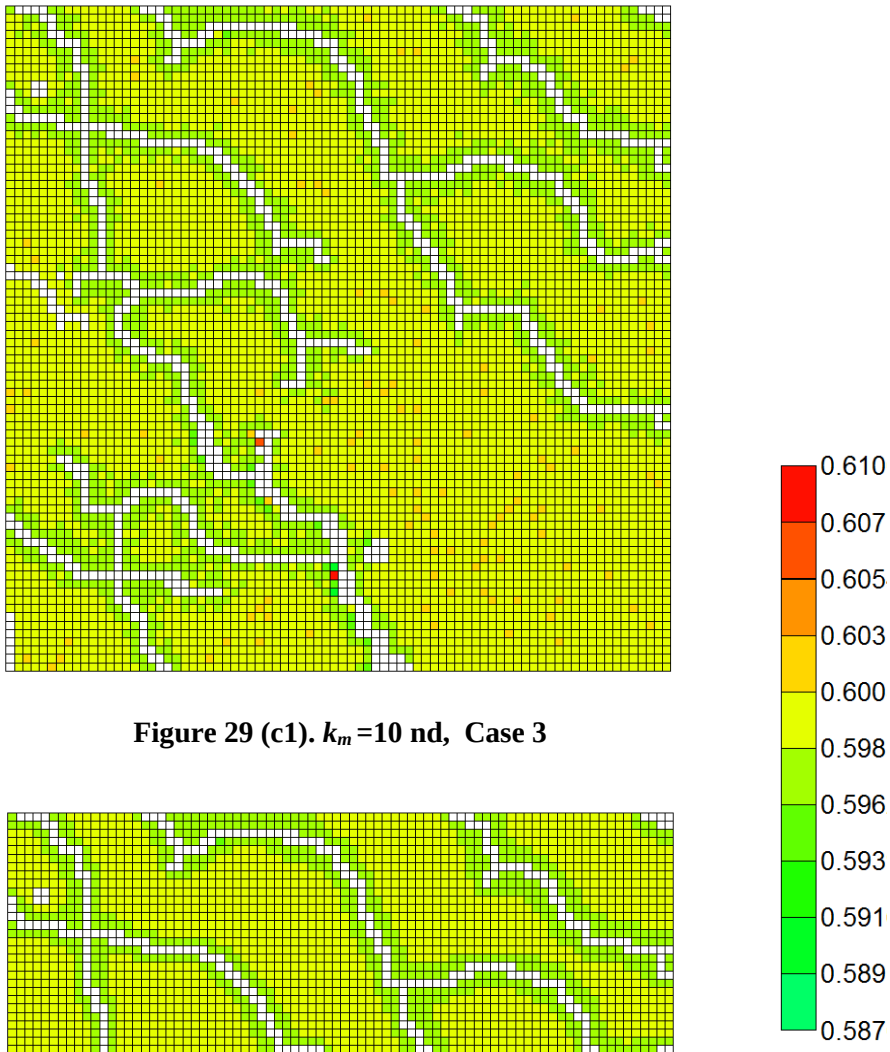

Figure 29 (c1). k_m =10 nd, Case 3

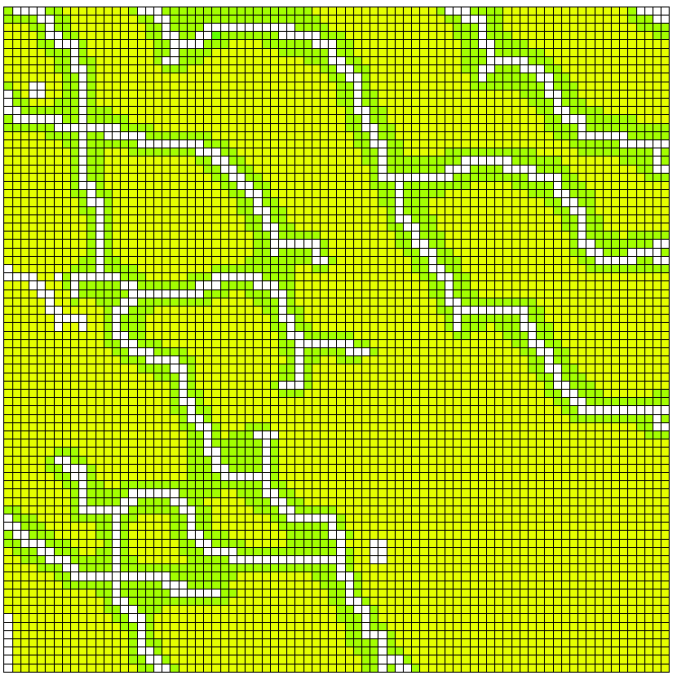

Figure 29 (c2). k_m =10 nd, Case 5

Figure 29. Saturations after 7 yr of production with 80 × 80 cells for case 3 and 5.

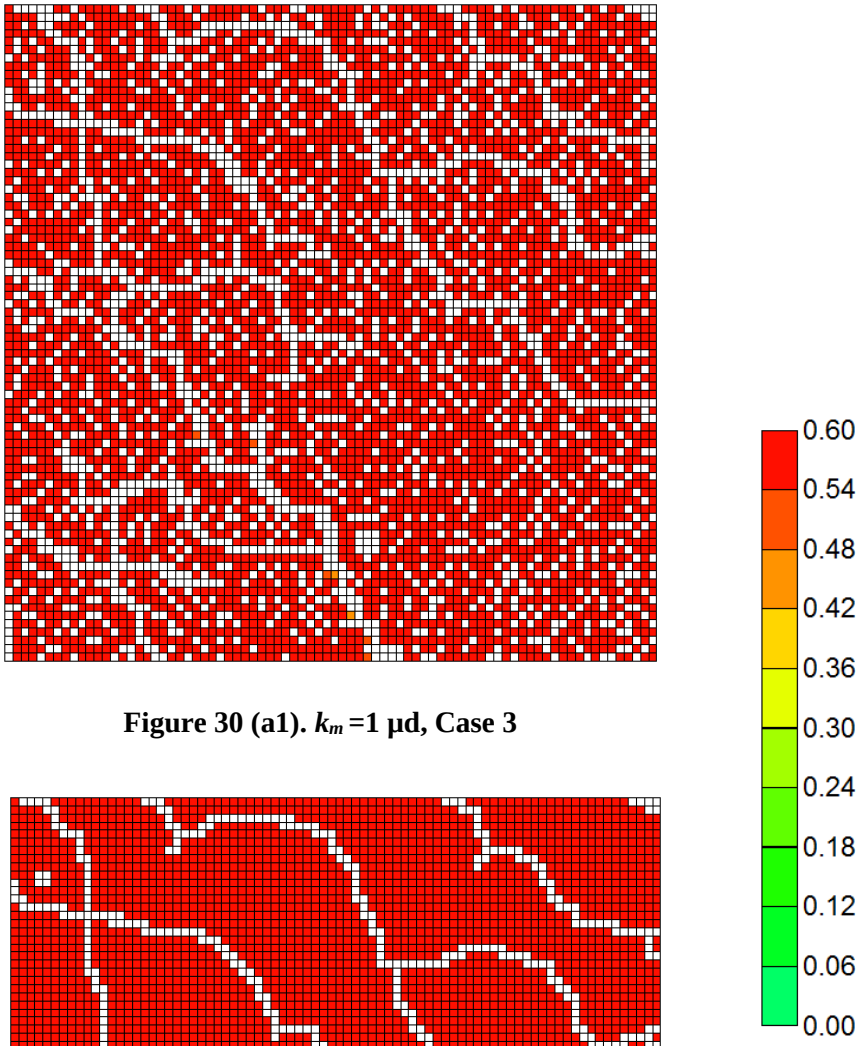

Figure 30 (a1). k_m =1 μd, Case 3

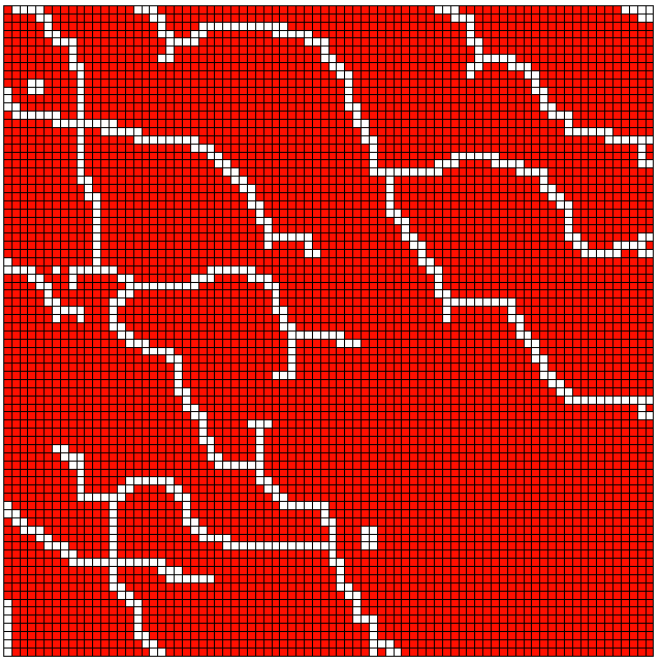

Figure 30 (a2). k_m =1 μd, Case 5

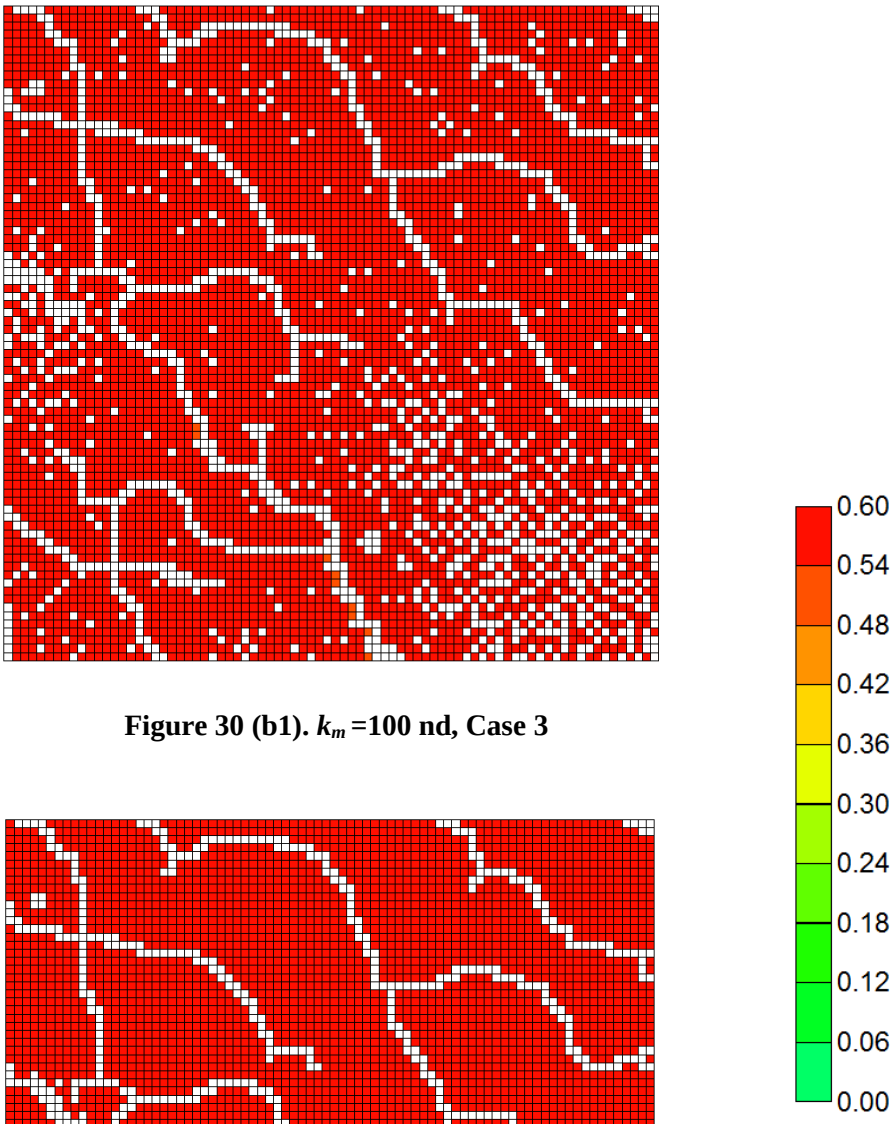

Figure 30 (b1). k_m =100 nd, Case 3

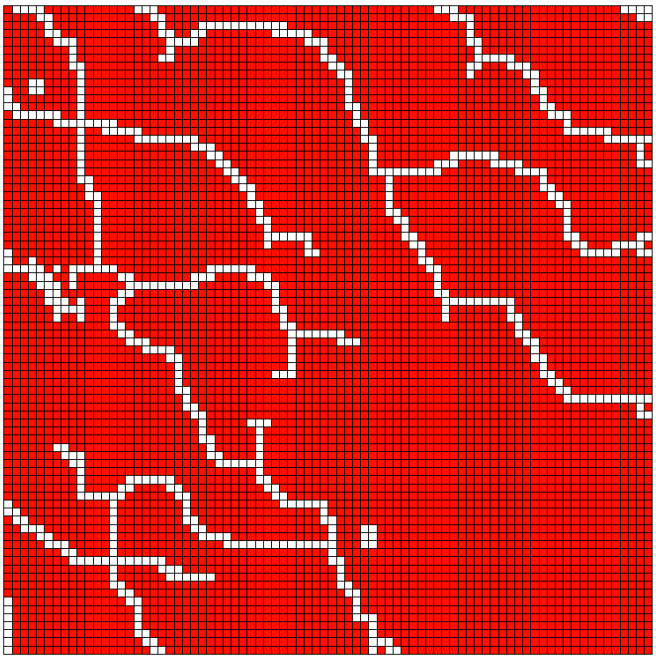

Figure 30 (b2). k_m =100 nd, Case 5

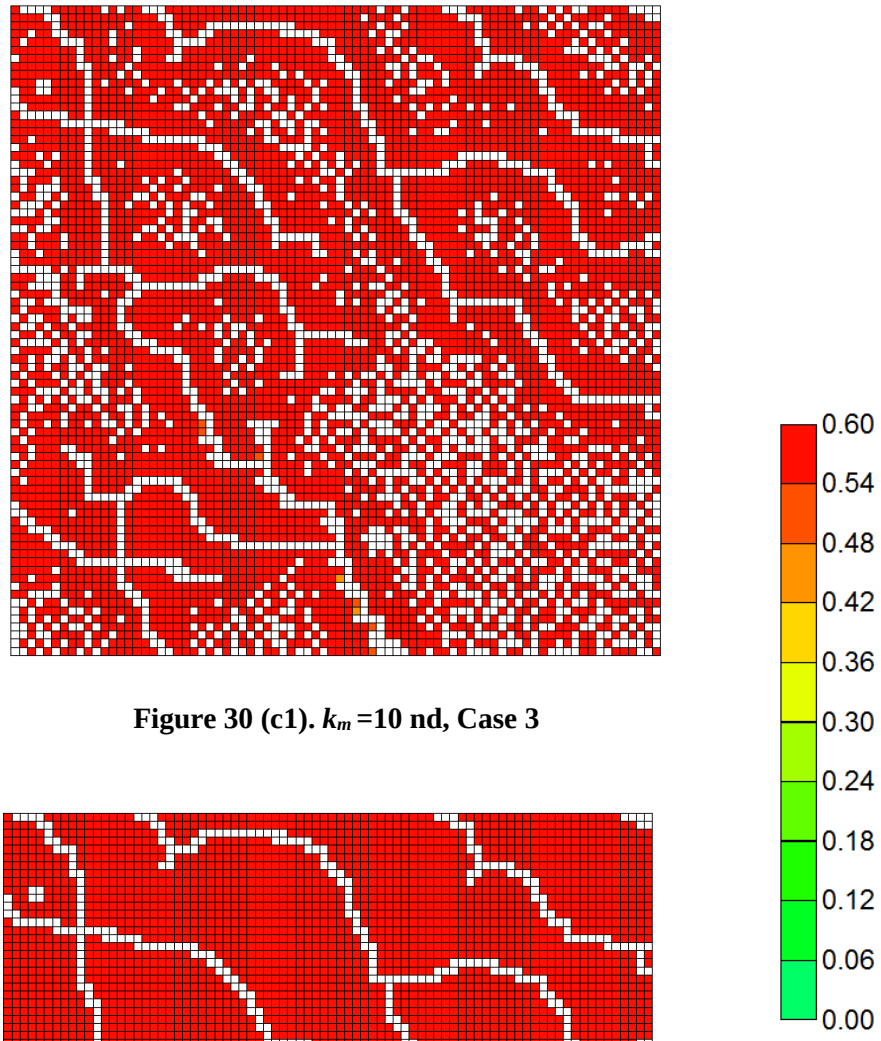

Figure 30 (c1). k_m =10 nd, Case 3

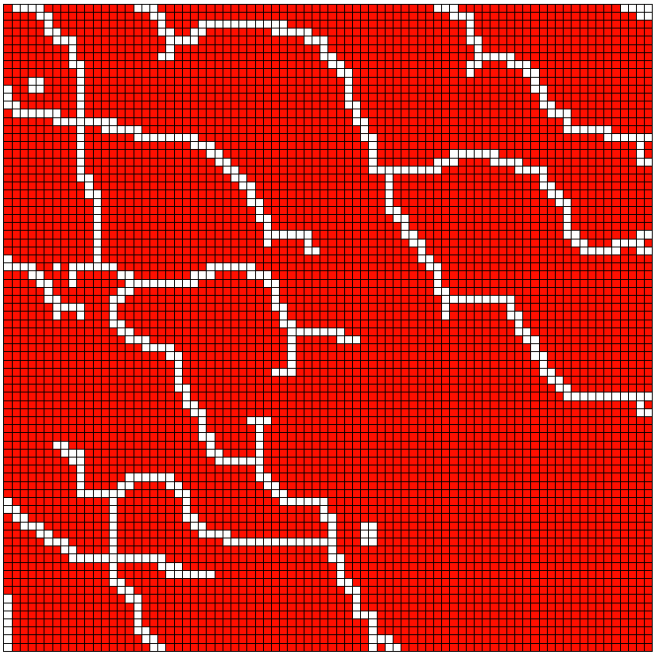

Figure 30 (c2). k_m =10 nd, Case 5

Figure 30. Saturations after 7 yr for case 3 and case 5 with another scale.

Chapter 6: Conclusions

The induced fractures in shale formations often form a complex pattern due to the formation heterogeneity and stress anisotropy. They are often multiple intersecting curved (complex) fractures. The increase in the contact area achieved by hydraulic fracturing is the main reason for the economic production from these formations. Thus, a better characterization of the complex fracture could help us understand hydrocarbon production more accurately. Thus, we used the fracture cell model to capture the complex fractures while accounting for the formation heterogeneity. The conducted study included heterogeneity in porosity, permeability, and the capillary pressure.

We accounted for the heterogeneity of the petrophysical properties using the fracture cell model. Five scenarios were included to present different level heterogeneities, and for each scenario, at least 50 realizations were presented. The matrix permeability was taken to be realistic for shale formations (k_m =1 μd, 100 nd, 10 nd).

Our study showed that the capillary pressure heterogeneity plays a dominant role, compared to the effects of permeability and porosity heterogeneity, for the cumulative production. This conclusion is true for shale formations where the matrix permeability is usually smaller than 1 μd. Using a representative capillary pressure based on *J* function reduces the uncertainty of the results, and the difference between the minimum and maximum cumulative productions becomes less significant.

A better understanding of the reduced model is important when petroleum engineers provide an estimate for the cumulative production. The accuracy of the reduced model was improved when the capillary heterogeneity is included based on the *J* function. The capillary heterogeneity implemented using *J* function accounts for the local capillary trapping. The capillary heterogeneity also results in a ramified fluid front. The conducted study has major implications for building a more realistic reservoir model for shale formations as it quantifies the importance of capillary heterogeneity on the cumulative production. It also provides a convenient tool, Fracture-Cell model, that can be easily incorporated in a commercial software.

We checked the accuracy of the reduced model with complex fractures by comparing the results for different number of cells. The accuracy of the reduced model decreases as much as 50% for homogeneous model when we decrease the number of cell by a factor of 6.4. This effect becomes much less significant when we account for the heterogeneity of the formation. The difference between the results of the reduced and the refined models becomes negligible when we scale the capillary pressure of the reservoir using *J* function. We also have to pay attention that, when the reduced model fracture pattern is no longer representative to the refined model, the EUR sensitivity to cell sizes become less convincing. Therefore, the corresponding reservoir setting, such as fluid saturations for the fracture cells has to be modified or upscaled. The implement of the *J* function results in a less scattered range of EUR realizations in ultralow permeability cases, meaning *J* function utilization strengthen the cumulative production prediction capability in the representative reduced model. For the reduced models in k_m =1 μd and k_m =100 nd

heterogeneous formations scenarios, the average cumulative productions follow the production decreasing trend: case 5, case 4, case 3, case 2.

Our model has applications for predicting the ultimate recovery of a shale formation with complex fractures by clarifying the importance of the formation heterogeneity. It also reveals the accuracy of the reduced models for shales and the importance of the matrix-fracture permeability interactions in the fracture adjacent cells. For sake of the broader application, the corresponding permeability-porosity correlations can be made.

Nomenclature

$a =$ fracture passed dimension perpendicular to pressure gradient

$A =$ cross section area

$a/h =$ span ratio

$b =$ fracture passed dimension parallel to the pressure gradient

$b/h =$ penetration ratio

$B_l =$ fluid formation volume factor

$e_0 =$ Corey relative permeability model exponent for non-wetting phase

$e_w =$ Corey relative permeability model exponent for wetting phase

$h =$ reservoir cell size

$J =$ *J* function

$k =$ absolute permeability

$k_{FF} =$ effective permeability of two neighbor fracture cells

$k_m =$ matrix permeability

$k_{MF} =$ effective permeability counting interactions between fracture cell and the adjacent matrix cells

$k_{MM} =$ effective permeability of two neighbor matrix cells.

$k'_{MF} =$ modified permeability which is assigned to fracture adjacent cell

$k_{rw} =$ wetting phase relative permeability

$k^o_{rw} =$ end point wetting phase relative permeability

$k_{ro} =$ non-wetting phase relative permeability

$k^o_{ro} =$ end point non-wetting phase relative permeability

$k_S =$ permeability of surrounding region

m= empirical parameter in Van Genuchten model

l_C/l_f = length ratio of representative path length and curved fracture length

p_c = capillary pressure

p_{nw} = non-wetting phase pressure

p_w = wetting phase pressure

μ_l = fluid viscosity

$\bar{S}$ = normalized wetting phase saturation

S_w = wetting phase saturation

S_{wr} = residual wetting phase saturation

S_{or} = residual non-wetting phase saturation

T = transmissibility

w = fracture cell width

α = empirical parameter in Van Genuchten model

β_c = unit conversion constant

ϕ = porosity

σ =surface tension

θ =contact angle

Δx = cell size in x direction

References

Alfi, Masoud, Bicheng Yan, Yang Cao, Cheng An, John E. Killougha, and Maria A. Barrufet. 2015. "Microscale porosity models as powerful tools to analyze hydrocarbon production mechanisms in liquid shale." *Journal of Natural Gas Science and Engineering* 26: 1495-1505. doi:http://dx.doi.org/10.1016/j.jngse.2015.08.002.

Al-Hinai, Omar, Gurpreet Singh, Gergina Pencheva, Tameem Almani, and Mary F. Wheeler. 2013. "Modeling Multiphase Flow with Nonplanar Fractures." *Reservoir Simulation Syposium.* Woodlands: Society of Petroleum Engineers. doi:http://dx.doi.org/10.2118/163605-MS.

Ambrose, Ray J., Robert C. Hartman, Mery Diaz-Campos, I. Yucel Akkutlu, and Carl H. Sondergeld. 2012. "Shale Gas-in- Place Caluculations Part I: New Pore-Scale Considerations." *SPE Journal* (Society of Petroleum Engineers) 17 (01). doi:http://dx.doi.org/10.2118/131772-PA.

Balogun, A., H. Kazemi, M. Al-Kobaisi, and B. Ramirez. 2007. "Verification and Proper Use of Water/ Oil Transfer Funcion for Dual-Porosity and Dual-Permeability Reservoirs." *Middle East Oil & Gas Show and Conference.* Bahrain, Kingdom of Bahrain: Society of Petroleum Engineers. doi:http://dx.doi.org/10.2118/104580-MS.

Barenblatt, G. I., Lu. P. Zheltov, and I.N. Kochina. 1960. "Basic Concepts in The Theory of Seepage of Homogeneous Liquids in Fissured Rocks." *Applied Mathematics and Mechanics* 24 (5): 1286-1303. doi:doi:10.1016/0021-8928(60)90107-6.

Blaskovish, F. T., G. M. Cain, Fernand Sonier, David Waldren, and S. J. Webb. 1983. "A Multicomponent Isothermal Systerm For Efficient Reservoir Simulation." *Middle East Oil Technical Conference.* Manama, Bahrain: Society of Petroleum Engineers. doi:http://dx.doi.org/10.2118/11480-MS.

Chen, Li, Qinjun Kang, Rajesh Pawar, Ya-Ling He, and Wen-Quan Tao. 2015. "Pore-scale prediction of transport properties in reconstructed nanostructures of organic matter in shales." *Fuel* 650-658. doi:http://dx.doi.org/10.1016/j.fuel.2015.06.022.

Civan, Faruk. 2010. "Effective Correlation of Apparent Gas Permeability in Tight Porous Media." *Transp Porous Med* 82 (2): 375-384. doi:10.1007/s11242-009-9432-z.

Civan, Faruk, Chandra S. Rai, and Carl H. Sondergeld. 2011. "Shale-gas permeability and diffusivity inferred by improved formulation of relevant retention and transport mechanisms." *Transp Porous Med* 86 (3): 925-944. doi:10.1007/s11242-010-9665-x.

Civan, Faruk, Deepak Devegowda, and Richard Sigal. 2013. "Critical Evaluation and Improvement of Methods for Determination of Matrix Permeability of Shale." *SPE Annual Technical Conference and Exhibition.* New Orleans: Society of Petroleum Engineers. doi:http://dx.doi.org/10.2118/166473-MS.

Corey, A.T. 1954. "The interrelation Between Gas and Oil Relative Permeabilities." (Producers Monthly) 38-41.

Daniels, J., G. Waters, J. LeCalvez, J. Lassek, and D. Bentley. 2007. "Contacting More of the Barnett Shale Through an Integration of Real-Time Microseismic Monitoring, Petrophysics and Hydaulic Fracture Design." *Annual Technical Conference and Exhibition.* Anaheim: Society of Petroleum Engineers. doi:http://dx.doi.org/10.2118/110562-MS.

Darabi, Hamed, Amin Ettehadtavakkol, Farzam Javadpour, and Kamy Sepehrnoori. 2012. "Gas Flow in Ultra-Tighr Shale Strata." *Journal of Fluid Mechanics* 641-658. doi:10.1017/jfm.2012.424.

Dean, R. H., and L. L. Lo. 1988. "Simulations of Narually Fractured Reservoir." *SPE Reservoir Engineering* (Society of Petroleum Engineers) 3 (02): 638-348. doi:http://dx.doi.org/10.2118/14110-PA.

Dewers, Thomas A., Jason Heath, Russ Ewy, and Luca Duranti. 2012. "Three-Dimensional Pore Networks and Transport Properties of a Shale Gas Formation Determined From Focused Ion Beam Serial Imaging." *Int. J. of Oil, Gas and Coal Technology* (Int. J. Oil, Gas and Coal Technology) 5: 229-248. doi:http://dx.doi.org/10.1504/IJOGCT.2012.046322.

Filho, Cavalcante, M. Shakiba J. S. A., A. Moinfar, and K. Sepehrnoori. 2015. "Implementation of a Preprocessor for Embedded Discrete Fracture Modeling in an IMPEC Compositional Reservoir Simulator." *SPE Reservoir Simulation Symposium.* Houston: Society of Petroleum Engineers. doi:http://dx.doi.org/10.2118/173289-MS.

Freeman, C. M., G.J. Moridis, G.E. Michael, and T.A. Blasingame. 2012. "Measurement, Modeling, and Diagnostics of Flowing Gas Composition Changes in Shale Gas Wells." *Latin American and Caribbean Petroleum Engineering Conference.* Mexico City, Mexico: Society of Petroleum Engineer. doi:http://dx.doi.org/10.2118/153391-MS.

Ganjdanesh, Reza, Mohsen Rezaveisi, Gary A. Pope, and Kamy Sepehrnoori. 2016. "Treatment of Condensate and Water Blocks in Hydraulic-Fractured Shale-Gas/Condensate Reservoirs." *SPE Journal* (Society of Petroleum Engineers) 21 (02): 665-674. doi:http://dx.doi.org/10.2118/175145-PA.

Geertsma, J., and F. De Klerk. 1969. "A Rapid Method of Predicting Width and Extent of Hydraulically Induced Fractures." *Journal of Petroleum Technology* (Society

of Petroleum Engineers) 21 (12): 1571-1581. doi:http://dx.doi.org/10.2118/2458-PA.

Genuchten, van. 1980. "A Closed Form Equation for Predicting the Hydraulic Conductivity of Unsaturated Soils." *Soil Science Society of America Journal 44 (5)* (Soil Socience Society of America Journal) 892-898. doi:10.2136/sssaj1980.03615995004400050002x.

Hartman, Robert C., Ray J. Ambrose, I. Yucel Akkutlu, and C.R. Clarkson. 2011. "Shale Gas-in-Place Calculations Part II -- Multi-component Gas Adsorption." *Unconventional Gas Conference.* Woodlands: Society of Petroleum Engineers. doi:http://dx.doi.org/10.2118/144097-MS.

Heller, Rob, John Vermylen, and Mark Zoback. 2014. "Experimental investigation of matrix permeability of gas shales." *AAPG Bulletin* 975-995. doi:DOI: 10.1306/09231313023.

Hoteit, Hussein, and Abbas Firoozabadi. 2008. "An Efficient Numerical Model for Incompressible Two-Phase Flow in Fractured Media." *Adcances in Water Resources* 31 (6): 891-905. doi:http://dx.doi.org/10.1016/j.advwatres.2008.02.004.

Javadpour, F., D. Fisher, and M. Unsworth. 2007. "Nanoscale Gas Flow in Shale Gas Sediments." *Journal of Canadian Petroleum Technology* 46 (10). doi:http://dx.doi.org/10.2118/07-10-06.

Kazemi, H., Jr. L. S. Merrill, K. L. Porterfield, and P.R. Zeman. 1976. "Numerical Simulation of Water-Oil Flow in Narually Fractured Reservoir." *Society of Petroleum Engineers Journal* (Society of Petroleum Engineers) 16 (06): 317-326. doi:http://dx.doi.org/10.2118/5719-PA.

Latham, John-Paul, Jiansheng Xiang, Mandefro Beleyneh, Hamidreza M. Nick, Chin-Fu Tsang, and Martin J. Blunt. 2012. "Modelling Stress-Dependent Permebility in Fractured Rock Including Effects of Propagating and Bending Fractures." *International Journal of Rock Mechanics & Mining Sciences* 57: 100-112. doi:http://dx.doi.org/10.1016/j.ijrmms.2012.08.002.

Leverett, M. C. 1941. "Capillary Behavior in Porous Solids." *Transactions of the AIME* (Trans. of AIME) 152-169. doi:http://dx.doi.org/10.2118/941152-G.

Li, Liyong, and S. H. Lee. 2008. "Efficient Field-Scale Simulation of Black Oil in a Naturally Fractured Reservoir Through Discrete Fracture Networks and Homogenized Media." *SPE Reservoir Evaluation & Engineering* 750-758. doi:10.2118/103901-PA.

Lu, Huiyun, Ginevra Di Donato, and Martin J. Blunt. 2008. "General Transfer Functions for Multiphase Flow in Fractured Reservoirs." *SPE Journal* (Society

of Petroleum Engineers) 13 (03): 289-297. doi:http://dx.doi.org/10.2118/102542-PA.

Mathur, Ashish, Carl H. Sondergeld, and Chandra S. Rai. 2016. "Comparison of Steady-State and Transient Methods for Measuring Shale Permeability." *SPE Low Perm Symposium.* Denver: Society of Petroleum Engineers. doi:http://dx.doi.org/10.2118/180259-MS.

Moinfar, Ali, Abdoljalil Varavei, Kamy Sepehrnoori, and Russell T. Johns. 2013. "Development of a Coupled Dual Continuum and Discrete Fracture Model for the Simulation of Unconventional Reseroivrs." *Reservoir Simulation Symposium.* Woodlands: Society of Petroleum Engineers. doi:http://dx.doi.org/10.2118/163647-MS.

Nojabaei, Bahareh, Russell T. Johns, and Lifu Chu. 2013. "Effect of Capillary Pressure on Phase Behavior in Tight Rocks and Shales." *Reservoir Evaluation & Engineering* 16 (03): 281 - 289. doi:http://dx.doi.org/10.2118/159258-PA.

Nordgren, R.P. 1972. "Propagation of a Vertical Hydraulic Fracture." *Society of Petroleum Engineers Journal* (Society of Petroleum Engineers) 12 (04): 306-314. doi:http://dx.doi.org/10.2118/3009-PA.

Olorode, O. M., C. M. Freeman, G. J. Moridis, and T.A. Blasingame. 2013. "High-Resolution Numerical Modeling of Complex and Irregular Fracture Patterns in Shale- Gas Reservoirs and Tight Gas Reservoirs." *SPE Reservoir Evaluation & Engineering* (SPE Reservoir Evaluation & Engineering) 16 (04): 443-455. doi:http://dx.doi.org/10.2118/152482-PA.

Penny, G.S., J.T. Pursley, and T.D. Clawson. 2006. "Field Study of Completion Fluids to Enhance Gas Production in Barnett Shale." *Gas Technology Symposium.* Calgary, Canada: Society of Petroleum Engineers. doi:http://dx.doi.org/10.2118/100434-MS.

Perkins, T.K., and L.R. Kern. 1961. "Widths of Hydraulic Fractures." *Journal of Petroleum Technology* (Original copyright American Institute of Mining, Metallurgical, and Petroleum Engineers, Inc. Copyright has expired.) 13 (09): 937-949. doi:http://dx.doi.org/10.2118/89-PA.

Pitakbunkate, Termpan, Perla B. Balbuena, George J. Moridis, and Thomas A. Blasingame. 2016. "Effect of Confinement on Pressure/Volume/Temperature Properties of Hydrocarbons in Shale Reservoirs." *SPE Journal* (Society of Petroleum Engineers) 21 (02): 621-634. doi:http://dx.doi.org/10.2118/170685-PA.

Roya, Subrata, Reni Raju, Helen F. Chuang, Brett A. Cruden, and M. Meyyappan. 2003. "Modeling Gas Flow Through Microchannels and Nanopores." (Journal of Applied Physics) 93 (8). doi:http://dx.doi.org/10.1063/1.1559936.

Rylance, Martin. 2013. "Optimising Remote Unconventional Gas Exploration." *Middle East Unconventional Gas Conference and Exhibition.* Muscat, Oman: Society of Petroleum Engineers. doi:http://dx.doi.org/10.2118/163987-MS.

Saadatpoor, E., S.L. Bryant, and K. Sepehrnoori. 2010. "New Trapping Mechanism in Carbon Sequestration." *Transp Porous Med* 82 (1): 3-17. doi:10.1007/s11242-009-9446-6.

Saadatpoor, Ehsan, Steven L. Bryant, and Kamy Sephernoori. 2010. "New Trapping Mechanism in Carbon Sequestration." (Transp Porous Med) 82 (1): 3-17. doi:10.1007/s11242-009-9446-6.

Sakhaee-Pour, A., and Steven L. Bryant. 2012. "Gas Permeability of Shale." *SPE Reservoir Evaluation & Engineering* (SPE Reservoir Evaluation & Engineering) 15 (04): 401-409. doi:http://dx.doi.org/10.2118/146944-PA.

Sakhaee-Pour, A., and Steven L. Bryant. 2014. "Pore Structure of Shale." *Fuel* 467-475. doi:10.1016/j.fuel.2014.11.053.

Sakhaee-Pour, Ahmad, and Marry F. Wheeler. 2016. "Effective Flow Properties for Cells Containing Fractures of Arbitrary Geometry." *SPE Journal* 21 (03): 965-980. doi:http://dx.doi.org/10.2118/167183-PA.

Saneifar, Mehrnoosh, Roy Conte, Clotilde Chen, Zoya Heidari, and Michael C. Pope. 2014. "Integrated Rock Classification in Carbonate Formations Based on Elastic and Petrophysical Properties Estimated From Conventional Well Logs." *SPWLA 55th Annual Logging Symposium.* Abu Dhabi, United Arab Emirates: Society of Petrophysicists and Well-Log Analysts.

Shabro, Vahid, Shaina Kelly, Carlos Torres-Verdín, Kamy Sepehrnoori, and André Revil. 2014. "Pore-scale Modeling of Electrical Resistivity and Permeability in FIB-SEM Images of Organic Mudrock." *Geophysics* (Society of Exploration Geophysicists) 79 (05): 289-299. doi:10.1190/GEO2014-0141.1.

Shad, Saeed, Brij B. Maini, and Ian D. Gates. 2010. "Effect of Fracture and Flow Orientation on Two-Phase Flow in an Oil-Wet Fracture: Relative Permeability Curves and Flow Structures." *SPE Western Regional Meeting.* Anaheim: Society of Petroleum Engineers. doi:http://dx.doi.org/10.2118/132229-MS.

Shakiba, J. T., E. Akhgarianb, and A. Ghaderic. 2013. "The effect of hydraulic fracture characteristics on production rate in thermal EOR methods." *Fuel* 141: 226-235. doi:http://dx.doi.org/10.1016/j.fuel.2014.10.063.

Sinha, S., E.M. Braun, Q.R. Passey, S.A. Leonardi, A.A. Wood, T. Zirkle, and R.A. Kudva. 2013. "Steady-State Permeability Measurements on Intact Shale Samples at Reservoir Conditions- Effect of Stress, Temperature, Pressure, and Type of Gas." *Middle East Oil and Gas show and Conference.* Manama,

Bahrain: Society of Petroleum Engineers. doi:http://dx.doi.org/10.2118/164263-MS.

Sondergeld, Carl H., Raymond Joseph Ambrose, Chandra Shekhar Rai, and Jason Moncrieff. 2010. "Micro-Structural Studies of Gas Shales." *SPE Unconventional Gas Conference.* Pittsburgh: Society of Petroleum Engineers. doi:http://dx.doi.org/10.2118/131771-MS.

Swaan, A. de. 1976. "Analytic Solutions for Determining Naturally Fractured Reservoir Properties by Well Testing." *Society of Petroleum Engineers Journal* (Society of Petroleum Engineers) 16 (03): 117-122. doi:http://dx.doi.org/10.2118/5346-PA.

Swami, Vivek, A. (Tony) Settary, and Farzam Javadpour. 2013. "A numerical Model for Multi-Mechanism Flow in Shale Gas Reservoirs with Application to Laboratory Scale Testing." *EAGE Annual Conference & Exhibition.* London: Society of Petroleum Engineers. doi:http://dx.doi.org/10.2118/164840-MS.

Tian, Wei, Xingru Wu, Zhenfeng Zhang, and Kegang Ling. 2015. "Estimate the Effective Fracture Properties from Tight Formation Production Data." *Asia Percific Unconventional Resources Conference and Exhibition.* Brisbane, Australia: Society of Petroleum Engineers. doi:http://dx.doi.org/10.2118/176983-MS.

Tinni, Ali, Ebrahim Fathi, Rajiv Agarwal, Carl H. Sondergeld, I. Yucel Akkutlu, and Chandra Shekhar Rai. 2012. "Shale Permeability Measurements on Plugs and Crushed Samples." *SPE Canadian Unconventional Resources Conference.* Calgary, Alberta, Canada: Society of Petroleum Engineers. doi:http://dx.doi.org/10.2118/162235-MS.

2012. *University of Minnesota College of Science & Engineering.* October 15. http://cefor-umn.com/mechanics-of-hydraulic-fractures/.

Warpinski, N. R., M. K. Mayerhofer, M. C. Vincent, C. L. Cipolla, and E. P. Lolon. 2009. "Stimulating Unconventional Reservoirs: Maximizing Network Growth While Optimizing Fracture Conductivity." *Journal of Canadian Petroleum Technology* (JCPT) 48 (10): 39-51. doi:http://dx.doi.org/10.2118/114173-PA.

Warren, J. E., and P. J. Root. 1963. "The Behavior of Narually Fractured Reservoirs." *Society of Petroleum Engineers Journal* (Society of Petroleum Engineers) 3 (03): 245-255. doi:http://dx.doi.org/10.2118/426-PA.

Wu, Xingru, Guangqing Zhou, Bahareh Najobaei, Hui Pu, and Yinghui Li. 2016. "Integrated Reservoir Modeling Workflow That Couples PVT and Adsorption in Confined Nano-Pores, An Eagle Ford Application." *Low Perm Symposium.* Denver: Society of Petroleum Engineers. doi:http://dx.doi.org/10.2118/180216-MS.

Xie, Jiang, Changdong Yang, Neha Gupta, Michael J. King, and Akhil Datta-Gupta. 2015. "Integration of Shale-Gas-Production Data and Microseismic for Fracture and Reservoir Properties With the Fast Marching Method." *SPE Journal* (Society of Petroleum Engineers) 20 (02): 347-359. doi:http://dx.doi.org/10.2118/161357-PA.

Xiong, X., D. Devegowda, G.G. Michel, R.F. Sigal, and F. Civan. 2012. "A Fully-Coupled Free and Adsorptive Phase Transport Model for Shale Gas Reservoirs Including Non-Darcy Flow Effects." *Annual Technical conference and Exhibition.* San Antonio: Society of Petroleum Engineers. doi:http://dx.doi.org/10.2118/159758-MS.

Yan, Bicheng, Yuhe Wang, and John E. Killough. 2013. "Beyond Dual-Porosity Modeling for the Simulation of Complex Flow Mechanisms in Shale Reservoirs." *SPE Reservoir Simulation Symposium.* Woodlands: Society of Petroleum Engineers. doi:http://dx.doi.org/10.2118/163651-MS.

Yin, Jichao, Jiang Xie, Akhil Datta-Gupta, and Alfred Daniel Hill. 2011. "Improved Characterization and Performance Assessment of Shale Gas Wells by Integrating Stimulated Reservoir Volume and Production Data." *SPE Eastern Regional Meeting.* Columbus: Society of Petroleum Engineers. doi:http://dx.doi.org/10.2118/148969-MS.

Zamirian, M., K. Aminian, and E. Fathi. 2014. "New Steady-State Technique for Measuring Shale Core Plug Permeability." *SPE/CSUR Unconventional Resources Conference.* Calgary, Canada: Society of Petroleum Engineers. doi:http://dx.doi.org/10.2118/171613-MS.

Zhang, Yuan, Hamid R. Lashgari, Yuan Di, and Kamy Sepehrnoori. 2016. "Capillary Pressure Effect on Hydrocarbon Phase Behavior in Unconventional Reservoirs." *SPE Low Perm Symposium.* Denver: Society of Petroleum Engineers. doi:http://dx.doi.org/10.2118/180235-MS.

Zheng, Jiangtao, Yang Ju, Hui-Hai Liu, Liange Zheng, and Moran Wang. 2016. "Numerical prediction of the decline of the shale gas production rate with considering the geomechanical effects based on the two-part Hooke's model." *Fuel* 185: 362-369. doi:http://dx.doi.org/10.1016/j.fuel.2016.07.112.

Zoback, Mark D., Arjun Kohli, Indrajit Das, and Mark McClure. 2012. "The Importance of Slow Slip on Faults During Hydraulic Fracturing Stimulation of Shale Gas Reservoirs." *Americas Unconventional Resources Conference.* Pittsburgh: Society of Petroleum Engineers. doi:http://dx.doi.org/10.2118/155476-MS.